Interface Modification and Interfacial Charge Dynamics in Quantum Dot Solar Cells and Perovskite Solar Cells

YAOHONG ZHANG

THE UNIVERSITY OF ELECTRO-COMMUNICATIONS

SEPTEMBER 2017

Interface Modification and Interfacial Charge Dynamics in Quantum Dot Solar Cells and Perovskite Solar Cells

Yaohong Zhang

Doctor of Philosophy

THE UNIVERSITY OF ELECTRO-COMMUNICATIONS

SEPTEMBER 2017

Interface Modification and Interfacial Charge Dynamics in Quantum Dot Solar Cells and Perovskite Solar Cells

APPROVED BY THE SUPERVISPRY COMMITTEE:

CHAIRPERSON: Prof. Qing Shen

MEMBER: Prof. Abe

MEMBER: Prof. Okuno

MEMBER: Prof. Takashi

MEMBER: Prof. Toyoda

量子ドット太陽電池とペロブスカイト太陽電池における界面修飾と界面電荷ダイナミクス

和文要旨

現在エネルギーと環境問題はますます深刻になってきたため、無尽蔵で安全なエネルギー源である太陽光の活用が強く望まれている。しかし、太陽エネルギーは大きな可能性があるにも関わらず、現在ごくわずかしか利用されていない。その原因は、太陽電池の作製コストが高く、かつ変換効率が十分には高くないことにある。最近、コロイド量子ドット太陽電池とペロブスカイト太陽電池は安価な溶液法で作製可能であることと理論変換効率は高いため、次世代太陽電池として注目されている。しかし、これらの次世代太陽電池を実用化させるためには、さらなる高効率化と安定化の実現とそのメカニズムの解明に関する基礎研究は不可欠である。特にこれらの太陽電池の各界面における電荷分離と再結合過程の解明、これらの界面電荷ダイナミクスと太陽電池の光電変換特性および安定化との関連を明らかにすることは鍵となる。

そこで本研究では、PbSe、PbS コロイド量子ドット太陽電池とペロブスカイト太陽電池を作製し、各界面に対して様々な有機分子と無機分子による界面修飾を行うことにより、太陽電池の変換効率の向上と安定化の向上に成功した。さらに、過渡吸収分光法と開放電圧の過渡応答測定法などを用いて、界面電荷分離と再結合ダイナミクスを解明し、界面修飾によるこれらの界面電荷移動ダイナミクスの変化と効率向上および安定化向上との関連性を明らかにした。具体的に以下の 3 つの内容である。

（1）PbSe 量子ドット太陽電池の界面修飾と界面電荷分離・再結合ダイナミクスについて研究を行った。まず、新しい方法を提案し安定な PbSe 量子ドット溶液の作製に成功した。次に、異なる 4 種類のリガンド分子（2 種類の

有機分子と 2 種類の無機分子）を PbSe 量子ドットの表面パッシベーションに適用し、PbSe 量子ドット薄膜を形成した。これらのリガンドの違いによる PbSe 量子ドット膜の空気中での安定性の変化、 PbSe 量子ドット膜のエネルギー準位の変化、PbSe 量子ドット太陽電池の光電変換特性の変化について詳しく調べた。さらに、過渡吸収分光法により量子ドット界面での電荷移動速度定数のリガンド長さ依存性とそのメカニズムを検討した。また開放電圧の過渡応答測定により PbSe 量子ドットにおける光励起キャリアの寿命と再結合過程のリガンド分子依存性を明らかにした。これらの結果により、適切な量子ドット界面修飾方法を確立できれば、空気中で安定でありさらなる高効率化である PbSe 量子ドット太陽電池の構築ができることが判明した。

（2）PbS 量子ドット太陽電池の界面修飾と界面電荷再結合の抑制について研究を行った。従来の PbS 量子ドットヘテロ接合型太陽電池のデバイス構造の中に、PbS 量子ドット層と Au 電極との界面に BTPA-4 という新しい有機小分子層をホール選択層として導入することをはじめて提案した。これにより、PbS 量子ドット太陽電池の開放電圧の向上に成功した。そのメカニズムを解明するために、開放電圧の時間応答と交流インピーダンスの測定を行った。その結果より、BTPA-4 ホール選択層の導入により、PbS 量子ドット層と Au 電極の界面での再結合を著しく抑制できたため、、PbS 量子ドット太陽電池における光励起キャリアの寿命が長くなり、開放電圧が向上できたことが明らかになった。さらに、この有機小分子 BTPA-4 を導入した PbS 量子ドット太陽電池は空気中で 100 日以上保存しても安定であることを実証した。この結果より、ご提案した BTPA-4 ホール選択層は従来の有機ホール選択層より安定であり、量子ドット太陽電池に応用できることが判明した。

（3）ペロブスカイト太陽電池の新しいホール輸送層の導入と界面電荷再結合の抑制について研究を行った。ペロブスカイト太陽電池は最近の 5 年間で大変盛んに研究されている。従来ペロブスカイト太陽電池では、Spiro-OMeTAD をホール輸送層としてほとんど使われているが、Spiro-OMeTAD の

コストが高いことは大きな課題であり、新しいホール安価な輸送層の開発が強く望まれている。そこで本研究では、Spiro-OMeTAD より安く合成できる３種類の異なる分子構造の新しいホール輸送層（BTPA-4, BTPA-5 と BTPA-6）をペロブスカイト太陽電池に導入し、界面電荷再結合と光電変換特性への影響について検討した。その結果、ペロブスカイト層とホール輸送層の界面における電荷再結合と光電変換特性はホール輸送層の分子構造に強く依存することを見出した。その中で、BTPA-6 を用いた場合では、ペロブスカイト太陽電池の変換効率は 14.4%に達成し、従来の Spiro-OMeTAD を用いた場合の変換効率（15.0%）とほぼ同レベルであった。さらに、BTPA-6 を用いた場合のペロブスカイト太陽電池の安定性は Spiro-OMeTAD を用いた場合のペロブスカイト太陽電池の安定性よりいい結果が得られた。BTPA-6 は有望なホール輸送材としてペロブスカイト太陽電池に応用できることが判明した。

以上の３つの研究内容の結果より、今後量子ドット太陽電池とペロブスカイト太陽電池のさらなる高効率化と安定化の実現に重要な知見を与えることが明らかになった。

Interface Modification and Interfacial Charge Dynamics in Quantum Dot Solar Cells and Perovskite Solar Cells

Abstract

The present globalization of energy shortage and environmental pollution issues have posed a grave menace to human survival and development. Finding a viable supply of clean, renewable energy is one of the most daunting challenges facing the world. Solar cells as devices that convert solar energy into electricity is the focus of the whole society. However, conventional solar cells have had limited impact in meeting this challenge because of their high pollution, high cost and low power conversion efficiencies. Recently, colloid quantum dot solar cells (CQDSCs) and perovskite solar cells (PSCs) as new generation solar cells have been attracting immense attention owing to their inexpensive solution-based techniques and high theoretical power conversion efficiency. However, stability is still a big problem for CQDSCs and PSCs, and charge dynamics in those solar cells are not clear. To obtain stable CQDSCs and PSCs through interface modification, and reveal the charge dynamics in those solar cells are the central aim of this thesis.

This thesis investigated the surface ligand dependent charge carrier dissociation, charge carrier transmission and recombination of CQDSCs, and used novel hole transport materials to modify the interface of CQDSCs and PSCs to reduce the interfacial recombination in CQDSCs and PSCs.

In this thesis, I explore a method to obtain air stable PbSe CQDs and surface ligand dependent exciton dissociation, recombination, photovoltaic property, and stability of PbSe solid films and CQDSCs. I select four short ligands, that is, two organic ligands 1,2-ethanedithiol (EDT) and 3-mercaptopropionic acid (MPA); two inorganic ligand cetyltrimethylammonium bromide (CTAB) and tetrabutylammonium iodide (TBAI) to investigate the ligand-dependent air stability, energy level shift, the exciton dissociation, and photovoltaic properties of PbSe CQDSCs. In addition, the charge transfer rate, recombination processes and carrier lifetimes in these CQDSCs were also

revealed through ultrafast transient absorption (TA) spectra, and open-circuit transient voltage (V_{oc}) decay measurements.

We also explore a method to suppress the interfacial recombination at QDs/Au electrode in CQDSCs by using organic small molecule. We develop a novel donor-π-donor (D-π-D) organic small molecule bis-triphenylamine with spiro(fluorene-9,9'-xanthene) as the conjugated system, named BTPA-4, as a hole selective layer (HSL) in the PbS CQDSCs. We found that the introduction of BTPA-4 as HSL can enhance the open-circuit voltage (V_{oc}), prolong the effective carrier lifetime, reduce the interfacial recombination at PbS QDs/Au interface, and hence improve the device performance. Furthermore, the PbS CQDSCs with BTPA-4 possessed a noticeably stable property for over 100 days of storage under ambient atmosphere that has been the Achilles' heel of other organic HSL for CQDSCs.

We also focus on hole transport materials and the interfacial recombination in PSCs. Three triphenylamine-based hole-transport materials (HTMs), named BTPA-4, BTPA-5 and BTPA-6, were used into PSCs. BTPA-6 with four substituted triphenylamine units exhibited a better solar cell performance than BTPA-4 and BTPA-5 which contain two substituted triphenylamine units. BTPA-6 achieved a PCE of 14.4% which nearly matches Spiro-OMeTAD (15.0%). The order of the recombination resistance was found to be in the order of BTPA-4 < BTPA-5 < BTPA-6 < Spiro-OMeTAD, indicating that the electron blocking capability of the HTM is in this order. This trend agrees with the V_{oc} trend of their corresponding solar cells. In addition, BTPA-6 based devices showed better long-term stability than that with Spiro-OMeTAD, which can partially be attributed to the hydrophobicity of BTPA-6 is better than that of Spiro-OMeTAD.

The goal of above experiments is to gain a more complete understanding of charge carrier dynamics in CQDSCs and PSCs, so that more efficient materials and architecture for solar cells can be designed in the future.

Table of Contents

Chapter 1: Introduction and Background

1.1 The Energy and Environmental Crisis

With the development of economy, human consumes more and more energy and resources. Simultaneously, the heavy using of traditional fuels makes great damage to the environment. Exploiting and utilizing low cost, low-carbon emission, renewable energy sources becomes particularly urgent. Recently, we rely on fossil fuels, nuclear energy and renewable energies of our energy supply. In Japan, their contributions were 82%, 11% and 7% in 2010, and 93%, 0%, 7% in 2014, respectively. Around the global, their contributions were 82%, 5% and 14% in 2012. Those data show that fossil fuels take over 80 % part both in Japan and the world. What' more, after the Fukushima Dai-ichi nuclear accident, the nuclear energy supply for Japan has been absolutely replaced by fossil fuels.[1] Thus, we have now come to expect on the low cost, high efficiency, and easy promotion renewable energy sources.

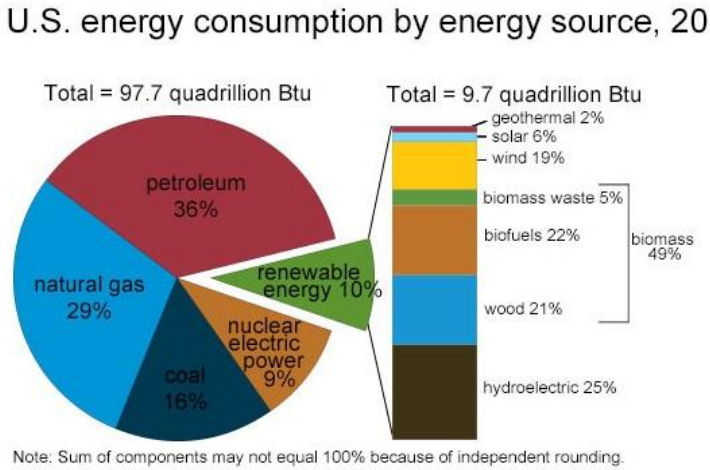

Figure 1-1. U. S. energy consumption by energy source in 2015. [2]

Different from fossil fuels, renewable energy is energy supplied by inexhaustible source. There are some commonly used renewable energy sources: wind, biomass, hydropower and solar. Among them, solar is the most important renewable energy sources. Solar is a powerful source of energy from the sun. Recently, the most

commonly ways to use solar energy for our daily life are solar water heating and convert sunlight directly into electricity by solar cells.

1.2 Solar Cells

Solar cells can convert sunlight energy to electrical energy based on the principles of the photovoltaic effect of semiconductor materials. Sunlight is made up of photons if the absorbed photons has larger energy than the bandgap energy of semiconductor, electrons will be excited from semiconductor's valence band up to its conduction band, and leaving holes in the valence band. Once the electron and hole are separated successfully, the photogenerated electron and hole are driven by the built-in electric field to the edges of the depletion region. The electrons and holes which in quasi-neutral region, should be diffused through the quasi-neutral region to flow through an external circuit and supply power to appliances.[3]

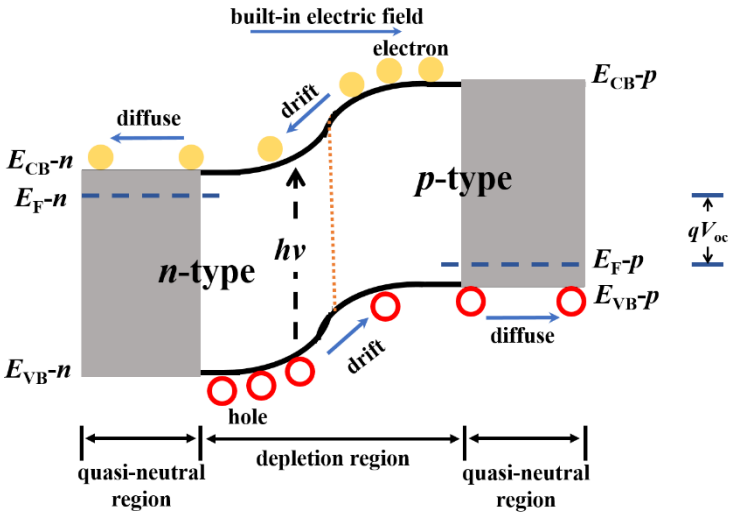

Figure 1-2. Working schematic diagram of classic *p*-*n* junction. qV_{oc} is the difference between quasi-Fermi level of electrons (E_F-*n*) in the *n*-type semiconductor and quasi-Fermi level of (E_F-*p*)in the *p*-type semiconductor on sunlight.[3]

Performance of solar cells can usually be evaluated through two main indexes: power conversion efficiency (PCE) and stability. The PCE of solar cell can be calculated by following equation:

$$PCE = \frac{J_{sc} \times V_{oc} \times FF}{P_{in}} \times 100\% \qquad (1-1)$$

where V_{oc} is open circuit photovoltage, J_{sc} is the short circuit current density, FF is the fill factor (the maximum power divided by the product of J_{sc} and V_{oc}), and P_{in} is the incident light intensity. For one sun illumination, P_{in} is 100 mW/cm^{-2}. Figure 1-3 shows the current density-voltage (J-V) curves of a perovskite solar cell.

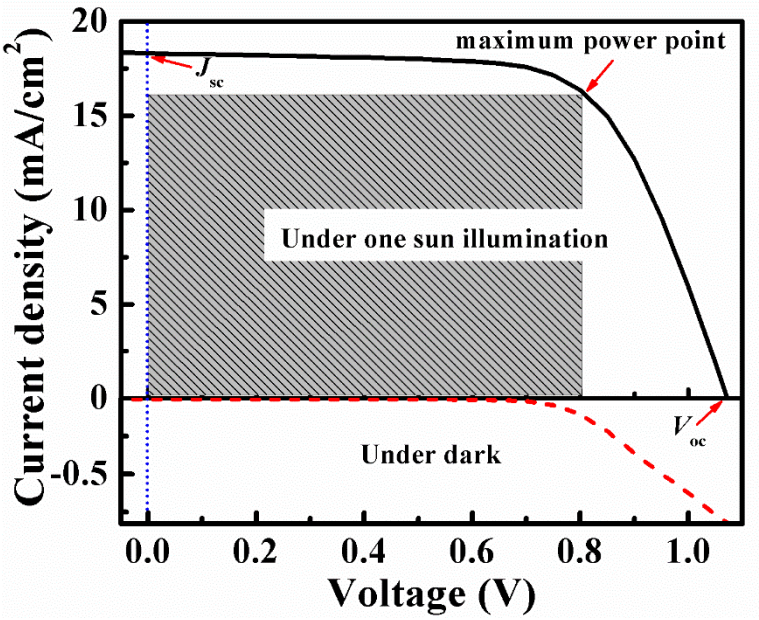

Figure 1-3. J-V curves of a perovskite solar cell under dark and under one sun illumination.

For solar cells, V_{oc} is determined by the difference of the quasi Fermi level of n-type material (E_F-n) and that of p-type material (E_F-p), divided by q, the equation is:

$$V_{oc} = \frac{E_{Fn} - E_{Fp}}{q} \qquad (1-2)$$

And J_{sc} is the largest value of photocurrent that can be supplied by a solar cell per unit area. It mainly depends on light power, the absorption spectrometry, absorbance of

light absorbing layer, and the charge recombination in the solar cells. There exists a relationship between J_{sc} and V_{oc}:

$$V_{oc} = \frac{kT}{q} ln \frac{J_0 + J_{sc}}{J_0} \approx \frac{kT}{q} \ln \frac{J_{sc}}{J_0} \qquad (1-3)$$

Besides J_{sc}, V_{oc} and FF, the series resistance (R_s) and shunt resistance (R_{sh}) are also very important parameters for solar cells. The following equations describe the J-V characteristics of a solar cell:

$$I_{sc} = I'_{sc} - I_0 \left[\exp\left(\frac{qI_{sc}R_s}{n_0 kT}\right) - 1\right] - \frac{I_{sc}R_s}{R_{sh}} \qquad (1-4) \ [4]$$

$$\frac{V_{oc}}{R_{sh}} = I'_{sc} - I_0 \left[\exp\left(\frac{qV_{oc}}{n_0 kT}\right) - 1\right] \qquad (1-5) \ [4]$$

where I'_{sc} is the short circuit current when R_s is zero and R_{sh} is infinite; n_0 is the diode ideality factor. From equation 1-4 and 1-5, it can be seen that series resistance R_s reduces J_{sc} but has no effect on V_{oc}. In contrast, the shunt resistance R_{sh} has no effect on J_{sc} but can reduce the V_{oc}. R_s is mainly associated with charge transport resistance, while R_{sh} is associated with charge recombination resistance. In addition, FF is mainly dependent on both of R_s and R_{sh}: the lower the R_s, the larger the R_{sh}, leads to the larger the FF. All in all, minimized R_s and maximized R_{sh} are beneficial for J_{sc}, V_{oc} and FF and hence the PCE.[3]

Like other devices, environment temperature also affects the performance of solar cells. The band gap (E_g) of semiconductor has relationship with temperature:

$$E_g(T) = E_g(0) - \frac{\alpha T^2}{T + \beta} \qquad (1-6)$$

where α and β are intrinsic constants of semiconductor, T is environmental temperature and $E_g(0)$ is the band gap at 0 K. With environmental temperature increasing, the band gap of semiconductor becomes narrowing, and the decrease of band gap can be regarded as increasing the energy of the electrons. The band gap of semiconductor also depends on the bond energy of atoms. Thus, with environmental temperature increasing, band gap of semiconductor reduced, in turning to affecting most material parameters of semiconductor. The temperature dependency V_{oc} for solar cell is approximated by the following equation[5]:

$$\frac{dV_{oc}}{dT} = -\frac{\frac{E_g(0)}{q} - V_{oc} + \zeta\frac{kT}{q}}{T} \qquad (1-7)$$

The J_{sc} of solar cell, increases slightly with temperature, due to the band gap of semiconductor was narrowed and absorbs more light to create e-h pairs. As I have introduced in above, J_{sc} of solar cell depends on incident light energy. Another important parameter, quantum efficiency (QE), can characterize the relationship between J_{sc} and incident light. The QE is the percentage of the absorbed photons that are converted to electric current in solar cell. The QE spectrum ideally has the square shape, and for most solar cells is reduced due to surface and interfacial recombination in solar cells. There are two common expressions of QE: external quantum efficiency (EQE) and internal quantum efficiency (IQE). EQE is defined to be the probability of suppling one electron to the external circuit by single incident wavelength (λ) light. The equation is:

$$\mathrm{EQE}(\lambda) = \frac{I_{sc}(\lambda)}{qAQ(\lambda)} \qquad (1-8)$$

A is the active area of solar cell, Q (λ) is the incident photon flux density on solar cell.

The EQE of a solar cell depends on the incident light (included transmission and reflection light). IQE is defined to be the probability of suppling one electron to the external circuit by absorbing single wavelength (λ) light. The IQE of a solar cell depends on its absorbed light. By measuring the percentage of light transmission and reflection of a solar cell, IQE can be calculated from EQE curve. The equation is:

$$\text{IQE}\ (\lambda) = \frac{EQE(\lambda)}{1 - R(\lambda) - T(\lambda)} \qquad (1-9)$$

R(λ) and T(λ) are hemispherical directional reflectance and hemispherical transmission of the solar cell, respectively. If the solar cell is thick enough, $T(\lambda)=0$.

1.3 Types of Solar Cells

Solar cell can be categorized into various classes basis on the types of materials applied for solar cells and the structure of solar cell as shown in Figure 1-4.

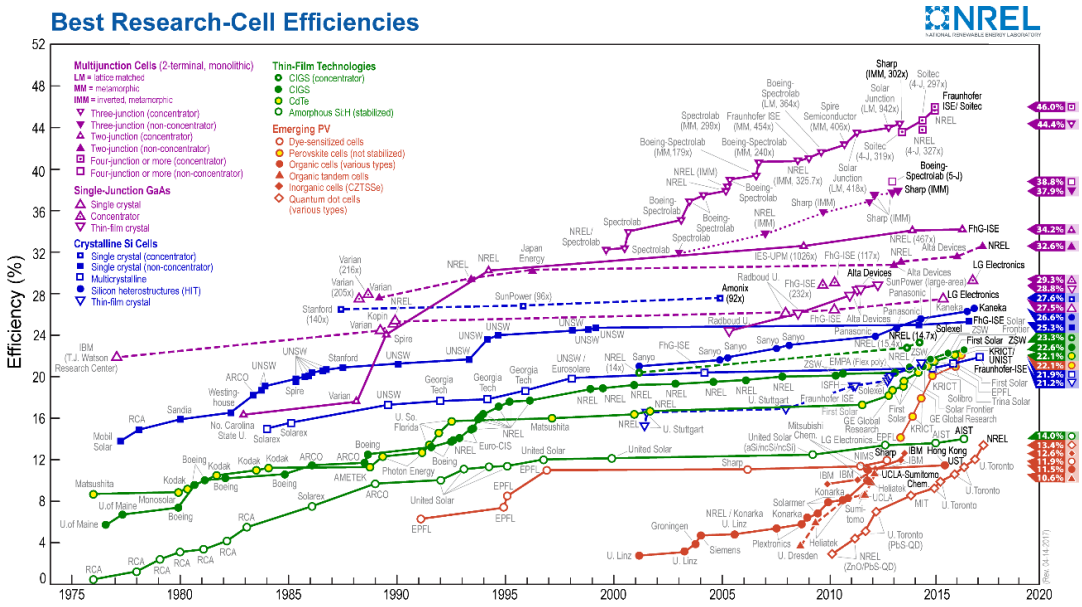

Figure 1-4. The research solar cells record efficiencies chart.[6]

1.3.1 First Generation Solar Cells-Silicon Wafer Based

The first-generation solar cells are based on silicon wafers. It is the oldest and the

most widely used type of solar cell due to its stable and high performance. The silicon wafer based solar cell can further be subdivided into two distinct classifications: single-crystalline silicon solar cell and multi-crystalline silicon solar cell. Single-crystalline solar cell, as the name indicates, is manufactured from single crystals of silicon. In order to obtain requirement quality single crystals of silicon, multi process and a lot of energy are needed, so the price of single-crystalline silicon solar cell is expensive. The new efficiency record of single-crystalline silicon solar is 26.3%.[7] Multi-crystalline silicon solar cells are generally composed of several different crystals, coupled to one another in a single cell. The processing of multi-crystalline silicon solar cells are more economical and most popular solar cells. They are slightly cheaper to fabricate compared to single-crystalline silicon solar cells. Now the most widely used solar cells is multi-crystalline silicon solar cells with efficiencies ranging between 18%-19.9%.[7] Due to the low absorption coefficient of silicon, the silicon solar cell devices are required to over hundreds of microns thickness in order to absorb more incident light. The devices made with so thick layers require high pure crystalline silicon to ensure efficient extraction of carriers. Through the first-generation solar cells need expensive processing requirements, these devices, with high efficiency and stable performance and decreasing costs, occupy the highest percentage of market today.[8]

1.3.2 Second-Generation Solar Cells-Thin Film Solar Cells

CdTe, $CuIn_xGa_{(1-x)}Se_2$ (CIGS) and a-Si, etc. thin film solar cells are considered to second generation solar cells, and are more economical than the first-generation solar cells. The light absorbing layers of the first-generation solar cells are up to 350 μm thick, while thin film solar cells have about several microns thickness thin light absorbing layers.[9] The thin films technologies use methods such as spray pyrolysis, sputter coating or vapor deposition (PVD or CVD) and allow simultaneously assemble constructions of entire modules. Some thin film solar cells with enough thin film can be deposited on flexible substrates or through solution processing, these technologies can further expand the application fields and reduce the costs of solar cells. Recently, the PCE of the lab scale thin film solar cells has reached about 22% (in Figure 1-4), but their module's PCEs are still ~17%.[7] Moreover, most of the thin films technologies should use rare earth metals, which could restrict their large-scale

application in the future. However, because of their low cost, the market share of thin film solar cells is continually increasing.

1.3.3 Third-Generation Solar Cells

Third-generation solar cells take advantage of promising technologies to promote solar cell efficiency to overcome the Shockley-Queisser limit of 33%.[10] The Shockley-Queisser limit proves that semiconductor with a bandgap of 1.4 eV have a largest theoretical efficiency of 33%. It mainly due to semiconductor's incomplete absorption of the solar spectrum, heat relaxation of excess energy and thermodynamic losses.[8] Emerging solar cells include: copper zinc tin sulfide solar cell (CZTS), organic solar cells (OPV), dye-sensitized solar cells (DSSCs), quantum dot solar cells (QDSCs) and perovskite solar cell (PSCs). The following will emphases upon the introduction of quantum dot solar cells and perovskite solar cells.

1.4 Quantum Dot Solar Cells (QDSCs)

1.4.1 Quantum Dots (QDs)

Quantum structures are nanocrystals composed of a few thousand atoms or less that experience quantum confinement in at least one dimension. it means that a quantum confined nanostructure approaches and then becomes smaller than its exciton Bohr radius, a natural length scale that characterizes the average separation between electrons and holes in the bulk. Quantum dots (QDs) are several nanometers small nanoparticles. The optical and electronic properties of QDs are different with their bulk materials. QDs will emit specific frequencies lights when electricity or light is applied to them, and those lights can be precisely tuned by changing the sizes or shapes of QDs. In QDs, the electron-hole pairs can be generated by excited light cannot move as in bulk material since the discrete nature of their energy levels. When the electron and hole are confined within a zero dimension which approach to or smaller than QDs Bohr radius, the exciton receives enhancing confinement effects which drastically change the stayed energy levels and lead to increasingly discrete electronic structures.

1.4.2 Multiple Exciton Generation

Multiple exciton generation (MEG) is the process by which one photon ($h\nu > 2\ E_g$) can generate multi electron-hole pairs in a quantum confined material.[11] MEG effect can break the Shockley-Queisser limit in bulk material through a process similar to impact ionization. Impact ionization (one photon producing multi electron-hole pairs) was difficult to find in bulk materials because of the momentum and energy conservation, which means the energy threshold for impact ionization is often over three times the bandgap of the bulk material, requiring light well in the UV range (λ<400 nm) which take up only a narrow portion of solar spectrum.[12] The MEG process results in that the extra energy in a hot carrier can be used in a reverse Auger recombination process to create multi electron-hole pairs. During the Auger recombination process, an electron-hole pair at the band edge can transfer its energy to another electron-hole pair at the band edge through non-radiative transition. This process leads to fast hot carrier cooling due to the generated single high energy exciton is quickly cooling to the band edge.[13] Meanwhile, hot carrier Auger cooling process is where a high level excited electron transfers its extra energy to its associated hole therefore bypassing the hot phonon bottleneck because of the high density of hole states. These processes are considered to be increased in quantum confined systems due to the enhanced coulomb coupling and decreased in translational momentum conservation.[11, 14] Nozik, A. J. proposed that quantum confined materials can be more efficient for generating multi electron-hole pairs from a high energy single photon using fundamentally different physics than bulk materials.[15]

In quantum dot solar cells, MEG phenomenon has great application value if multiple photogenerated excitons can be efficiently extract before they recombined. The high charge collection efficiency of multiple carriers has the potential to remarkably enhance the efficiency of solar cells, leading to an over 100% EQE at high energy wavelengths and finally obtains higher PCE. The further combination of MEG with solar concentration is expected to largely improve the efficiency to 75% at 500 nm based on theoretical calculations, much more efficient than the expected theoretical increase for conventional silicon-based solar cells.[16-17] QDs have the potential to largely improved V_{oc} and J_{sc} of solar cells by extracting hot carriers and multiple

excitons, respectively. The efficient realization of these goals should faces a great challenge because of the fast charge carriers relaxation process in the solar cell cannot be underestimated.[17]

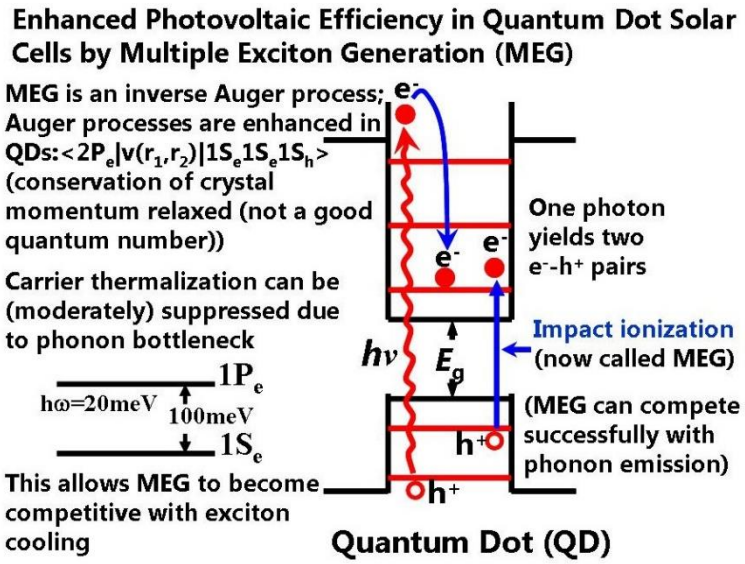

Figure 1-5. Schematic of multiple exciton generation process in QDs.

1.4.3 Quantum Confinement Effect

Semiconductors can be characterized by two distinct distributions of allowed states called the conduction band (or lowest unoccupied molecular orbital, LUMO) and valence band (or highest occupied molecular orbital, HOMO) which separated by the bandgap (E_g) of the material (Figure 1-6). If individual atoms bind with each another, their atomic orbitals will split to form pairs of molecular orbitals. For numerous regular arrangement of atoms combing in a crystal lattice, the states form continuous energy bands are separated by energy gaps instead of isolated energy levels. The bandgap of material is defined as the amount of energy needed to move an electron in a perfect, infinite crystal lattice from the fully occupied valence band to the unoccupied conduction band, where the electron can freely move.[11] When the size of a semiconductor is reduced to a few hundred atoms (0 D), the density of states in the bands is replaced by a set of isolated energy levels, *i.e* S, P and D levels, which may have energy level spacing, e.g. *E*p-*E*s. The reorganization of density of states in

quantum levels produce effect on the optical and electronic properties of the semiconductor.[18-19]

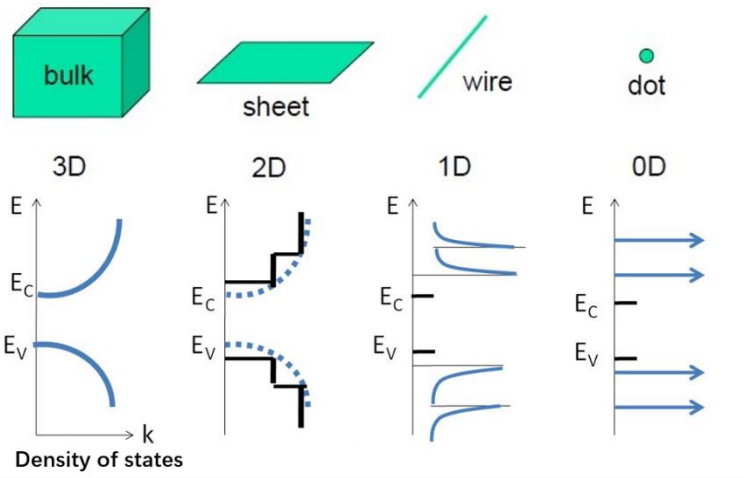

Figure 1-6. Schematic of density of states in different confinement configurations: (a) bulk (3D); (b) sheet (2D); (c) wire (1D); (d) QD (0D).

In QD, the electron-hole pairs are known as excitons are not free due to the isolate nature of the energy levels. Therefore, when the electron and hole are bound in a particle dimension that is approach to or smaller than its Bohr radius, electron and hole interact strongly with each another by Coulomb forces. With the size of the semiconductor is decreasing from bulk to QD dimension, the density of states is changing from continuous to isolate by the isolate energy levels. These isolate levels can be found by solving the Schrodinger equation for different particle dimensions.[20]

For bulk semiconductor, wavefunction of electron is delocalized and electrons can freely move throughout the conduction band. So, we can use the wavefunction of free particle which without any confinement condition to compute the Schrodinger equation for finding possible energy values.[20] The energy of the electron in bulk semiconductor can be expressed as following:

$$E(k) = \frac{\hbar^2(k_x^2 + k_y^2 + k_z^2)}{2m_e^*} \qquad (1-10)$$

where k is wave vector, $\hbar$ is Planck constant, and m_e* is electron effective mass. When the dimensions of the semiconductor reduced smaller than its exciton Bohr radius, the energy of the discrete states for QDs for spatial dimensions of L_x, L_y, and L_z can be expressed as following: [21]

$$E(k) = \frac{\hbar^2}{8m_e^*}\left(\frac{n_x^2}{L_x^2} + \frac{n_y^2}{L_y^2} + \frac{n_z^2}{L_z^2}\right) \qquad (1-11)$$

where $k_x = \pi(\frac{n_x^2}{L_x^2})^{\frac{1}{2}}$, $k_y = \pi(\frac{n_y^2}{L_y^2})^{\frac{1}{2}}$, and $k_z = \pi(\frac{n_z^2}{L_z^2})^{\frac{1}{2}}$ are for a bound QD.

In the same way, the energy eigen values for spherical QD can be defined as:

$$E^e = E_g + \frac{\hbar^2}{2m_e}(\frac{\alpha_{n_e\ell_e}}{R})^2 \qquad (1-12)$$

$$E^h = \frac{\hbar^2}{2m_h}(\frac{\alpha_{n_h\ell_h}}{R})^2 \qquad (1-13)$$

$$E = E^e + E^h = E_g + \frac{\hbar^2}{2m_e}(\frac{\alpha_{n_e\ell_e}}{R})^2 + \frac{\hbar^2}{2m_h}(\frac{\alpha_{n_h\ell_h}}{R})^2 \qquad (1-14)$$

in above equations $\alpha_{n_e\ell_e}$ is the n^{th} root of the ℓ^{th} order Bessel function for the electron while is the $\alpha_{n_h\ell_h}$ is the n^{th} root of the ℓ^{th} order Bessel function for the hole.

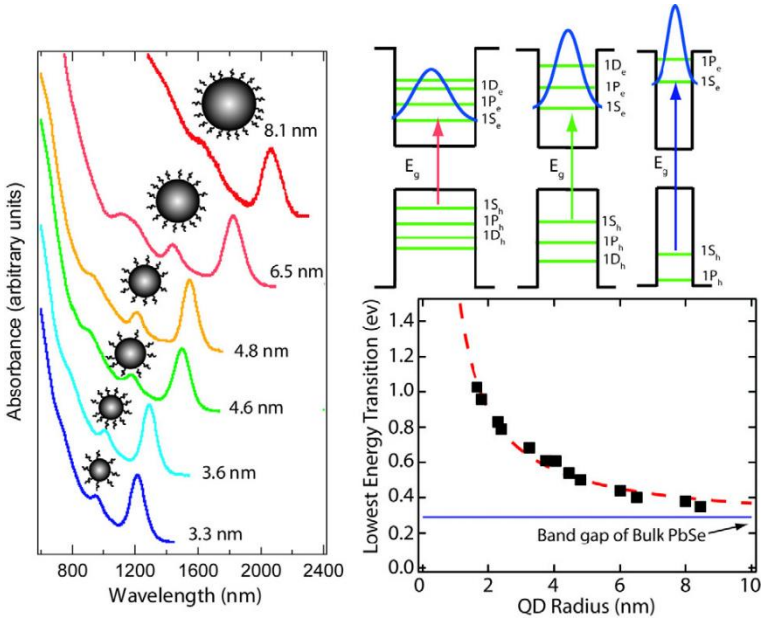

Figure 1-7. Size dependent band gap of PbSe QDs. Absorption spectra of PbSe QDs spanning the range from 8.1 nm to 1.8 nm show strong quantum confined $1S_{1/2}$ exciton shifted absorption. when the size of semiconductor material is smaller than the exciton Bohr radius of bulk semiconductor, the exciton experiences increasingly strong confinement effects which significantly alter the allowed energy levels and result in a size dependent and increasingly discrete electronic structure. The intra-band transition energies increase, and their widths narrow, resulting in optical absorption spectra that reveal structure indicative of discrete transitions with gaps between transitions reaching several hundred meV.[22-23]

In addition, according to equation 1-14, the effective band gap E_g of semiconductor increases with material decreasing size. The Figure 1-7 shows the increasing bandgap energy and intra-band spacing with the sizes of QDs. Semiconductor's property such as electrical and optical properties are mainly dependent on the quantum size effects of semiconductor. The size of the structure limits the exciton-Bohr radius of the bound electron-hole pairs, leading to altered electronic and optical properties, and causes high surface energy, which alters the physical properties.[20, 24] The actual size of semiconductor is usually smaller than its theoretical exciton Bohr radius (α_B). For the α_B of Si is at 4.9 nm, and for PbSe is at 6.1 nm, defined to be:

$$\alpha_B = \frac{e_0 \hbar^2}{m_r e^2} \qquad (1-15)$$

where e_0 is the dielectric constant of the QD (at low frequencies), $\hbar$ is Planck constant, and m_r is the reduced electron-hole mass. [24]

1.4.4 Classes of QDSCs

The most magnetic characteristic of quantum dot to solar cells or other devices is their tunable band gaps. Thanks to the quantum confinement effect, QDs' bandgaps can easily change by adjusting QD sizes. The smaller the QD size, the larger the band gap. Thus, the optical and electronic properties of QDs can be handily tuned. One of the most straight forward benefits from this phenomenon is the extended absorption range to the near-infrared (NIR) by using NIR-absorbing QDs (e. g. PbS, PbSe, etc). The NIR region sunlight contains about half of the sun irradiation, absorbing NIR region photons represents a great opportunity to dramatically improve the PCE of solar cells. Among narrow band gap (e.g., ~1.4−0.8 eV or even lower) QDs, such as PbS and PbSe have attracted great attention and have been extensively employed for thin-film solar cells applications.

Since QD-based solar cells were first reported in 1998, their PCE have been increased from below 1 to 13.4%.[6, 25] Although they have attracted extensive research interest, the improvement of the device performance was relatively steady and slow in the first 10 years or so. The past several years has be seen a rapid progress of this field, the highest ever certificated PCE of 13.4% was reported this year.[6] The impressive improvements have mainly been achieved via designing and improving device architectures and QD surface engineering. Diverse device architectures of QD-based solar cells have been developed to improve the photon-to-electron conversion efficiency. Recently, there are about four classes of QDSCs. They are a QD-sensitized solar cell, Schottky junction solar cell, depleted heterojunction solar cell, and depleted bulk heterojunction solar cell.[26] Almost all of these solar cells favor the use of monodisperse, high-quality colloidal QDs (CQDs) to avoid possible charge carrier trapping and recombination in QDs.

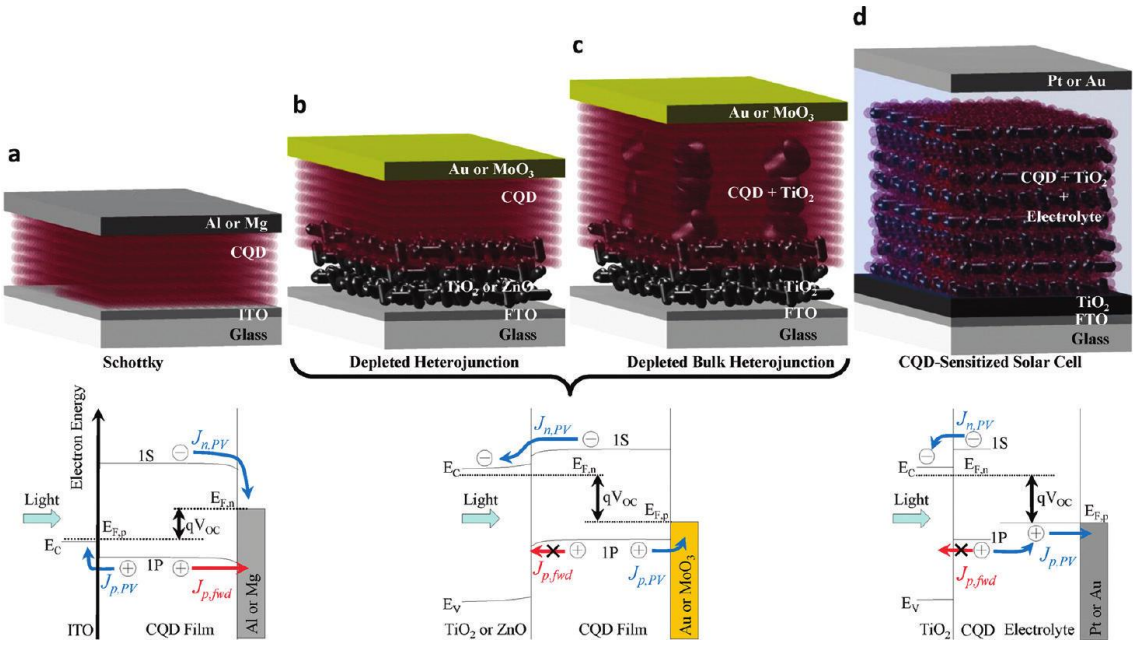

Figure 1-8. Single-junction CQD solar cell architectures. (a) Schottky CQD solar cell. (b) Depleted heterojunction CQD solar cell. (c) Depleted bulk heterojunction CQD solar cell. (d) CQD-sensitized solar cell. Also shown are the electron band diagrams of each architecture as indicated. Note that the depleted heterojunction and depleted bulk heterojunction solar cells share the same band diagram, with the only difference being the larger volume of CQDs within the depletion region due to the interfacial higher surface area between the TiO_2 and CQD film.[26]

1.4.4.1 Schottky CQD Solar Cells

The first Schottky CQD solar cell involving a thin and compact PbSe QDs film was reported by J. M. Luther in 2008.[27] This type of solar cells was once leading in the efficiency in all types of QD solar cells, with the highest reported efficiency reaching 4.5% in 2011.[28] The structure is quite simple and is constructed by sandwiching the QD layer in between an Ohmic-contact transparent electrode (such as indium-doped tin oxide (ITO)) and a low work function metal electrode. In general, electron-hole pairs are photogenerated in the absorbing QDs layer and separated at the Schottky junction imposed in between the back-contact electrode and QDs layer. Although the Schottky junction architecture demonstrates functional simplicity and ease of fabrication, it suffers from some inherent problems of limited QD layer thickness and low V_{oc}. The former constraint arises from the dilemma of poor diffusion of minority

carriers generated on the illumination side and the location of the Schottky contact at the back, while the latter limitation is set by Fermi level pinning, with the upper limit only being approximately half of the band gap of QDs.[17, 29-30]

1.4.4.2 CQD-Sensitized Solar Cells

CQD-sensitized solar cells represent one of the earliest configurations of QD solar cells, and emerged from the foundations of dye-sensitized solar cells (DSSCs).[31-32] The operative mechanism is the same as that of dye-sensitized solar cells, except for the dye sensitizer being replaced by CQDs. By substituting CQDs for the molecular dye, it is possible to extend the absorptive range beyond the cutoff wavelengths of molecular dyes. The cells are typically made up by coupling CQDs to other wider band-gap electron transport materials, such as ZnO or TiO_2 with favorable band offset, to enable the charge separation at this interface. The presynthesized CQDs are usually coated by non-conductive long chain surface ligands (e.g. oleic acid, oleylamine, or trioctylphosphine), these long chain ligands should be removed from the surface of CQDs before used into solar cells. One way to achieve it is using bifunctional linker molecules. I. Robel, et al successfully linked CdSe CQDs with TiO_2 by using mercaptopropionic acid (MPA) and observed a photon-to-charge carrier conversion efficiency of 12%.[32] High quality of CQDs with low defects can improve the PCE of solar cells. The highest efficiency for CQD sensitized solar cells which was obtained by X. H. Zhong's group was further increased to 12.45% (with certified efficiency of 12.07%) by utilizing Zn-Cu-In-Se CQDs as a sensitizer.[33] In order to reduce the electrolyte corrosion effect on QDs, Q, Shen, et al proposed a breakthrough technique: depositing a thin ZnS layer on the photoanode by a successive ionic layer adsorption and reaction (SILAR) method. With the thin ZnS layer, the stability of QDs is largely improved and the recombination in the solar cells is effectively suppressed.[34]

1.4.4.3 Depleted Heterojunction Solar Cells

CQD solar cells reached above 5% PCE for the first time with the advent of the depleted heterojunction architecture (Figure 1-8 b).[35-37] Depleted heterojunction solar cells coat a wide-band-gap semiconductor such as ZnO or TiO_2 with CQDs. In contrast with CQD-sensitized solar cells, and in resemblance with Schottky CQD cells,

CQD depleted heterojunction solar cells exploit transport of electrons and holes through a many-layer CQD film. Now, this ambipolar transport occurs successfully over a distance equal to the sum of a depletion region and a minority carrier diffusion length; typically limiting the current contributing CQD layer thickness to 100~300 nm. While CQD layer can absorb nearly all visible wavelength light in a single pass through this thickness, near-infrared colors are only partially absorbed. This limitation may be termed an absorption versus extraction trade-off arising from electronic transport limits in CQD layers further detailed below.[26]

1.4.4.4 Depleted Bulk Heterojunction Solar Cells

CQD depleted bulk heterojunctions (Figure 1-8 c) provide an architecture solution to this present-day materials limitation: they employ a nanoporous architecture to extend the photon interaction length while maintaining a short exit route for electrons. Electrons, the current-limiting carrier in most CQD solar cells, are collected laterally into the nearest vertical instance of the nanoporous TiO_2 (or ZnO) substrate.[26] In this design, QDs and TiO_2 nanostructures are assembled in such a way to create a certain level of interpenetration. As such, the interfacial area is maximized, and the depletion region can spread in all three dimensions in the active QDs layer. Therefore, in principle, the active layer can be made thicker to absorb more light yet still enable efficient charge carrier collection. ZnO nanowires were also employed into the bulk heterojunction solar cells as an n-type semiconductor to improve the carrier collection.[38-39] For the vertically oriented ZnO nanowires grown by a simple hydrothermal process, J. Jean, et al observed a 35% efficiency enhancement over corresponding planar devices with a maximum efficiency of 4.9%.[17, 39] Six year before, the CQD solar cells usually use CQDs with short bifunctional organic molecules (such as EDT, MPA, BDT etc.) as surface ligand. But those CQDs and solar cells with short organic ligands are unstable when they were exposed in air. J. Tang, et al used halide anions to modify CQDs surface and change CQD's surface ligand, obtained air stable CQDs and solar cells. They found that after halide anions treatment, the trap states in CQDs were reduced and electronic transport parameters in CQD films were enhanced. What's more, the devices can be deposited at room temperature and under ambient atmosphere, rendering the process amenable to low-cost, roll-by-roll

fabrication, and the efficiency of solar cells can reach 6%.[40]

By manipulating the QD's surface ligand in such heterojunction cells, an improved ZnO/PbS-TBAI/PbS-EDT (1,2-ethanedithiol) *n-i-p* solar cell architecture has promoted the PCE of CQDSCs from 7.0% to 9.2%, which was found by Bawendi's group.[41] The high PCE was achieved in TiO_2 (or ZnO)/PbS QD solar cells by engineering the band alignment of PbS-I and PbS-EDT layers.[42-43] PbS-I layers served as the major light-absorbing layer while the PbS-EDT layer acted as a hole extraction layer. The large conduction band offset between those two layers provides an energy barrier to prevent photogenerated electrons from flowing toward the anode, and the large valence band offset offers an additional driving force for the flow of photogenerated holes toward the anode.[17] In those works, the active layer was deposited sequentially in a layer-by-layer process, consisting of 12 layers, each with one ligand-exchange treatment and two washing steps. This multi-step processing makes manufacturing complex, and, additionally, the material is wasted with each layer deposited and treated. Furthermore, the spin-coating and dip-coating techniques are typically only allowed for small-scale batch processing and are incompatible with roll-to-roll manufacturing schemes. Therefore, one step deposition process by using CQDs inks becomes inevitable.[44-46] In this technique, the original surface ligand oleic acid (OA) of CQDs can be replaced by halide precursor though solution state ligand exchange process, as shown in Figure 1-9. The obtain CQDs inks can be deposited on to TiO_2 (or ZnO) substrate by spin-coating or spray-coating method as light absorbing layer of solar cells. Although those solar cells are stable, their PCE are still lower than 4%, which is mainly due to the limited thickness of absorbing layer and low densification.[46]

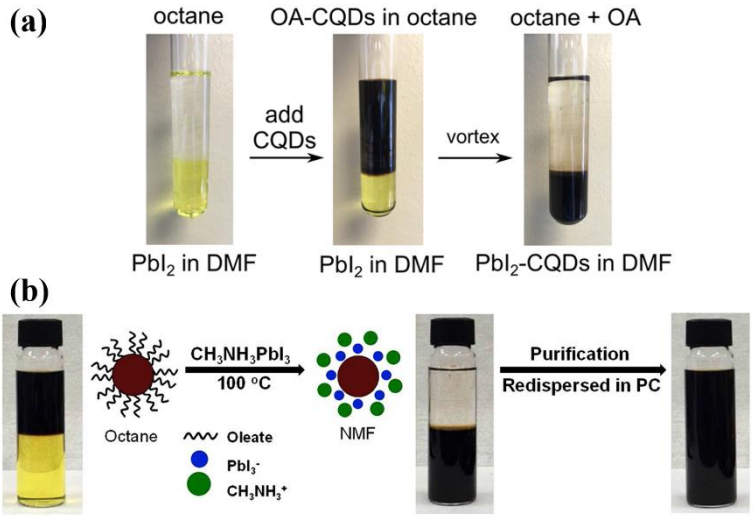

Figure 1-9. Solution state ligand exchange process of CQDs. (a) using PbI_2 as the iodine processor and (b) using perovskite material $CH_3NH_3PbI_3$ as iodine ligand processor.

In summary, CQDs present high extinction coefficients (i. e. PbS thickness of 20 - 30 μm is sufficient to absorb more than 99% from the incident solar radiation)[47], and long wavelength absorption spectra which can be conveniently tuned by controlling their size. Specifically, the demonstration of the multiple exciton generation (MEG) phenomena in CQDs opens the possibility of obtaining quantum efficiencies higher than 100%. CQDSCs have moved forward at a rapid pace in recent years. The credit for these advances goes to synthetic and materials chemists, materials processing groups, and innovators in device architecture. However, CQDSCs also face some challenges such as low charge carrier mobility, high surface trap density, and incomplete mechanistic understanding of transport and recombination. Thus, I focus on the modification of the interface and investigation of the charge carrier dynamics of CQD films and CQDSCs.

1.5 Perovskite Solar Cells (PSCs)

1.5.1 Perovskite Materials and Structure

Perovskite (PVK) was discovered in the Ural Mountains by German mineralogist Gustav Rose and named after Russian nobleman and mineralogist Lev Aleksevich von

Perovski in 1839.[48] The word “perovskite” refers to the mineral form of $CaTiO_3$. It adopts a crystal structure consisting of corner-sharing TiO_6 octahedra in three dimensions, with Ca occupying the cuboctahedral cavity in each unit cell. The same crystal structure is also found for a wide range of materials with ABX_3 stoichiometry, with three notable cases being $BaTiO_3$, $SrTiO_3$, and $NaNbO_3$. Examples of insulating, semiconducting and superconducting PVK structured materials are known. These materials are the archetypal systems for phases transitions with accessible cubic, tetragonal, orthorhombic, trigonal and monoclinic polymorphs depending on the tilting and rotation of the BX_3 polyhedra in the lattice.[49] Reversible phase changes can be induced by a range of external stimuli including temperature, pressure and magnetic or electric fields.[50]

The ideal cubic PVK structure is like a body-centered cubic structure, with additional anions positioned along the faces of the unit cell. The basic stoichiometry is ABX_3, the A site is a cation usually occupied by Group I or Group II of the periodic table. The B site is a cation filled with transition metals, and the X sites are usually occupied by non-metal anions (halide or oxygen). As shown in Figure 1-10, the atoms on the corners of the unit cell are the A site, and the atom in the center of the body is the B site. The atoms on the faces of the unit cell are the X site. The cation B atoms form an octahedron with the six closest X anions, and the cation A atoms form a twelve-fold coordination with the X sites.[51-53]

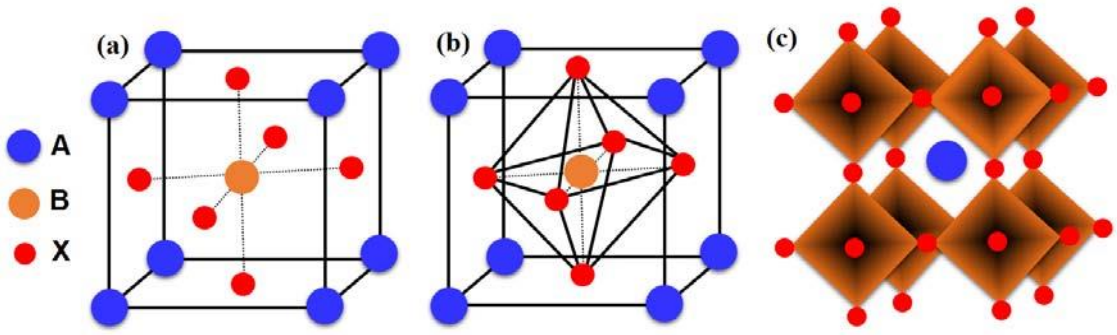

Figure 1-10. Schematic diagram of the ideal PVK structure: (a) the positions of the atoms, (b) the BX_6 octahedron, and (c) the BX_6 octahedron extending in three dimensions around atom A.[54]

The symmetry elements of PVK structure depend on the atomic species that occupy

the A and B sites. Their crystallographic stability and probable structure can be deduced by considering a tolerance factor t and an octahedral factor μ. t and μ are defined as[55]:

$$t = \frac{R_A + R_X}{\sqrt{2}(R_B + R_X)} \qquad (1-16)$$

$$\mu = \frac{R_B}{R_X} \qquad (1-17)$$

where R_A, R_B, and R_X are the corresponding ionic radii of A, B, and X ions. The values of R_A+R_X and R_B+R_X are approximately the distances of A-X and B-X, respectively, and the $\sqrt{2}$ is due to geometric considerations.[54] The value of t is equal to 1 for the ideal cubic PVK structure. If the tolerance factor $t > 1$, the structure tends to distort towards a tetragonal structure, whereas if $t < 1$, a buckling of the octahedron occurs.[56] For halide perovskites (X = F, Cl, Br, I), generally $0.81 < t < 1.11$ and $0.44 < \mu < 0.90$. If t lies in the narrower range 0.89 to 1.0, the cubic structure of Figure 1-10 is likely, with lower t values giving less symmetric tetragonal or orthorhombic structures. Despite these constraints, transitions between such structures on heating are common for any given PVK, with the high-temperature phase generally being cubic.[51]

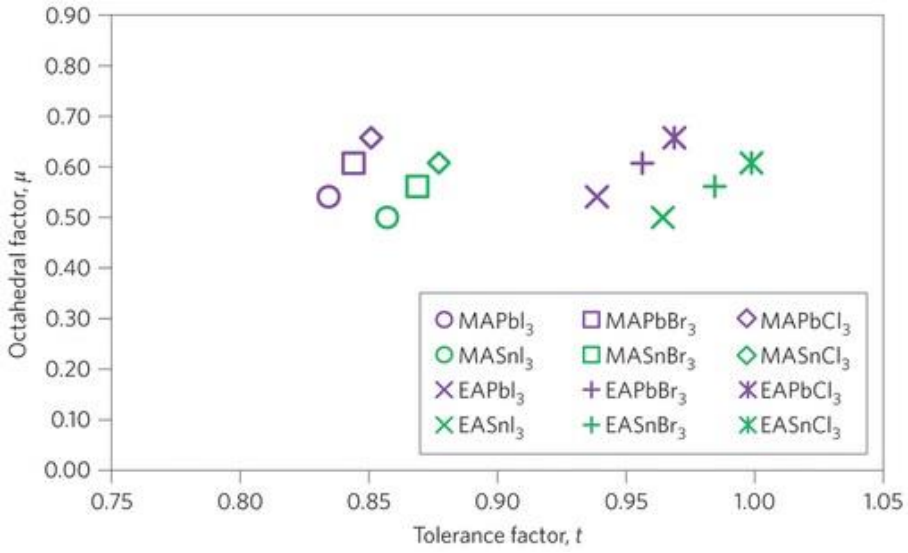

Figure 1-11. Calculated t and μ factors for 12 halide PVKs. The corresponding formamidinium (FA) based halides are expected to have intermediate values between those of the methylammonium (MA) and ethylammonium (EA) compounds shown.[50]

For the organic–inorganic halide PVKs of present interest, the larger cation A is organic. It is generally methylammonium (MA) with R_A = 0.18 nm,[57] ethylammonium (EA) with R_A = 0.23 nm,[58] and formamidinium (FA) with R_A has intermediate values between those of MA and EA, is estimated to lie in the range 0.19–0.22 nm.[51] The anion X is a halogen, generally Cl, Br, and I with R_X =0.181 nm, 0.196 nm, and 0.220 nm, respectively. For efficient cells, cation B usually uses Pb with R_B = 0.119 nm.[59] Calculated and estimated t and μ factors for a range of these PVKs are shown in Figure 1-11.

1.5.2 The Components of PSCs

Perovskite solar cells usually contains four parts: electron transport layer, perovskite light absorbing layer, hole transport material layer, and metal back contract electrode. The architecture diagram and cross section SEM image of PSCs, as shown in Figure 1-12.

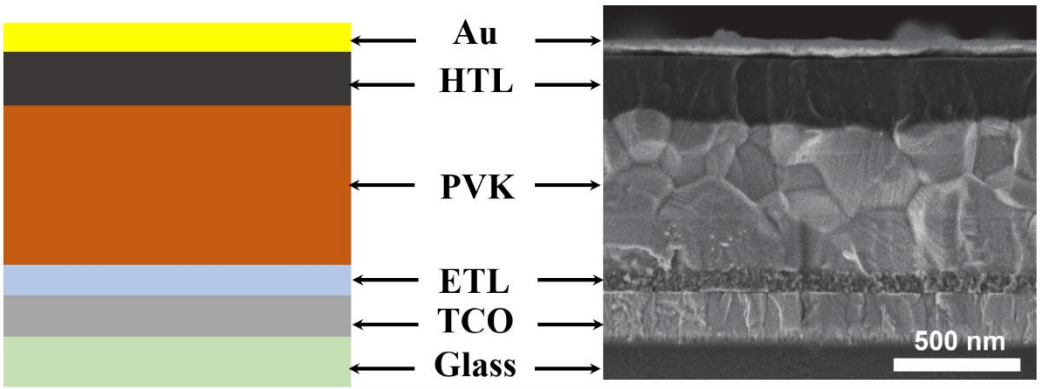

Figure 1-12. Schematic diagram and SEM image of regular *n-i-p* structure PSCs.[60]

1.5.2.1 The Electron Transport Layer

Basically, electron transport layer (ETL) plays a vital role in PSCs for contact selectivity and in optimizing device performance. ETL works as electron selective contact that preferentially extracts electrons to one side of the device and blocks the

direct contact between transparent conductive oxide and hole transporting layer. Besides working as a hole blocking layer, ETL enhances the fill factor and the open circuit voltage of PSCs as the recombination rate is mitigated by electron selective contact between PVK and ETL. Additionally, ETL influences the PVK layer morphology and its loading and controls the quality of PVK/ETL interface and PVK layer itself since ETL provides the intervention in the full PVK transformation from the precursor.[61] For regular *n-i-p* structure PSCs, the TiO_2 mesoporous layer which pores are filled with the PVK material, yield to a higher PCE, and is the most popular structure for PSCs. A thin TiO_2 compact layer has also been used for the PSCs. Compared to TiO_2, the ZnO nanostructure is second in popularity. ZnO is a wide band semiconductor with similar band gap structure to that of TiO_2 but has higher electron mobility. Moreover, high crystalline ZnO films can be grown at low temperature without sintering processes. But due to the corrosion effect of PVK solution on ZnO, ZnO as ETL based PSCs usually using two-step method to prepare PVK layer. D. Liu, et al fabricated the $MAPbI_3$-based solar cell on ZnO planar nanostructure, and got a PCE as high as 15.7% on ITO and 10.2% on a flexible substrate.[62] Park fabricated ZnO nanorod-based perovskite solar cell in the absence of a compact TiO_2 blocking layer with a PCE of 11%.[63] For inverted structure (*p-i-n* structure) PSCs, an organic polymer 6,6-phenyl C61 butyric acid methyl ester (PCBM) also can work as ETL in the hybrid PSCs.[64]

1.5.2.2 The Halide Perovskite Layer

Halide PVK (ABX_3) optical bandgap can be varied by changing the A cation, the B (metal) cation and the halide anion. For the small A cation, such as Cs^+, MA^+ or FA^+, $APbI_3$ prefer to form a three-dimensional framework with PbI_6 network, and an increase in the cation size ($R(Cs^+) < R(MA^+) < R(FA^+)$) results in a reduction in the band gap, since the values are 1.73 eV, 1.58 eV and 1.48 eV for the $CsPbI_3$, $MAPbI_3$ and $FAPbI_3$, respectively. Therefore, a higher efficiency is expected for the $FAPbI_3$ compound compared to $MAPbI_3$.[65] For the influence of the B cation, taking the example of $MABI_3$ (B=Sn, Pb), the band gap of $MASnI_3$ (1.20 eV) is lower than $MAPbI_3$ (1.58 eV).[66] People have investigated the influence of the halide anion, the band gap of this group follows the trend $MAPbI_3$ (1.58 eV) < $MAPbBr_3$ (2.2 eV), but

the efficiency depends on the ratio of I and Br in $MAPbBr_xI_{3-x}$.[66] The energy levels of normally used PVKs are shown in Figure 1-13.

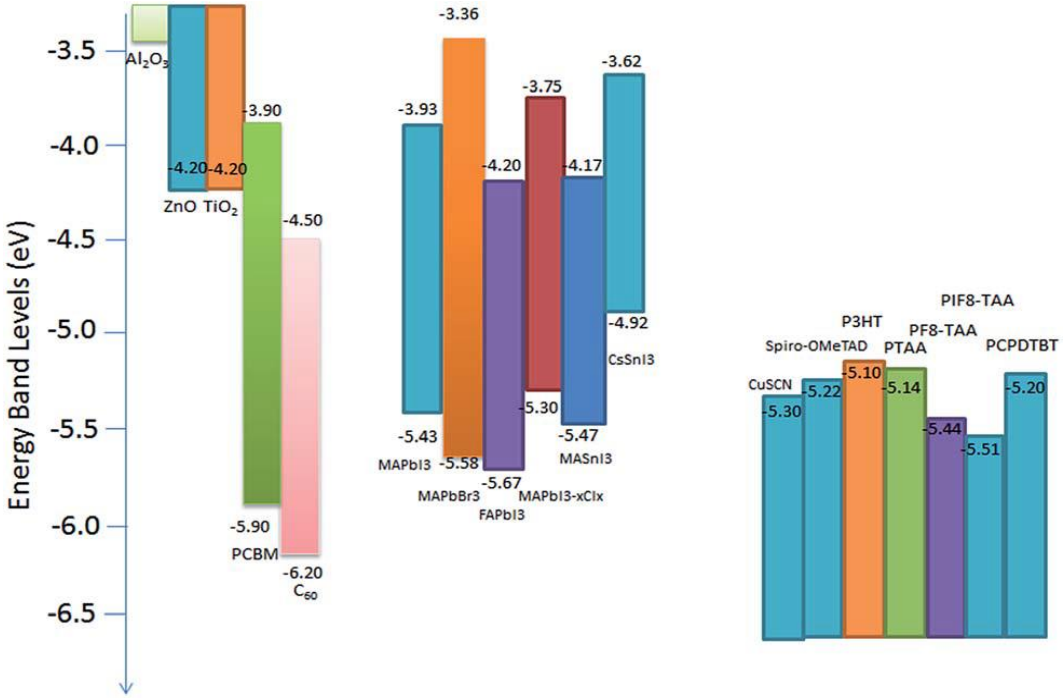

Figure 1-13. Schematic energy level diagram of different materials in PSCs.[67]

The evolution of device efficiencies requires the continuously improving the film quality of crystalline PVK layers, to be uniform, smooth, and pin-hole free etc. There are several commonly used effective methodologies for the access of high quality PVK films as shown in Figure 1-14. Thanks to the sophisticated fabrication methods developed so far, the progress of device efficiencies is approaching its theoretical limitation in single junction PSCs with small area. To push PSCs into real application, the continuous efforts are needed to fabricate high quality crystalline perovskite film into large area with good reproducibility.

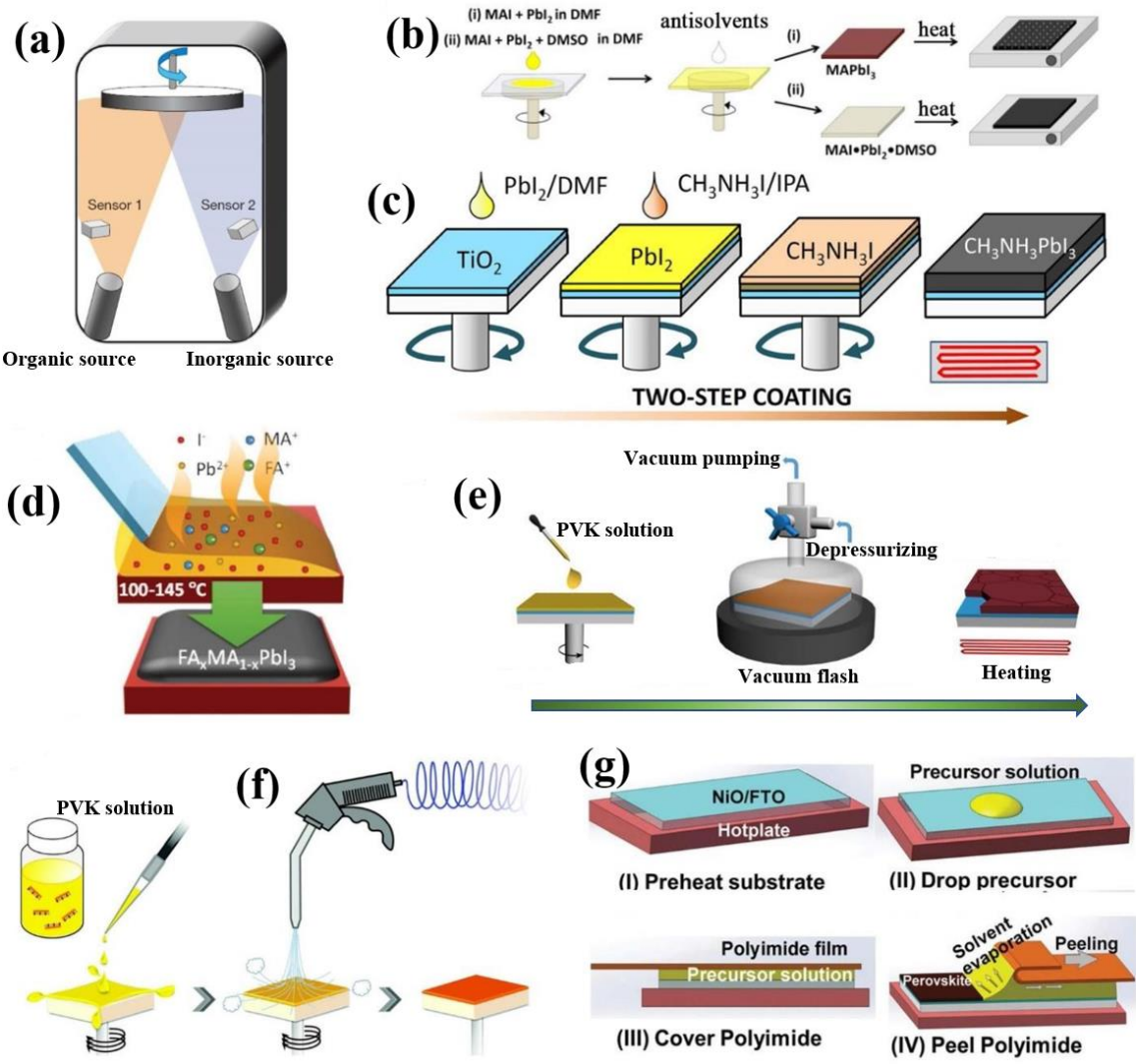

Figure 1-14. Schemes of perovskite deposition: (a) vapor deposition method; (b) anti-solvents method; (c) two-step spin-coating method; (d) doctor-blade coating method; (e) vacuum flash-assisted solution process method; (f) complex-assisted gas quenching method; (g) soft-cover deposition method.[68]

1.5.2.3 The Hole Transport Layer

The hole transport material (HTM) is one of the key components in the solid state solar cells, which is used to transport holes away from the sensitized junction to the back contact of the solar cell. Various materials have been explored as HTM, ranging from low HOMO molecular, polymer, and inorganic component CuSCN, as shown in Figure 1-13. In typical PSCs, the most commonly used hole transport material is 2,2',7,7'-tetrakis-*N*,*N*-di(4-methoxyphenyl)amine-9,9'-spirobifluorene (Spiro-

OMeTAD) which molecular structure is shown in Figure 1-14. Spiro-OMeTAD is an amorphous organic *p*-type semiconductor with a large bandgap and almost colorless when deposited from solution as a thin film on the substrate. The advantage of Spiro-OMeTAD is its good ability to pore filling due to the high solubility in toluene and chlorobenzene organic solvent. Pristine Spiro-OMeTAD has high resistivity and needs to be partially oxidized to decrease the intrinsic charge-transport resistance of the bulk material. This has been achieved through the addition of chemical *p*-type dopants or through the facile oxidation of the material in the presence of oxygen and light. Besides Spiro-OMeTAD, other molecule HTM were synthesized and introduced in PSCs, their molecular structures are shown in Figure 1-15.

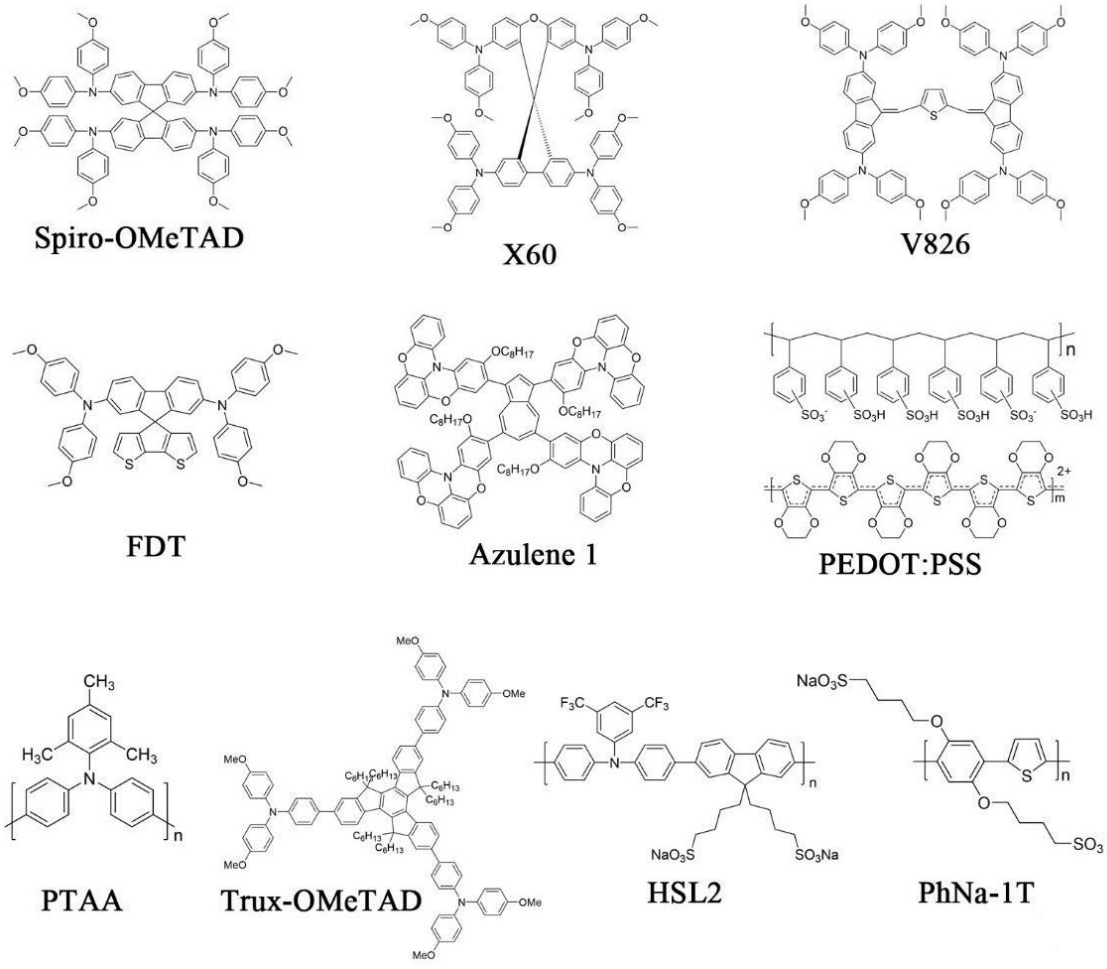

Figure 1-15. Molecular structures of efficient HTM.[68]

Due to the low conductivity of pristine Spiro-OMeTAD and other HTMs, they usually require additive doping for efficient hole extraction and transport. The

common additives are: 4-tert-butylpyridine (t-BP), bis(trifluoromethylsulfonyl)imide lithium salt (LiTFSI) attributed. Usually, the effect of the t-BP is believed to be an upward shift of the TiO_2 (or ZnO) conduction band or reduce the electron-hole recombination rate, which leads to a high V_{oc}.[69] In contrast, the effect of an addition of LiTFSI is a downwards shift of the metal oxide and accelerate the electron injection. The result is an increase in J_{sc}.[70]

1.5.2.4 The Back Contact

The back contact in the typical PSCs is high conductivity metal thin film formed by thermal evaporation method. The silver is more used than gold, which is due to a lower cost and a higher conductivity. Another benefit is the higher reflectivity induced to a higher J_{sc}.[71] Compared to the expensive gold and silver contacts, the low-cost carbon materials have attracted some attention especially with the layer preparation by screen printable deposition technique.[72] Moreover, the carbon layer can work as a water repellent layer to protect the cell from water, which is an important point for the stability of PSCs device.[73]

Table 1-1. Summary of the highest *PCE* of PSCs with different compositions.[68]

Device structure	**PVK**	J_{sc} **(mA/cm^2)**	V_{oc} **(V)**	***FF* (%)**	***PCE* (%)**
ITO/PTAA/PVK/C_{60}/BCP/Au	$MAPbI_3$	24.0	1.11	78.0	20.7
FTO/bl-TiO_2/mp-TiO_2/PVK/PTAA/Au	$FAPbI_3$	24.7	1.06	77.5	20.2
ITO/PTAA/PVK/ICBA/C_{60}/BCP/Au	$MA_{0.6}FA_{0.4}PbI_3$	23.0	1.03	77.0	18.3
FTO/SnO_2/C_{60}-SAM/PVK/Spiro-OMeTAD/Au	$Cs_{0.2}FA_{0.8}PbI_3$	22.2	1.09	80.8	19.6
FTO/bl-TiO_2/mp-TiO_2/PVK/Spiro-OMeTAD/Au	$Cs_{0.15}FA_{0.83}Pb(I_{0.83}Br_{0.17})_3$	22.8	1.153	76.0	20.0
FTO/bl-TiO_2/mp-TiO_2/PVK/Spiro-OMeTAD/Au	$FA_{0.81}MA_{0.15}Pb_{2.51}Br_{0.45}$	24.6	1.16	73.0	20.8
FTO/bl-TiO_2/mp-TiO_2/PVK/PTAA/Au	$Cs_{0.05}(MA_{0.17}FA_{0.83})_{0.95}Pb(I_{0.83}Br_{0.17})_3$	23.5	1.15	78.5	21.1
FTO/bl-TiO_2/mp-TiO_2/PVK/Spiro-OMeTAD/Au	$Rb_{0.05}[Cs_{0.05}(MA_{0.17}FA_{0.83})_{0.95}]_{0.95}Pb(I_{0.83}Br_{0.17})_3$	22.7	1.18	81.0	21.6

1.5.3 Advantages and Challenges of PSCs

PVK has some outstanding advantages such as high absorption coefficients, high extinction coefficients, tunable band gap, direct band gap, high stability, and high carrier mobility. Moreover, PVK is not fabricated by expensive, complicated techniques; instead, easy, low temperature methods may be used, such as solution-processing, thermal evaporation, or printer-based processes. Although the highest certified PCE of PSCs surpassed 22% in small areas,[6] the stability and the toxicity of lead remain big challenges. Chemical and structural instability of PVKs are the main culprit of the vulnerability for device operational stabilities. The compositional engineering of perovskites showed the encouraging progresses to address such issues. Although some materials are fairly stable within a few months, there is still a distance to make them and the related devices stable into decades under environmental stresses. Device approaches such as blocking layers and encapsulation are also needed to tackle these issues. With optimism minds, the stabilities for PSC may eventually allow reaching the prerequisites for practical application. Studies of lead-free perovskites implied the simple substitution of lead to other metal cations in new PVKs usually led to decline device efficiency. Although Sn-Pb based PVKs promises a fairly high efficiency,[74-75] Sn faces unstable issues and some reports indicate that Sn even has larger impact to human and environment than that of Pb.[76] Alternatively, Bi-based halide double perovskite would be worth to pay more attention with, because it has 3D structure with good stability, as well as Bi displays a similar electronic structure to Pb.[77-78] To address environmental issues of PSCs, attentions can also be involved to develop excellent capsulation and recycling of PSCs for avoiding the leakage of lead. To develop lead-free perovskite with high efficiency, there remain significant challenges.

1.6 Thesis Focus

This thesis will investigate the surface ligand dependent charge carrier dissociation, charge carrier transmission and recombination of CQDSCs, and use novel hole transport materials to modify the interface of CQDSCs and PSCs to reduce the interfacial recombination in CQDSCs and PSCs. The goal of all of these experiments

is to gain a more complete understanding of charge carrier dynamics in CQDSCs and PSCs, so that more efficient materials and architecture for solar cells can be designed in the future.

The second chapter will provide an introduction of characterization equipment and technologies which were used in this thesis.

The third chapter explores a method how to obtain air stable PbSe CQDs and surface ligand dependent exciton dissociation, recombination, photovoltaic property, and stability of PbSe solid film and CQDSCs. I select four short ligands, that is, two organic ligands 1,2-ethanedithiol (EDT) and 3-mercaptopropionic acid (MPA); two inorganic ligand cetyltrimethylammonium bromide (CTAB) and tetrabutylammonium iodide (TBAI) to investigate the ligand-dependent air stability, energy level shift, the exciton dissociation, and photovoltaic properties of PbSe CQDSCs. In addition, the charge transfer rate, recombination processes and carrier lifetimes in these CQDSCs were also revealed through ultrafast transient absorption (TA) spectra, and open-circuit transient voltage decay measurements. **The originalities of this work are**: (1) TBAI was used to exchange original surface ligand OA of PbSe QDs for the first time; (2) long-term air stable PbSe based QDSCs was obtained. Part of this chapter was published in *The Journal of Physical Chemistry C*, 2016, 120, 28509-28518.

The fourth chapter explores a method to suppress the interfacial recombination in CQDSCs. we develop a novel donor-π-donor (D-π-D) organic small molecule bis-triphenylamine with spiro(fluorene-9,9'-xanthene) as the conjugated system, named BTPA-4, as a hole transport layer in the PbS CQDSCs. We found that the introduction of BTPA-4 as hole transport layer can enhance the open-circuit voltage, prolong the effective carrier lifetime, reduce the interfacial recombination at PbS QDs/Au interface, and hence improve the device performance. Furthermore, the PbS CQDSCs with BTPA-4 possessed a noticeably stable property for over 100 days of storage under ambient atmosphere that has been the Achilles' heel of other organic hole transport layer for CQDSCs. **The originalities of this work are**: (1) novel hole transport material BTPA-4 was synthesized; (2) organic small molecule was used to suppress the interfacial recombination in QDSCs for the first time. Part of this chapter was published in *The Journal of Physical Chemistry Letters*, 2017, 8, 2163-2169.

The fifth chapter will focus on hole transport material and the interfacial recombination in PSCs. Three triphenylamine-based hole-transport materials (HTMs), named BTPA-4, BTPA-5 and BTPA-6, were used into PSCs. BTPA-6 with four substituted triphenylamine units exhibited a better solar cell performance than BTPA-4 and BTPA-5 which contain two substituted triphenylamine units. The order of the recombination resistance was found to be in the order of BTPA-4 < BTPA-5 < BTPA-6 < Spiro-OMeTAD, indicating that the electron blocking capability of the HTM is in this order. This trend agrees with the V_{oc} trend of their corresponding solar cells. In addition, BTPA-6 based devices showed better long-term stability than that with Spiro-OMeTAD, which can partially be attributed to the hydrophobicity of BTPA-6 is better than that of Spiro-OMeTAD. **The originalities of this work are**: (1) low cost hole transport materials BTPA-5 and BTPA-6 were synthesized; (2) BTPA-4, BTPA-5, and BTPA-6 were used to be as hole transport layer in perovskite solar cells for the first time.

The sixth chapter will summarize the problems existing in the research and give the future development prospects of QDSCs and PSCs.

Chapter 2: Characterization

2.1 X-ray Power Diffraction

X-ray powder diffraction, which is usually shorted for XRD, is a rapid analytical technique primarily used for phase identification of a crystalline material and can provide information on unit cell dimensions. The analyzed material is finely ground, homogenized, and average bulk composition is determined. In this thesis, an X-ray powder diffraction (TTR-III, Rigaku Corp., Japan) was used to identify the phase and crystallization of QDs.

2.2 UV-Vis-NIR Spectroscopy

Ultraviolet-Visible-Near Infrared (UV-Vis-NIR) Spectroscopy can present the absorption or reflectance spectra in the UV-Vis-NIR spectral region from 200 nm to 2000 nm. The absorption or reflectance properties of the chemicals in the visible region directly affect the observed color of the chemicals involved. In this visible region, atoms or molecules undergo electronic transitions, which main that the molecules including non-bonding electrons (n-electrons) or π-electrons can absorb the energy of light with exciting these electrons to higher anti-bonding molecular orbitals. Thus, it can be concluded that the more easily excited the electrons (i.e. smaller E_g between the HOMO orbital and the LUMO orbital), the longer the wavelength of light it can absorb due to the inverse proportion of the energy and the wavelength. Besides, UV-Vis-NIR spectroscopy can also be well used in analytical chemistry for the quantitative analysis, such as the determination of molar extinction coefficient, thickness or optical properties of thin films. In this thesis, all the UV-vis-NIR absorption spectra were obtained by using a UV−Vis-NIR spectrophotometer (JASCO, V-670).

2.3 Fluorescence Spectroscopy

Fluorescence (FL) spectroscopy can present electromagnetic fluorescence information from a sample which has been excited by. Using a beam of light and the

causes itself to emit light. FL spectroscopy is greatly closed to the molecular electronic and vibrational states. Noticeably, there are various vibrational states in each electronic states including the electronic ground state and the electronic excited state. In detail, some molecules are firstly excited, by absorbing the photons from the ground electronic state with higher energy to one of the various vibrational states in the excited electronic state with higher energy. After that, collisions with other adjacent molecules cause the excited molecules to lose vibrational energy or transfer conversion of this vibrational energy to heat until it reaches the lowest vibrational state of the excited electronic state. The PL process can be subsequently generated after the molecule falls back to one of the various vibrational levels of the ground electronic state again. Thus different energies will be produced as molecules may fall back into any of several vibrational levels in the ground electronic state, and thus different frequencies. Interestingly, by investigating the different frequencies of light emitted in the fluorescent spectroscopy, as well as their relative intensities, the structure diagram of the different vibrational levels can be determined. In this thesis, the fluorescence spectroscopy measurement was conducted by using LabRAM HR-800 (HORIBA, Japan).

2.4 Fourier Transform Infrared Spectroscopy

Fourier transform infrared spectroscopy (FT-IR) can provide an infrared spectrum of a solid, liquid or gas by utilizing different wavelengths in near infrared region to investigate the molecular structure, which reveals the molecular vibrational and rotational energies. The components of FT-IR spectrometers commonly are IR sources, detectors, beam splitter, attenuated total reflectance (ATR) and fast Fourier transform (FFT) algorithm. FT-IR spectroscopy is used in geology, chemistry, materials and biology for and research fields. In this thesis, the FT-IR spectra (Thermo Scientific, Nicolet 6700, Japan) of the PbSe QDs films were measured to verify that the as-synthesized ligand (OA) on PbSe QDs were successfully exchanged.

2.5 Ultrafast Transient Absorption Spectra

Ultrafast transient absorption (TA) spectroscopy, an example of non-linear

spectroscopy, monitors the change in the absorbance or transmittance in the sample. Here, the absorbance at a particular wavelength or range of wavelengths of a sample is measured as a function of time after excitation by a flash of light. In a typical experiment, both the light for pump and probe light are generated by a pulsed laser. If the process under study is slow, then the time resolution can be obtained with a continuous (i.e., not pulsed) probe beam and repeated conventional spectrophotometric techniques. TA spectroscopy relies on our ability to resolve two physical actions in real time. The shorter the detection time, the better the resolution. This leads to the idea that femto-second laser based spectroscopy offers better resolution than nano-second laser based spectroscopy. In this thesis, TA spectra were examined by using a fs-TA system. The laser source was a Ti/sapphire laser (CPA-2010, Clark-MXR Inc.) with a wavelength of 775 nm, a pulse width of 150 fs, and a repetition rate of 1 kHz.

2.6 X-ray Photoelectron Spectroscopy

X-ray photoelectron spectroscopy (XPS) is a surface-sensitive quantitative spectroscopic technique that measures the elemental composition at the parts per thousand range, empirical formula, chemical state and electronic state of the elements that exist within a material. XPS spectra are obtained by irradiating a material with a beam of X-rays while simultaneously measuring the kinetic energy and number of electrons that escape from the top 0 to 10 nm of the material being analyzed. XPS can be used to analyze the surface chemistry of a material in its as-received state, or after some treatment. In this thesis, XPS measurement was conducted to identify the presence of short ligands within the PbSe QD films after ligand exchange. The measurement was carried on JEOL JPS-9200.

2.7 Photoelectron Yield Spectroscopy

The information on the electronic structures of semiconductors can be revealed by using photoelectron yield spectroscopy (PYS). In PYS, the quantum yield of photoelectron (Y), which stands for the number of emitted photoelectrons per photon absorbed, is detected as a function of incident photon energy. If incident photon energy

becomes greater than the threshold ionization energy of a semiconductor during incident photon scan, the value of Y starts to increase. Thus, by determining the threshold of the spectrum, the value of threshold ionization energy can be evaluated. In the case of metal sample, the work function of the sample can be deduced in similar way. Comparing with ultraviolet photoelectron spectroscopy (UPS), PYS is available not only in vacuum but also in air, and sample charging can be practically avoided.[79] In this thesis, the PYS of the PbSe and PbS films were obtained by employing a BIP-KV205 Model ionization energy measurement system.

2.8 Electron Microscope

An electron microscope is generally used to reveal the morphology, size and the distribution of a wide range of biological and inorganic specimens by using a beam of accelerated electrons as a source of illumination. As the wavelength of an electron can be up to 100,000 times shorter than that of visible light photons, electron microscopes have a higher resolving power than light microscopes and can reveal the structure of smaller objects. In this thesis, the morphologies of solar cell were examined using a scanning electron microscope (SEM, JEOL, JSM-6340). The sizes of PbSe and PbS QDs, and distance between ligand treated PbSe QDs were determined by transmission electron microscope (TEM, JEOL, JEM-2100F).

2.9 Characterization of Solar Cells' Performance

The current density−voltage ($J-V$) curves were carried out in the dark or under AM 1.5 G irradiation (100 mW cm^{-2}), with a Peccell solar simulator PEC-L10 by using a Keithley 2400 source meter. Incident photon to current conversion efficiency (*IPCE*) spectra of CQDSCs were measured by using a 300 W Xe arc lamp, which was equipped with a Nikon G250 monochromator. The transient V_{oc} decay curves were obtained by using a pulsed YAG laser (wavelength 532 nm, repetition rate 4 Hz, pulse width 5 ns). The impedance spectroscopy (IS) measurements of CQDSCs were obtained by applying the bias from 0 to 0.45 V (amplitude 10 mV) with a frequency ranging from 1M Hz to 1 Hz on a SP-300 (BioLogic) impedance analyzer.

Chapter 3: Ligand Dependent Charge Dynamics in Air Stable PbSe Quantum Dot Films and Solar Cells

3.1 Introduction

Colloidal quantum dots (CQDs) have attracted immense attention in the past decades owing to their unique size-dependent properties and low-cost solution process ability.[80-84] This makes CQDs promising in various applications such as light emitting diodes (LEDs),[85-86] field effect transistors (FETs),[82, 87-89] biolabeling,[90-92] lasers[93-95] and solar cells[96-98]. Recently, colloidal quantum dot solar cells (CQDSCs), which are facile to prepare by simple spin-coating procedure with low fabrication cost, have attracted increasing scientific and industrial interests as a promising candidate for the next generation solar cells. Among them, CQDs present high extinction coefficients, and long wavelength absorption spectra which can be conveniently tuned by controlling their size. Specifically, the demonstration of the multiple exciton generation (MEG) phenomena in CQDs opens the possibility of obtaining quantum efficiencies higher than 100%, that is, more than one electron generated per absorbed photon at a broad wavelength range across the solar spectrum.[99-102] As predicted by Nozik and co-workers, the theoretical power conversion efficiency (PCE) of QDSCs can achieve as high as 44% due to MEG which is higher than the theoretical efficiency of single junction solar cells (Shockley Queisser limit).[103] Recently, PbS CQDSCs have been reported with certified PCE of 13.4% and Zn-Cu-In-Se QDs sensitized solar cells have achieved a certified PCE as high as 11.6%.[104-105] However, the efficiencies are still much smaller than the theoretical efficiency. Therefore, fundamental studies on the mechanism for improving the photovoltaic properties of CQDSCs are of great importance and necessary.

Specifically, PbSe QDs have attracted attention because of their small bulk bandgap (0.26 eV),[106] high dielectric constant (ε_m = 23),[107] and large exciton Bohr radius (46 nm) which is two times higher than that of PbS (23 nm).[108-109] What's more, it has been reported that PbSe QDs have more efficient MEG than PbS QDs due to their slower hot carrier cooling rate,[110] and PbSe CQDSCs have been confirmed

with a peak external quantum efficiency of 114%.[80] Unfortunately, PbSe CQDs are highly susceptible to oxidation which results in uncontrollable changes in their optical and electronic properties,[108, 111] thus making the performance of PbSe CQDSCs tend to quickly degrade after the solar cells exposed to air environment. Therefore, the fabrication process and the necessary measurements for PbSe CQDSCs must be in the air free environment as reported up to now.

It is no doubt that air stability is a major constraint factor on the development of PbSe CQDSCs. Recently, halide treatments have been identified as a viable method to improve the air stability of PbSe CQDs colloidal solution and film.[108-109, 111-112] For PbSe CQDSCs, Asil et al. injected cadmium chloride ($CdCl_2$) into PbSe reaction solution after PbSe CQDs growth period to form a $PbCl_2$ surface passivation layer outside PbSe, and obtained air stable PbSe CQDs and solar cells. But their solar cells were encapsulated in the devices fabrication process, so these solar cells are not really exposed to air.[113] Beard's group used Pb-halide precursors as the source of Pb^{2+} to get air stable halide ligand treated PbSe CQDs through complicated cation-exchange reactions.[114-116] The best PCE of the PbSe CQDSCs in his group was reached 6.47% and the solar cell had a 5.9% PCE after 50 days of storage in air.[115] But all of these solar cell devices were measured in an inert atmosphere not in air. So far, PbSe CQDSCs have not been implemented the whole process in ambient atmosphere: from PbSe CQDs washing step to solar cells fabrication, storage and measurements. In addition, charge transfer and recombination mechanism in PbSe CQDSCs are also not clear.

In this chapter, I described an improved simple method for fabricating air stable PbSe heterojunction CQDSCs using rarely reported tetrabutylammonium iodide (TBAI) as ligand source in solid state ligand-exchange process. The solar cells with simple structure (TiO_2 compact layer/PbSe/Au) and relatively larger active area (0.25 cm^2, a mask of 0.16 cm^2 was used when measuring photovoltaic performance) compared to most of the reported PbSe CQDSCs (about 0.01-0.06 cm^2) were fabricated by spin-coating method in ambient atmosphere.[101, 109, 115] The PCE of TBAI-treated PbSe CQDSCs was over 3.5% which measured in air, and the solar cells possessed a remarkable long term stability of more than 90 days of storage in ambient

atmosphere. We compared TBAI with the other three short ligands, i.e., 1,2-ethanedithiol (EDT), 3-mercaptopropionic acid (MPA) and cetyltrimethylammonium bromide (CTAB), to investigate the ligand-dependent air stability, energy level shift, the exciton dissociation, and photovoltaic properties of PbSe CQDSCs. In addition, the charge transfer rate, recombination processes and carrier lifetimes in these CQDSCs were also revealed through ultra-fast transient absorption (TA) spectra, and open-circuit transient voltage decay measurements.

3.2 Experimental Methods

Materials. Lead(II) oxide (PbO, Wako, 99.5%), oleic acid (OA, Aldrich, 90%), 1-octadecene (ODE, Aldrich, 90%), trioctylphosphine (TOP, Aldrich, technical grade 90%), selenium (Se, Wako, 98%), cadmium chloride ($CdCl_2$, Wako, 95%), tetradecylphosphonic acid (TDPA, Aldrich, 97%), oleylamine (OLA, Aldrich, 70%), Titanium diisopropoxide bis(acetylacetonate) (Aldrich, 75 wt.% in isopropanol), 1,2-ethanedithiol (EDT, Aldrich, 98%), 3-mercaptopropionic acid (MPA, Aldrich, 99%), cetyltrimethylammonium bromide (CTAB, Wako, 98%), tetrabutylammonium iodide (TBAI, Wako, 98%), Tetrachloroethene (TCE, Wako, 99%). These materials were used as received from commercial sources without any purification.

Synthesis of PbSe CQDs. PbSe CQDs were synthesized following a similar literature method,[113] but modified as a simple process in our paper. Briefly, 6 mmol PbO and 15 mmol OA were mixed with 30 mL ODE in a 100 mL three-neck flask. The mixture was stirred and degassed at room temperature for 0.5 h and then at 100°C for 1 h. The solution was then heated to 130°C under nitrogen for another 2 h. 18 mL of 1 M TOP-Se solution (Se powder dissolved in TOP) was then rapidly injected to the above lead oleate solution at 90°C. After 3 min, the heater was removed immediately while stirring of the solution was maintained. When the solution was cooled to 75°C, a $CdCl_2$-TDPA-OLA solution containing 1 mmol $CdCl_2$, 0.1 mmol TDPA, and 3 mL OLA was injected into the colloidal PbSe solution. After quickly cooling down to room temperature, the PbSe CQDs were isolated from the reaction solution by using acetone/methanol/hexane solvent system in air, and this purification process was repeated for three times. After purification, the obtained PbSe CQDs precipitate was

then dried by an air flow and dispersed in octane at a concentration of 50 mg/mL and stored in ambient atmosphere.

PbSe QDs Film Fabrication. The PbSe CQDs were deposited on glass substrates by a typical layer-by-layer spin-coating method using a fully automatic spincoater.[117] Each cycle was consisted of three steps: PbSe deposition, ligand exchange, and solvent rinse. Generally, colloidal PbSe (100 μL) was dropped onto glass substrates and spun-cast at 2500 rpm for 15 s. Then, the ligand solution (0.02% vol EDT in acetonitrile, 30 mM MPA in methanol, 30 mM CTAB (as Br^- source) in methanol, and 30 mM TBAI (as I^- source) in methanol) was dropped onto the substrate and spun dry after a 60 s wait. The substrate was then rinsed three times with methanol (acetonitrile for EDT) to remove excess unbound ligands.

Photovoltaic Device Fabrication. To fabricate PbSe CQDSCs, fluorine-doped tin oxide (FTO) patterned glass substrates were cleaned through sequential ultrasonic treatment with ethanol, acetone, isopropanol and deionized water. The washed FTO glass substrates were further cleaned with oxygen plasma for 15 min before use. FTO/TiO_2 substrate was made by spinning 0.3 M Titanium diisopropoxide bis(acetylacetonate) in 1-butanol solution on FTO substrate. In other words, 200 μL Ti^{4+} solution was dropped on FTO glass substrates (2.5×2.5 cm) and spin-coating at 3000 rpm for 30 s, followed by annealing at 450°C for 30 min in air. The PbSe CQDs were deposited on FTO/TiO_2 substrates by spin-coating method same as PbSe films fabrication. Finally, 100 nm Au top electrode was deposited onto the PbSe layer by thermal evaporation through a shadow mask to create four identical cells on each substrate, each solar cell with an active area of 0.25 cm^2.

3.3 Results and Discussion

3.3.1 Different Sizes PbSe QDs

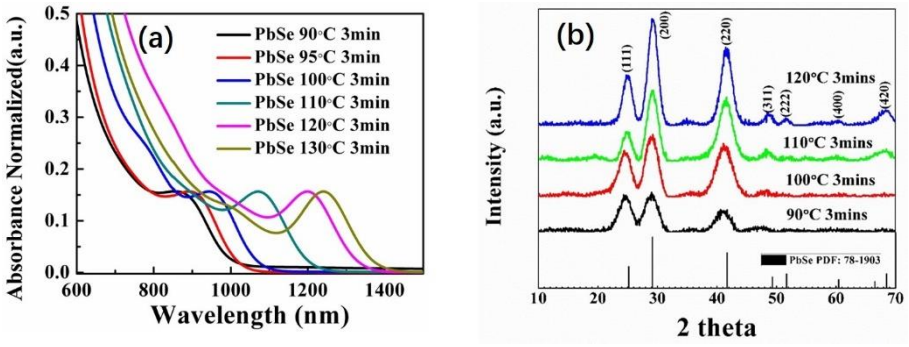

Figure 3-1. Normalized absorbance of PbSe QDs (a) and XRD patterns of PbSe QDs (b) synthesized at different temperature.

Figure 3-1a shows the normalized absorbance of PbSe QDs synthesized under different injection temperatures. With the injection temperature increasing, the first exciton peak of PbSe QDs shifts from 858 nm (90 ºC) to 1241 nm (130 ºC). It indicated that the sizes of PbSe QDs are increased with the injection temperature. According the empirical formula between the sizes and first exciton peak position of PbSe, the sizes of PbSe QDs can be estimated.[118] The data was shown in Table 3-1.

$$D = \frac{\lambda - 143.75}{281.25} \qquad (3-1)$$

Table 3-1. The first exciton peak positions and calculated sizes of PbSe QDs which were synthesized at different temperature.

Synthesized temperature (ºC)	90	95	100	110	120	130
First exciton peak (λ, *nm*)	858	892	943	1071	1199	1241
Calculated size (*D, nm*)	2.54	2.66	2.84	3.30	3.75	3.90

Figure 3-1b presents the XRD spectra of PbSe QDs which synthesized at different temperature. All the diffraction peaks are characteristic of cubic PbSe structure (space group Fm-3m, JCPDS 78-1903). With the synthesis temperature of PbSe increasing, the half-width of peaks becomes narrow which indicates that the crystallinity and sizes of PbSe QDs are increased.

3.3.2 Optical Properties, Stability and Assembly of PbSe QDs

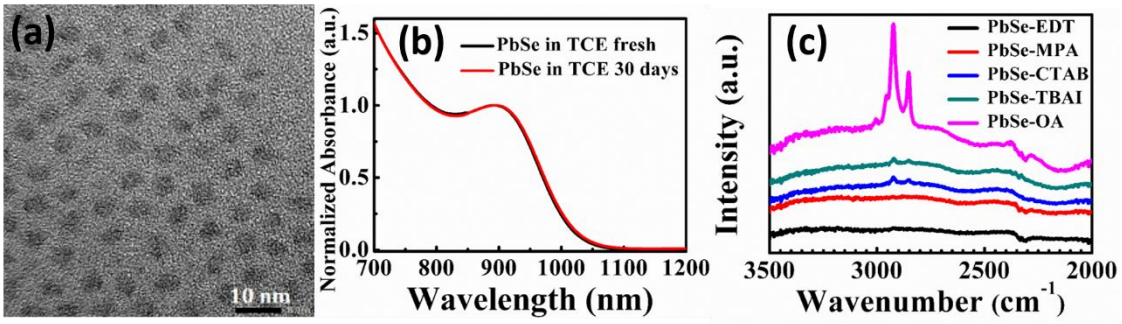

Figure 3-2. Transmission electron microscopy (TEM) image of PbSe CQDs (a). Absorption spectra of PbSe CQDs dispersed in TCE solution measured soon after preparation and after storing in air for 30 days (b). FT-IR spectra of PbSe QDs films capped with different ligands (c).

PbSe CQDs with OA capping ligands synthesized by a simple method were shown in the experimental section. The average size of PbSe CQDs is approximately 2.9 nm in diameter, as shown in Figure 3-2a. Figure 3-2b shows optical absorption spectra of the monodisperse PbSe CQDs in TCE. The first exciton absorption peak of PbSe CQDs in TCE is about 910 nm, which corresponds to its band gap energy of 1.37 eV. After stored in air 30 days, there was not any significant change in the optical absorption spectra for PbSe CQDs TCE solution, indicating that $CdCl_2$ surface passivation technique is an effective method to improve the stability of PbSe CQDs colloidal solution. FT-IR spectra of PbSe QDs films treated with different ligands on Au coated glass substrates which are fabricated by spin coating method are given in Figure 3-2c. FT-IR measurements demonstrated that the C-H absorption stretching peaks at 2961, 2929, and 2854 cm^{-1} for the films with short ligand treatments were significantly reduced. What's more, the =C-H stretching peak at 3006 cm^{-1} belonged to OA disappeared, which suggested that OA ligands were successfully removed during ligand exchange process and replaced by short ligands. This is further confirmed by the XPS measurements. As shown in Figure 3-3, the clear peaks corresponding to sulfur, Br and I (S 2p, Br 3d and I 3d) could be observed, respectively. From what has been discussed above, we can draw the conclusion that PbSe QDs within the films were completely packed by short ligands after ligand exchange

process.

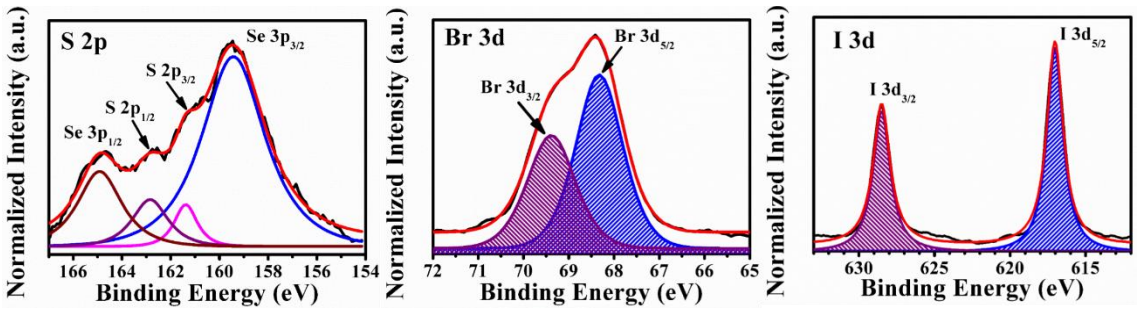

Figure 3-3. High-resolution XPS spectra of S 2p, Br 3d and I 3d region of EDT, CTAB and TBAI treated PbSe QDs, respectively.

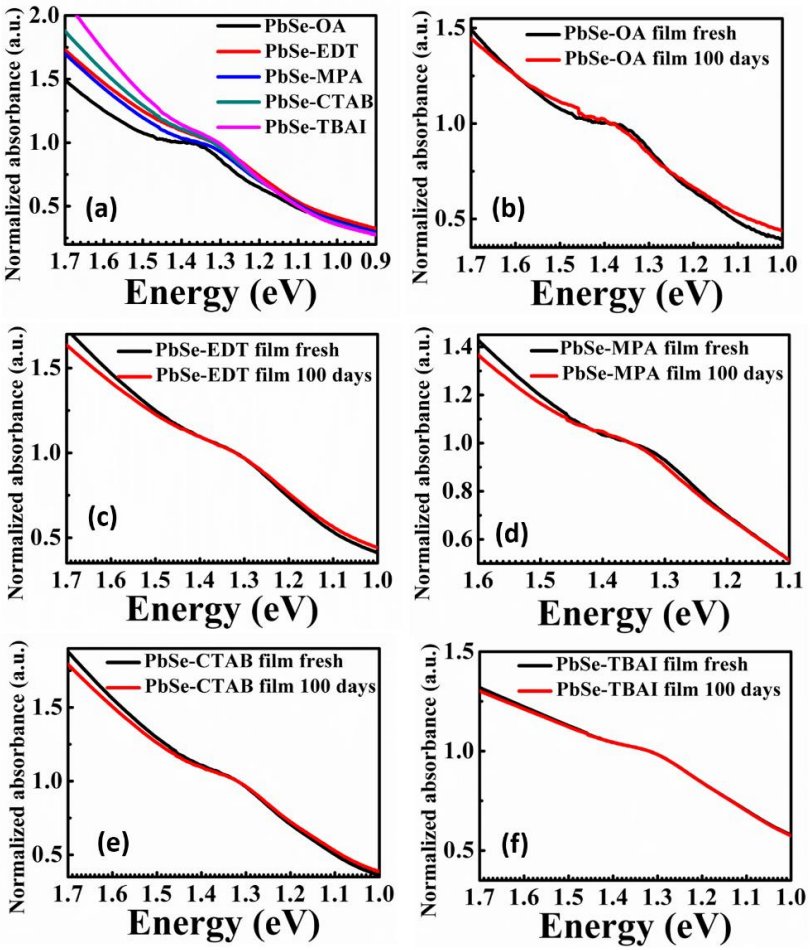

Figure 3-4. Normalized absorption spectra of PbSe QDs thin films capped with difference ligands (a), and after stored in air and dark condition for 100 days (b-f).

Figure 3-4a presents the normalized absorption spectra of PbSe QDs thin films capped with different ligands. The first exciton peak of PbSe-OA film was located at

1.36 eV which was similar to that of PbSe CQDs in TCE. Moreover, after ligand exchanging, the first exciton peak of MPA treated PbSe QDs film moved to 1.33 eV and PbSe QDs films treated with EDT, CTAB and TBAI exhibited their first exciton peak near at 1.32, 1.32, and 1.31 eV respectively. Compared with PbSe-OA film, the red shift of the first exciton peaks of PbSe QDs films treated with short ligands are caused by the narrowed distance among PbSe QDs[119], as shown in Figure 3-5 (the average QD-QD distances were calculated as 3 nm, 1 nm, 1 nm, 0.5 nm and 0.5 nm for OA, EDT, MPA, CTAB, and TBAI ligands, respectively), which leads to strengthened dipole-induced dipole interaction, enlarged wave function delocalization and increased dielectric constant of the surrounding medium, in turn results in enhanced packing densities and conductivities of the PbSe QDs films.[120-122]

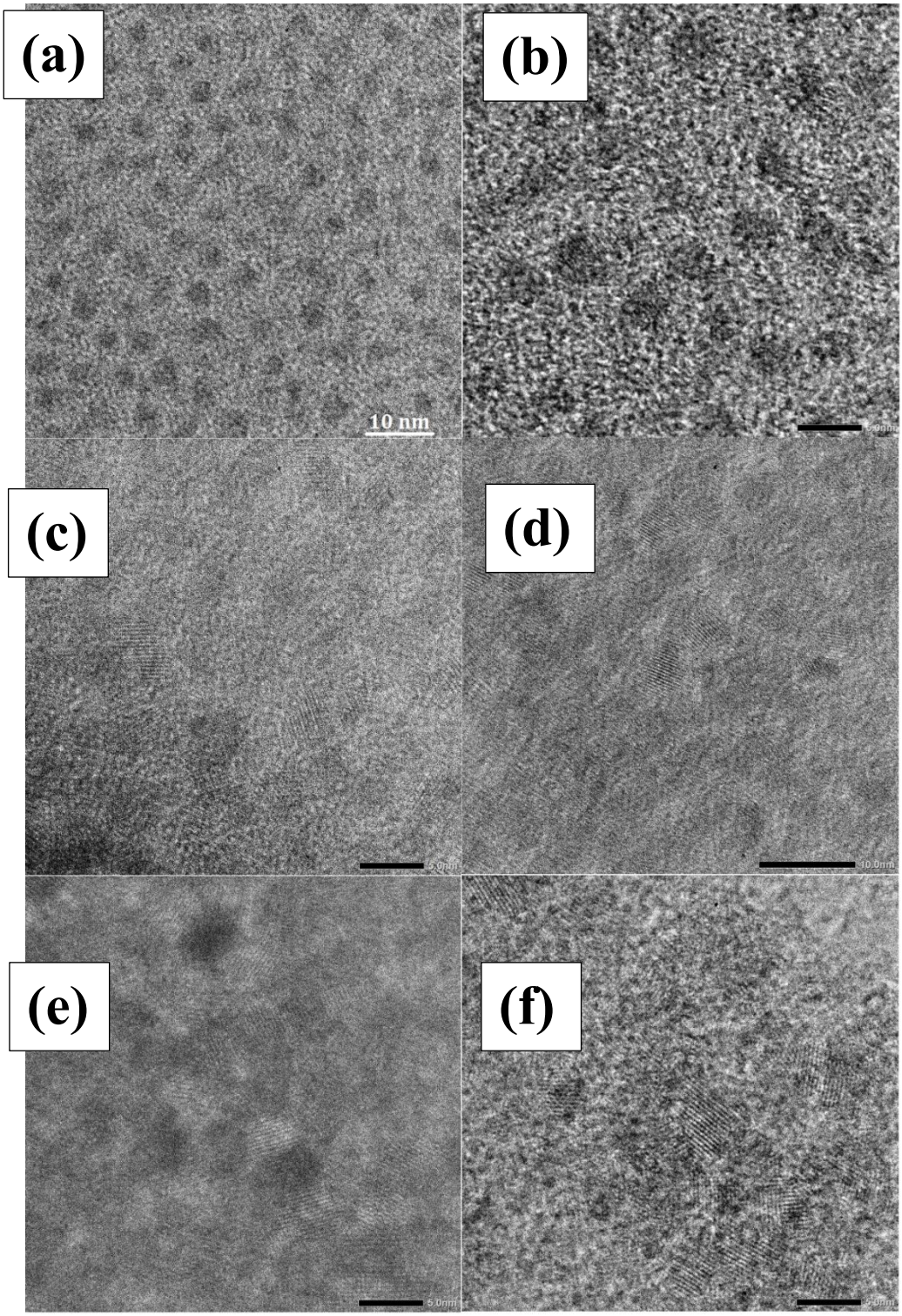

Figure 3-5. TEM images of PbSe QDs capped with different ligands. (a) PbSe-OA, the scale bar represents 10 nm; (b) PbSe-OA, the scale bar represents 5 nm; (c) PbSe-MPA, the scale bar represents 5 nm; (d) PbSe-EDT, the scale bar represents 10 nm; (e) PbSe-CTAB, the scale bar represents 5 nm; (f) PbSe-TBAI, the scale bar represents 5

nm.

We examined the effect of air exposure on PbSe QDs thin films to investigate the stability of these thin films, which were stored in air and under dark condition after fabrication. It's obvious that after 100 days the first exciton absorption peak of PbSe-OA thin film was blue shifted together with slightly broad, as shown in Figure 3-4b. This observation may originate from the changes in the surfaces of PbSe QDs which were oxidized to be higher bandgap species, such as Pb-O, or PbOH, resulting in smaller effective size of PbSe QDs (Figure 3-6).[111, 113] It means that the surface atoms of PbSe QDs which uncapped by OA and $CdCl_2$ are oxidized when they are exposed in air for a long time, thus the surface of PbSe-OA QDs needs for further passivation taking account of QDs' stability. In contrary, as shown in Figure 3-4c and 3-4d, the first exciton peak of PbSe-EDT film shows no significant change while that of PbSe-MPA film shows blue-shift. This indicates that PbSe-EDT film is more stable than PbSe-MPA film. EDT molecule with two thiol groups may effectively take more OA away from the PbSe CQDs surface and passivate more Pb ions on the surface of PbSe QDs than MPA molecule with only one thiol group. This is also confirmed by XPS result (Figure 3-6), in which, small peaks belonged to $Pb(OH)_2$ are observed in Pb 4f region of PbSe-MPA film. Fortunately, there are no sizable peak shifts for PbSe-CTAB and PbSe-TBAI films after storing in air for 100 days, as shown in Figure 3-4e and Figure 3-4f. Therefore, after CTAB and TBAI treatments, the air stabilities of PbSe QDs films are significantly improved. In Figure 3-6d and Figure 3-6e, the peaks belonged to Pb oxide species were not found. And the peaks of Pb $4f_{7/2}$ (or Pb $4f_{5/2}$) for both PbSe-CTAB and PbSe-TBAI films can fit with two components: one peak of Pb $4f_{7/2}$ at 137.5 eV corresponds to the binding energy of Pb-Se and the other peak of Pb $4f_{7/2}$ corresponds to Pb-X bond (X is halogen). For PbSe-CTAB, the latter peak at 137.9 eV corresponds to Pb-Br bond, while for PbSe-TBAI, the latter peak at 137.8 eV corresponds to Pb-I bond. We suppose the treatment of CTAB and TBAI can form strong protective layer (Pb-Br and Pb-I) on PbSe QDs surface, which can resist the oxidation of PbSe QDs, thereby improving the stability of PbSe QDs at ambient atmosphere.

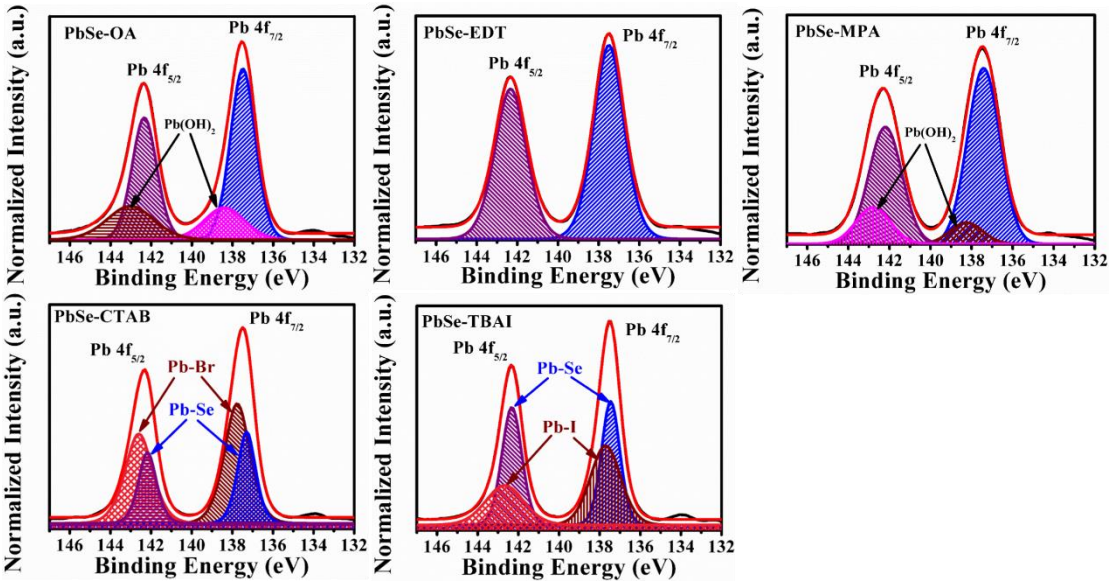

Figure 3-6. High-resolution XPS spectrum of Pb 4f region of (a) OA, (b) EDT, (c) MPA, (d) CTAB, (e) TBAI capped PbSe films, respectively.

3.3.3 Ligand Dependent Energy Levels of PbSe QDs

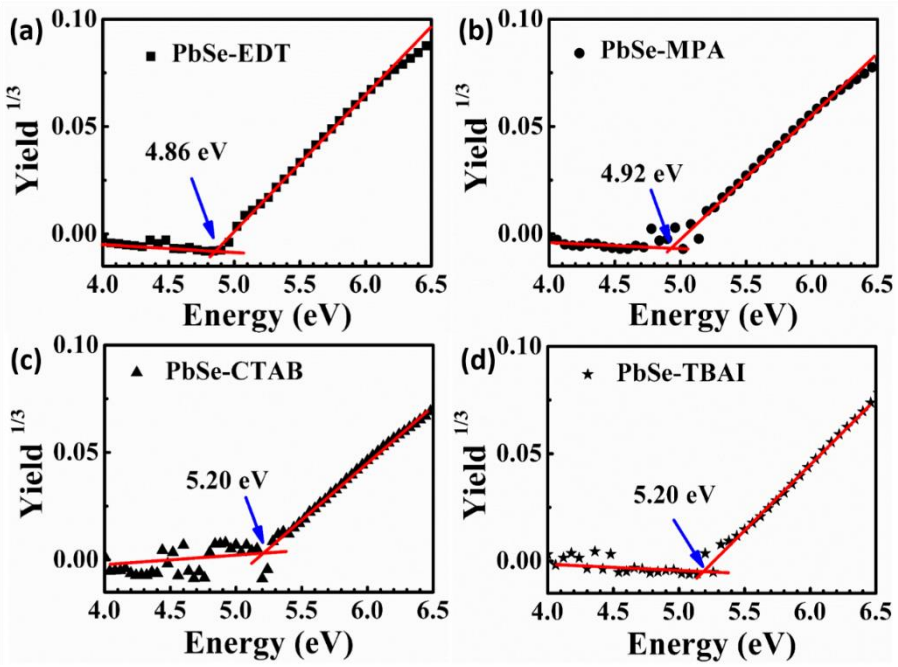

Figure 3-7. Photoelectron yield spectra of PbSe QDs films treated with EDT (a), MPA (b), CTAB (c), TBAI (d). The threshold energy for the photoelectron emission was estimated on the basis of the third root of the photoelectron yield plotted against the incident photon energy.

Changing the identity of the chemical binding group and dipole moment of the ligand should also affect the strength of the QD-ligand surface dipole and shift the vacuum energy, in turn change the valence band (VB) and conduction band (CB) position of QD.[123] The valence band maximum (VBM) positions of PbSe QDs thin films treated with different ligands were measured by using photoelectron yield spectroscopy (PYS, OA ligand is too insulating to be employed in PYS). Because of the collective contributions of the QD-ligand interface dipole and the intrinsic dipole moment of the ligand molecule itself,[123] the VBM positions of PbSe QDs treated with organic ligands EDT and MPA upward shift to -4.86 eV and -4.92 eV in comparison with halide ligands CTAB (-5.2 eV) and TBAI (-5.2 eV), respectively, as shown in Figure 3-7. The energy level diagrams of PbSe QDs treated with ligands were estimated from the PYS and UV-vis-measurements as shown in Figure 3-8. These energy level shifts will significantly influence the charge injection efficiency and open-circuit voltage of photovoltaic devices.

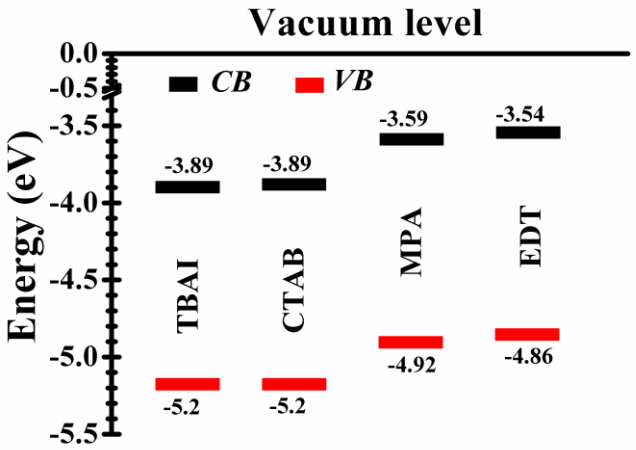

Figure 3-8. Schematic energy level diagrams of PbSe QDs treated with short ligands (the first exciton peak position of the film is taken as the band gap).

3.3.4 Ligand Dependent Exciton Dissociation in PbSe QDs film

Surface ligands treatment not only can influence the distance between QDs (Figure 3-5) and energy levels of QDs but also has effects on the QDs surface trap density and charge transfer between QDs.[124-125] In order to avoid formation of oxidation of

PbSe QDs, PL spectra of PbSe QDs thin films capped with different ligands were measured under vacuum at 77 K and 298 K with the excitation wavelength of 532 nm. It is known that the relaxation process of photoexcited carriers in QD solids usually includes radiative and non-radiative recombination.[126] The PL corresponds to the radiative recombination of excitons in the QDs. The PL quenching of QD solids is highly associated with non-radiative recombination. The non-radiative recombination of charge carriers in QDs solids are usually through four routes: carrier trapping by defects in QDs, charge transfer between QDs (i.e., the exciton dissociation), charge transfer from QDs to ligands which usually occurs when the ligand has conjugated structure, and energy transfer between QDs which usually occurs when the QDs have wide size distribution. In our work, all of the short ligands do not have conjugated group and PbSe QDs have a narrow size distribution. Thus, the PL quenching is considered to mainly depend on the trap density of PbSe QDs and the charge transfer between PbSe QDs.

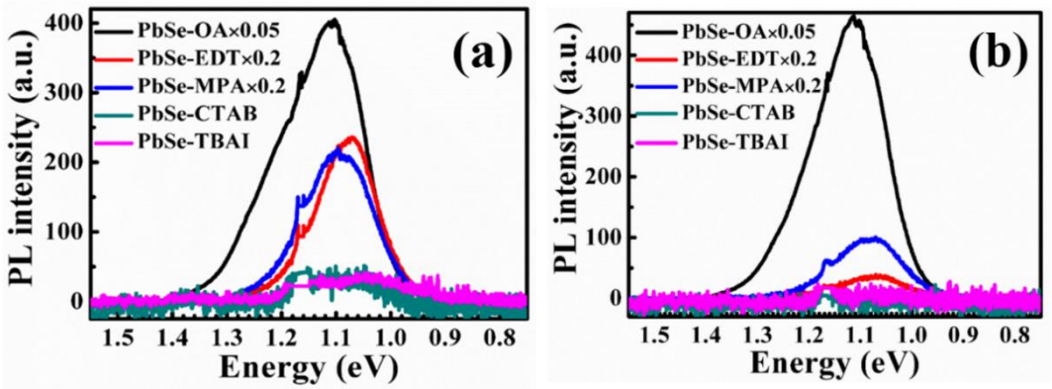

Figure 3-9. Steady state PL spectra measured at 77 K (a) and 298 K (b) for PbSe QDs films treated with ligands (the PL intensity of PbSe-OA, PbSe-EDT and PbSe-MPA films are shrunk 20 times, 5 times and 5 times than their original values, respectively).

As shown in Figure 3-9, the PL emission peak of PbSe-OA is at 1.11 eV. For the short ligands treated PbSe QDs films, the emission peaks are red shifted to 1.09 eV, 1.07 eV, 1.06 eV and 1.05 eV, respectively, the trends are consistent with the absorption spectra of the films. And the PL intensity decreased with the ligand length becoming shorter. Photoexcited carriers in PbSe-OA QDs with longest dielectric OA ligands between QDs are difficult to transfer to the adjacent QDs, which leads to the largest

PL emission. For short organic ligands EDT and MPA capped PbSe QDs, the PbSe inter-QD coupling is enhanced than that of PbSe-OA, so some photogenerated carriers can transfer to the adjacent QDs, some are trapped by surface or deep defects (we have observed surface oxidation by XPS for MPA treated PbSe QDs as mentioned earlier) and others are recombined through radiative recombination way. What's more, larger PL quenching is found in the CTAB and TBAI treated PbSe QDs solid films (high packing density) compared with PbSe-EDT and PbSe-MPA films. This phenomenon can also be observed at 298k (Figure 3-9b). As we discussed above, the short ligands can reduce the surface trap density of PbSe QDs, in turn improve the stability of PbSe QDs, especially for PbSe-CTAB and PbSe-TBAI. Therefore, the PL quenching of PbSe-CTAB and PbSe-TBAI films mainly depends on the charge transfer among PbSe QDs (the exciton dissociation). Thus, we can believe that the charge transfer from QD to QD (the exciton dissociation in QDs) in CTAB and TBAI treated PbSe QDs solid are faster and more unobstructed than those PbSe QDs solid treated with organic ligands. Next, we demonstrate this consideration by measuring the charge transfer rate from QD to QD (i.e., exciton dissociation rate) for different ligands treated PbSe QDs films using ultra-fast TA spectra measurement.

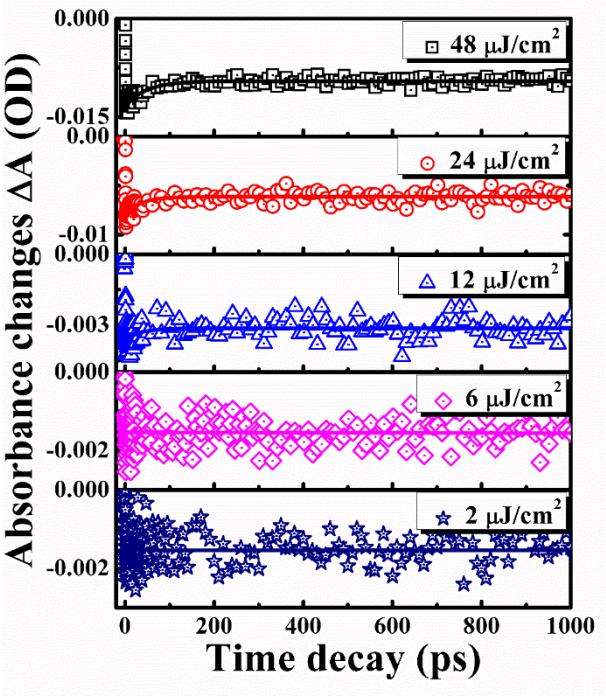

Figure 3-10. Power dependent TA spectra of the PbSe-OA solid QD films. The solid

lines are fitting curves. When 48 μJ/cm^2 pump fluence was applied, it can obviously find that the TA spectra contain two processes. The fast decay process which belongs to Auger recombination dominates the TA decay. When the pump fluence reduced to 6 μJ/cm^2, the signal of Auger recombination disappeared and the TA spectra can be well fitted by one exponential decay.

In all of the TA measurements, the pump light wavelength was 500 nm and the probe light wavelength was 935 nm (the peak position of the optical absorption spectra of the PbSe QD films as shown in Figure 3-4). Thus, the TA signal corresponded to the bleaching between LUMO and HOMO in the QDs. Then the TA signal intensity is proportional to the photoexcited exciton density in QDs.[127] Taking into the consideration of two-carrier and three-carrier recombination processes in the QDs, TA decay curves can be represented by the following equation:[128]

$$dn/dt = An + Bn^2 + Cn^3 \qquad (3-2)$$

where the first term A_n represents single-carrier behaviour, the second term Bn^2 represents two-carrier (electron-hole) radiative recombination (i.e. PL emission), and the third term Cn^3 represents the three-carrier Auger recombination process. In order to particularly evaluate the charge transfer process, i.e., the exciton dissociation (which is a single-carrier behaviour) in PbSe QD films, two-carrier and three-carrier recombination processes are needed to avoid which tend to take place under strong pump fluence, as shown in Figure 3-10. Therefore, a weak enough pump fluence of 6 μJ/cm^2 was applied here, under which condition the normalized TA decay can be fitted very well with one exponential decay, i.e., the first term of equation (3-2).

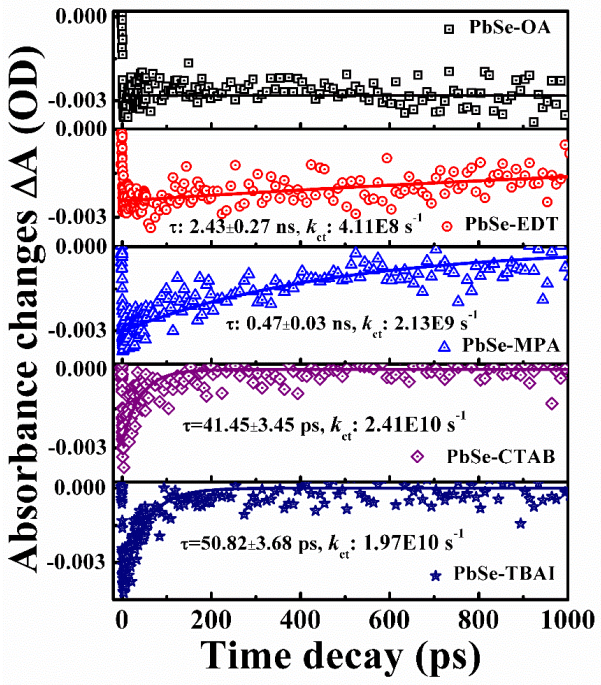

Figure 3-11. Comparison of the TA decays of PbSe QD films with different ligands. All samples were pumped by 500 nm laser pulse with the pump fluence of 6 μJ/cm^2, and probed at 935 nm. The solid lines are fitting curves with one exponential equation.

In Figure 3-11, for PbSe-OA film where QDs are separated by OA ligands, the TA signal is almost constant and no decay can be observed on the time scale of 1 ns. This result indicates that charge transfer between the QDs does not occur when the QD-QD distance is large enough (about 3 nm here, which can be confirmed in Figure 3-5a and Figure 3-5b). For short ligands treated PbSe films, the TA spectra can be well fitted by one exponential decay with a decay time τ. As shown in Figure 3-11, the values of τ in PbSe-EDT, PbSe-MPA, PbSe-CTAB and PbSe-TBAI are about 2.43 ns, 0.47 ns, 41.45 ps and 50.82 ps, respectively. The corresponding charge transfer rates $k_{ct}=1/\tau$ (i.e., the exciton dissociation rate in PbSe QDs) of PbSe-EDT, PbSe-MPA, PbSe-CTAB and PbSe-TBAI are 4.11 x 10^8 s^{-1}, 2.13 x 10^9 s^{-1}, 2.41 x 10^{10} s^{-1}, 1.97 x 10^{10} s^{-1}, respectively. It means that k_{ct} in PbSe-CTAB and PbSe-TBAI solid QD films are 1-2 orders of magnitude larger than that in PbSe-EDT and PbSe-MPA, which is consistent with the PL quenching results. According to above experimental results, it can be concluded that the halide ligands capped PbSe QDs have faster exciton dissociation rate than those of short organic ligands capped. The reason can be considered as follows. The

exciton dissociation (charge transfer from QD to QD) in the ligand treated PbSe QDs films occurs through electronic tunnelling effect.[129-130] So the charge transfers rate k_{ct} exponentially decreased with the QD-QD distance. Thus, k_{ct} increased largely for the halide ligands capped PbSe QDs film because of the smallest QD-QD distance of about 0.5 nm.

3.3.5 Ligand Dependent Photovoltaic Performance of PbSe CQDSCs

As is well known, the above discussion of exciton dissociation and charge transport in QDs active layer are of great value for deeply understanding the performance of photovoltaic devices. Figure 3-12 shows the light and dark current density-voltage (*J-V*) curves of PbSe CQDSCs. It is found that devices using EDT and MPA as surface ligands exhibit higher open-circuit voltage (V_{oc}) than those using CTAB and TBAI as ligands. The reason is not very clear now. One possibility is considered as follows. It was reported that EDT and MPA treated PbSe and PbS QDs exhibited *p*-type behaviour and Br^- and I^- treated PbSe and PbS QDs with near n-type characteristics,[108, 115, 119, 122, 130-133] so the difference between the Fermi energy level (E_F) and VBM in PbSe-EDT and PbSe-MPA are smaller than those in PbSe-CTAB and PbSe-TBAI. Despite the energy levels of PbSe-EDT and PbSe-MPA are higher than PbSe-CTAB and PbSe-TBAI (as shown in Figure 3-8), the E_F of PbSe-EDT and PbSe-MPA QDs may be lower than those of PbSe-CTAB and PbSe-TBAI.[114] So the E_F differences of TiO_2 and PbSe-organic ligand are larger than that of TiO_2 and PbSe-halide ligand, which results in higher V_{oc} of PbSe-EDT and PbSe-MPA CQDSCs.

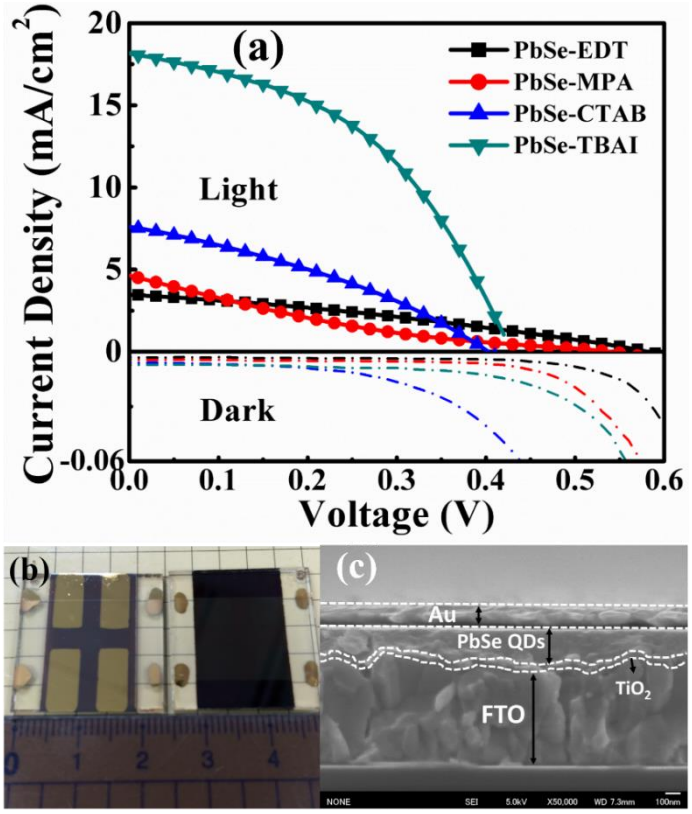

Figure 3-12. (a) *J-V* curves of PbSe CQDSCs using different ligands (measured in air), (b) photograph and (c) SEM cross-section image of PbSe planar heterojunction CQDSCs.

In contrary, the short-circuit current density (J_{sc}) of both of EDT and MPA treated devices are lower than that of devices treated with halide ligands. As we discussed above, the exciton dissociation rate, i.e., the charge transfer rate in the EDT and MPA treated QD films are 1-2 orders smaller compared to those in halide ligand treated the QD films. Larger PL intensity was observed for the former QD films. Therefore, one reason for the lower J_{sc} of PbSe-EDT and PbSe-MPA devices could be attributed to the relatively smaller exciton dissociation rate (charge transfer rate). It is worth noting that CTAB and TBAI exhibit huge distinct influence on the performance of PbSe CQDSCs. The *PCE* of PbSe-TBAI devices (3.50%) shows about 3.5 times value of PbSe-CTAB device (1.04%), which is mainly ascribed to the high J_{sc} and *FF* in PbSe-TBAI device. We have known that the bonding energy between Pb^{2+} and I^- is stronger than that between Pb^{2+} and Br^-, which leads to less surface trap density on PbSe-TBAI QDs.[108, 134] Surface traps can capture the photoexciton carries and as the electron-

hole recombination centres, which play a destructive impact on the charge collection efficiency and thus J_{sc} of CQDSCs. As we discussed earlier, the exciton dissociation rates are almost the same for PbSe-CTAB and PbSe-TBAI QDs films. Thus, the difference in the J_{sc} and *FF* in the two kinds of CQDSCs would be resulted from the difference in charge recombination and the charge collection efficiency. Moreover, Zhang et al investigated the hot carrier dynamics in PbSe-I and PbSe-Br QD films, they found that PbSe-I showed longer hot carrier thermalization time than PbSe-Br.[134] So the relatively slow hot carrier cooling in PbSe-TBAI film has a possibility for some hot carrier injection which may result in an increase in the J_{sc} of device.

Table 3-2. Performance details of PbSe CQDSCs using different ligand [a]

Devices	J_{sc} (mA/cm^2)	V_{oc} (V)	*FF* (%)	*PCE* (%)
PbSe-EDT fresh	3.48±0.22 (3.70)	0.58±0.01 (0.59)	31.6±0.4 (32.0)	0.64±0.05 (0.69)
PbSe-EDT 3 days	3.02±0.09 (3.09)	0.57±0.01 (0.58)	29.3±0.5 (29.7)	0.51±0.02 (0.53)
PbSe-MPA fresh	4.64±1.95 (6.59)	0.53±0.01 (0.54)	16.4±0.2 (16.6)	0.41±0.18 (0.59)
PbSe-MPA 3 days	2.46±0.75 (3.20)	0.52±0.01 (0.52)	15.9±0.4 (16.2)	0.20±0.07 (0.27)
PbSe-CTAB fresh	7.61±0.55 (7.06)	0.40±0.01 (0.40)	33.8±4.6 (38.4)	1.04±0.05 (1.09)
PbSe-CTAB 3 days	7.20±0.11 (7.25)	0.38±0.01 (0.38)	24.2±4.1 (28.9)	0.66±0.14 (0.80)
PbSe-TBAI fresh	18.1±0.1 (18.1)	0.42±0.01 (0.43)	44.6±0.8 (45.4)	3.50±0.03 (3.53)
PbSe-TBAI 3 days	18.3±0.1 (18.3)	0.42±0.01 (0.42)	44.9±0.5 (45.4)	3.49±0.03 (3.52)

[a] Numbers in parentheses represent the values obtained for the best-performing cell. To account for experimental errors, four devices of each type were measured to give the reported averages and deviations. All of the devices were stored and measured in air.

In order to reveal the effects of different ligands on charge carrier recombination and charge carrier lifetime in PbSe CQDSCs, transient open-circuit photovoltage decay measurements were carried out. Figure 3-13a shows the transient photovoltage

decay curves of PbSe CQDSCs with different ligands. It evidences that the PbSe-TBAI device exhibits much slower decay processes than those devices treated with other ligands. To quantitatively analyse the photovoltage decay processes, the decay curves can be fitted by using a dual exponential decay according to the following equation:

$$y(t) = A_1 e^{-t/\tau_1} + A_2 e^{-t/\tau_2} \qquad (3-3)$$

where A_1 and A_2 are proportionality constants, τ_1 and τ_2 are time constants.[117] The fitted curves are shown in Figure 3-13a (solid lines) and the corresponding parameters are shown in Table 3-3. According to the fitting data, the voltages of the PbSe-EDT and PbSe-MPA devices decrease quickly than those of PbSe-CTAB and PbSe-TBAI. What's more, the weight of fast voltage decay process (A_1) in PbSe-EDT and PbSe-MPA devices takes up a large proportion about 59.5% and 76.3%, respectively. The faster voltage decay of PbSe-EDT and PbSe-MPA devices is mainly ascribed to their larger defect density.

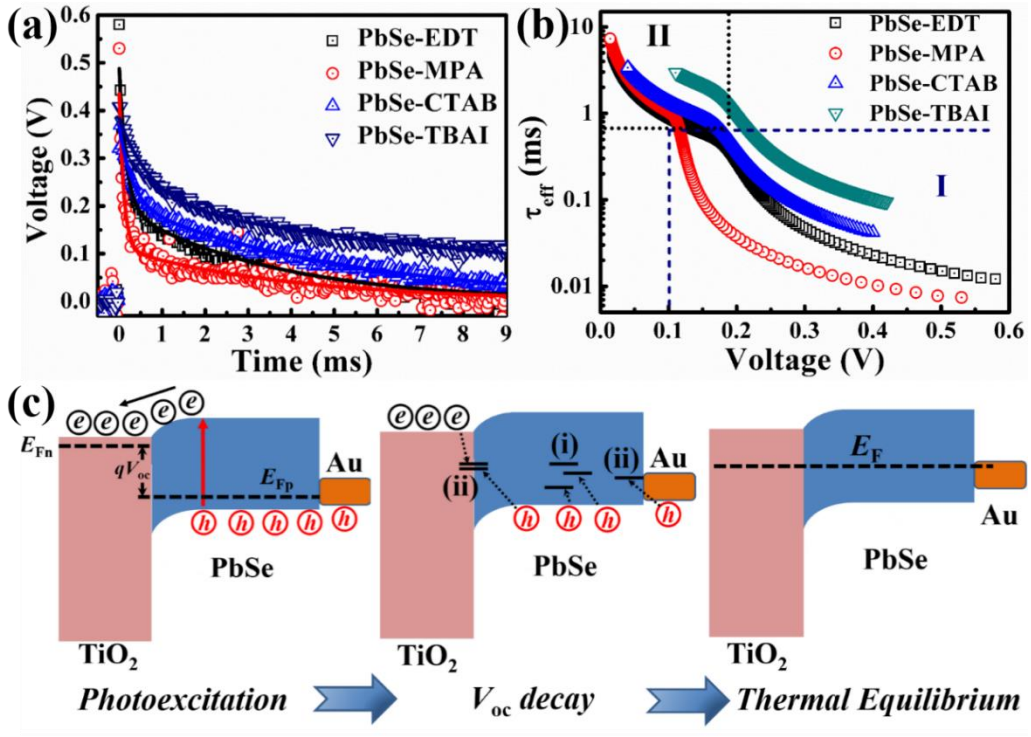

Figure 3-13. (a) The open-circuit photovoltage decay curves for PbSe CQDSCs with

different ligands. (b) The effective carrier lifetime calculated from the voltage decay curves. (c) Schematic illustration of the energy level alignment in the PbSe CQDSCs under different conditions. The voltage decay process is mainly through two recombination paths: (i) intrinsic trapping-assisted recombination in the PbSe QDs layer, and (ii) interfacial recombination at the TiO_2/PbSe interfaces and PbSe/Au interfaces.

Table 3-3. Fitted proportionality constants and time constants obtained from the open-circuit photovoltage decay curves of the PbSe CQDSCs.

Devices	A_1 (A_1/(A_1+ A_2))	τ_1 (ms)	A_2 (A_2/(A_1+ A_2))	τ_2 (ms)
PbSe-EDT	0.290±0.007 (59.5%)	0.16±0.01	0.197±0.003 (40.5%)	3.51±0.05
PbSe-MPA	0.355±0.009 (76.3%)	0.11±0.01	0.110±0.002 (23.7%)	4.01±0.12
PbSe-CTAB	0.161±0.002 (43.9%)	0.30±0.01	0.206±0.001 (56.1%)	5.22±0.04
PbSe-TBAI	0.178±0.002 (46.4%)	0.75±0.02	0.206±0.002 (53.6%)	12.59±0.22

To make sense of charge carrier recombination processes in CQDSCs, we evaluated the recombination process based on the effective carrier lifetime (τ_{eff}), which can be defined by the following equations: [117, 135]

$$\tau_{eff} = -(\frac{kT}{q})/(\frac{dV_{oc}}{dt}) = \frac{1}{\tau_n^{-1} + \tau_p^{-1}} \qquad (3-4)$$

$$\tau_n^{-1} = \frac{1}{n} \cdot \frac{dn}{dt} \qquad (3-5)$$

$$\tau_p^{-1} = \frac{1}{p} \cdot \frac{dp}{dt} \qquad (3-6)$$

where k is the Boltzmann constant, T is the temperature, q is the elementary charge, n is the free electron density in the TiO_2 film and p is the free hole density in the PbSe

QDs. τ_n and τ_p are the free electron lifetime in the TiO_2 and the free hole lifetime in the PbSe QDs layer, respectively. According to the above equations, the open-circuit photovoltage decay is dependent on both the electron and hole lifetimes in PbSe CQDSCs.

The τ_{eff} was calculated from the voltage decay curves (Figure 3-13a) which is shown in Figure 3-13b. The observed trend in τ_{eff} was TBAI > CTAB > EDT > MPA, which was consistent with the photovoltaic performances. The value of τ_{eff} in the PbSe-TBAI device is 1 or 2 orders of magnitude higher than those of other three devices, which confirms that the carrier lifetime in PbSe-TBAI device is longer than those of others. This corresponds to higher J_{sc} of PbSe-TBAI device due to larger charge collection efficiency. More interestingly, the photovoltage-dependent effective carrier lifetime curves can be separated into two sections, I and II, which correspond to two different recombination processes. It can obviously find that the voltage of devices mainly is influenced by the smaller τ_{eff} carriers in the solar cells. In the smaller τ_{eff} region (less than 0.7 ms, section I in Figure 3-13b), the values of τ_{eff} in different ligands treated PbSe CQDSCs exhibit a large difference when they get the same voltage. This confirms that the voltage decay process is dominated by the hole trapping mechanism in PbSe QDs layer (Figure 3-13c). The larger τ_{eff} region II (over 1 ms) is belonged to slow voltage decay process, in which the values of τ_{eff} in PbSe-EDT, PbSe-MPA and PbSe-CTAB devices are nearly the same (except PbSe-TBAI). This means that the slower recombination region II mostly due to electron recombination in TiO_2 and/or TiO_2/PbSe interfaces, and the ligands treatments have no obvious effect on this recombination process. More details about the effect of TBAI on the interfacial recombination will be investigated in future work. Based on the above results, it can conclude that the trap or defects state in PbSe layer have great impact on the V_{oc} of CQDSCs, and QDs surface treatment with TBAI can significantly reduce the surface states and enhance the charge collection efficiency in PbSe QDs layer, thus enhancing the J_{sc}, V_{oc} and *PCE* of PbSe CQDSCs.

3.3.6 The Stability of PbSe CQDSCs

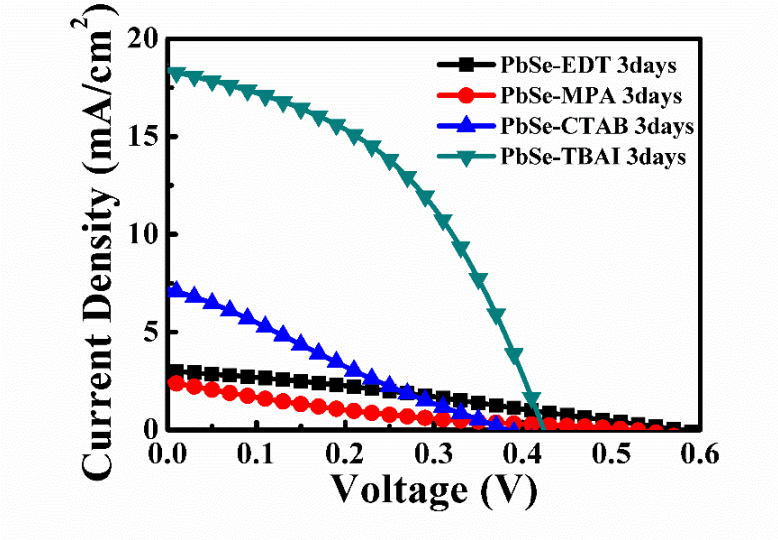

Figure 3-14. *J-V* curves of PbSe CQDSCs using different ligands after storing in air for 3 days.

Besides efficiency, the stability is also a significant indicator for the overall evaluation of solar cells. As shown in Table 3-2 and Figure 3-14, PbSe-TBAI device is the most stable one after 3 days while PbSe-EDT, PbSe-MPA and PbSe-CTAB devices show more or less reduction. The PCE degradation of those devices is possibly due to there are more defects in those devices than PbSe-TBAI device.

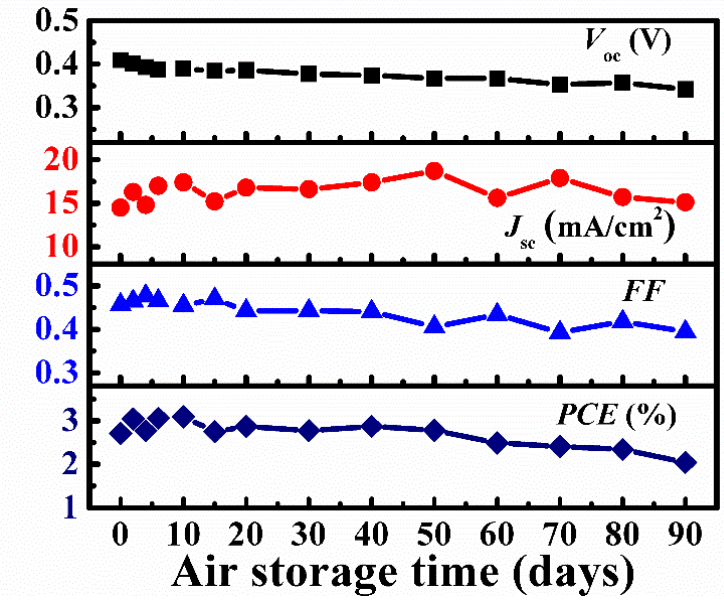

Figure 3-15. Stability evaluation of PbSe-TBAI CQDSCs. The solar cells were stored

and tested in an ambient atmosphere.

Furthermore, we have evaluated the long-term stability of the PbSe-TBAI device. All the solar cells were kept and tested in air without the control of humidity. In Figure 3-15, PbSe-TBAI CQDSCs exhibited the excellent stability for over 10 days and the efficiency still reaches over 75% of original after 90 days (>2000 h). What's more, we also investigated the continuous illumination stability of PbSe-TBAI CQDSCs in air, as shown in Figure 3-16. Unfortunately, the V_{oc} and *FF* of solar cell were gradually reduced along with the increase of illumination time, and the PCE of solar cell only keeps about 70% of the original after continuous illumination 3.5 hours (under 100 mW/cm^2, AM 1.5 G illumination). This result indicates that light irradiation in air may accelerate the degradation of the PbSe CQDSCs.

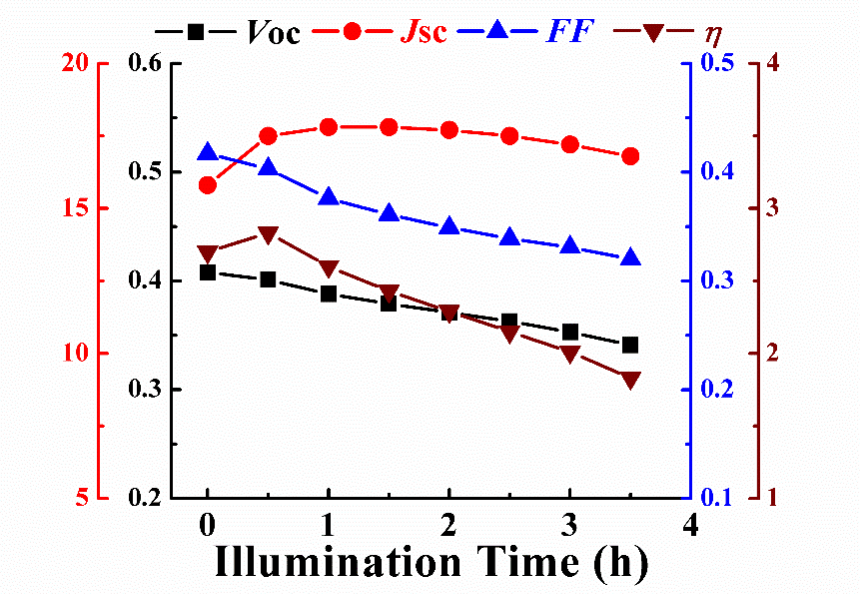

Figure 3-16. *J-V* curves of PbSe-TBAI CQDSCs which measured under continuous illumination for 3.5 hours (in air).

3.4 Conclusions

In summary, long term air-stable and high efficiency PbSe CQDSCs were obtained by using TBAI as ligand in solid state ligand-exchange process, and it is realized that the whole processes: from PbSe QDs washing step to PbSe CQDSCs fabrication, storage and measurements are all in ambient atmosphere for the first time. In addition,

ligand-dependent performance of PbSe QD films and CQDSCs were systematically investigated in this work. By monitoring the absorption, PL and TA spectra of the samples, we confirmed that TBAI treatment can produce more air-stable and higher charge transfer rate PbSe QD films than mercapto organic short ligands (EDT and MPA). Due to less surface trap density and higher charge transfer rate in the solar cells, the PCE of TBAI treated large size PbSe CQDSCs is obtained as high as 3.53%. The mechanism behind this achievement was explored using open-circuit voltage decay. It was informed that the TBAI treatment significantly reduced the intrinsic hole trapping-assisted recombination in PbSe layer and improved the effective carrier lifetime in the PbSe CQDSCs. The device stability was also evaluated, which showed excellent storage stability in air (the efficiency of CQDSCs still remained 77% of original value over 90 days). In a word, long term stability and high efficiency PbSe CQDSCs can be fabricated and tested in ambient atmosphere by using TBAI as ligands. This work would shed light on the investigation of other PbSe QDs based devices, such as FET.

The originalities of this work are: (1) TBAI was used to exchange original surface ligand OA of PbSe QDs for the first time; (2) long-term air stable PbSe based QDSCs was obtained.

Chapter 4: Improvement of Photovoltaic Performance of Colloidal Quantum Dot Solar Cells Using Organic Small Molecule as Hole-Selective Layer

4.1 Introduction

In order to effectively enhance the photovoltaic performance, various interfacial modifications in CQDSCs are vital issues.[136-137] Considering the QDs layer in the first place, the surface defect states of QDs are the major constraints upon solar cell performance. Introducing the halide ligand, such as tetrabutylammonium iodide (TBAI) or PbI_2 to modify the surface of QDs is an effective way to enhance the coupling effect between QDs and reduce surface defect states of QDs.[40, 44, 108, 123, 138-141] Second, the use of appropriate charge selective contacts for both electrons and holes is a major issue in this kind of devices. For the photoanode/QDs interface, introducing an electron selecting layer between photoanode (ZnO or TiO_2, which have been the most commonly used) and the QDs active layer, and doping photoanode have been found to significantly reduce the trap density of photoanode and reduce the interfacial charge recombination at this interface.[117, 142-147] For QDs/Au interface, the notion of inserting a hole-selective layer (HSL) between them has been proposed to suppress the interfacial charge recombination at this interface.[41, 148-152] Molybdenum trioxide (MoO_3) has been introduced into PbS CQDSCs but those solar cells showed unstable properties due to the sensitivity of MoO_3 to H_2O and O_2.[148, 150, 153] An improved ZnO/PbS-TBAI/PbS-EDT (1,2-ethanedithiol) *p*-*i*-*n* solar cell architecture has promoted the PCE of CQDSCs from 7.0% to 9.2%.[41] Unfortunately, the EDT ligand is easily desorbed from QDs surface when the device was exposed to humid air in short time, reducing the stability and PCE of CQDSCs.[122, 140, 154] Other hole transport materials such as poly(3-hexylthiophene-2,5-diyl) (P3HT), 2,2',7,7'-tetrakis(*N*,*N*-di-*p*-methoxyphenylamine)-9,9'-spirobifluorene (Spiro-OMeTAD) and poly(bis(4-phenyl)(2,4,6-

trimethylphenyl)amine) (PTAA) have also been introduced into CQDSCs as a hole-selective/electron-blocking layer between QDs layer/Au electrode interface.[151, 155-157] However, high synthesis cost, complex purification, and the replicability especially for polymers are the major constraints upon their wide application. Great challenge should be taken to develop novel HSL with low cost and superior device stability.

Herein, we cooperated with Prof. Otsuki and Dr. Wu of Nihon University and develop a novel donor-π-donor (D-π-D) organic small molecule bis-triphenylamine with spiro(fluorene-9,9'-xanthene) as the conjugated system, named BTPA-4, as a HSL in the PbS CQDSCs. We found that the introduction of BTPA-4 as HSL can enhance the open-circuit voltage (V_{oc}), prolong the effective carrier lifetime (τ_{eff}), reduce the recombination at PbS-QDs/Au interface, and hence improve the device performance. Furthermore, the PbS CQDSCs with BTPA-4 possessed a remarkable long-term stability for more than 100 days of storage in ambient atmosphere that has been the Achilles' heel of other organic HSL for CQDSCs.

4.2 Experimental Methods

Materials. Lead(II) oxide (PbO, Wako, 99.5%), oleic acid (OA, Aldrich, 90%), 1-octadecene (ODE, Aldrich, 90%), hexamethyldisilathiane (TMS, Aldrich, synthesis grade), cadmium chloride ($CdCl_2$, Wako, 95%), tetradecylphosphonic acid (TDPA, Aldrich, 97%), oleylamine (OLA, Aldrich, 70%), Zinc acetate dehydrate ($Zn(OAc)_2 \cdot 2H_2O$, Wako, 99.9%), ethanolamine (Wako, 99.0%), 2-methoxyethanol (Wako, 99.0%), zinc nitrate hexahydrate ($Zn(NO_3)_2 \cdot 6H_2O$, Wako, 99.0%), hexamethylenetetramine (HMTA, Wako, 99.0%), 1,2-ethanedithiol (EDT, Aldrich, 98%), cetyltrimethylammonium bromide (CTAB, Wako, 98%). These materials were used as received from commercial sources without any purification.

Synthesis of PbS-QDs. The synthesis of colloidal PbS-QDs is carried out similarly to our previously reported method.[117] Briefly, 6 mmol PbO, 15 mmol oleic acid and 50 mL 1-octadecene (ODE) was degassed at 80°C for 1 h. The obtained solution was heated to 85°C under nitrogen for another 2 h, followed by the injection of a hexamethyldisilathiane (TMS) solution (3 mmol TMS in10 mL of pre-degassed ODE).

When the obtained colloid solution was cooled to 70°C, a $CdCl_2$-TDPA-oleylamine halide precursor was injected into the colloidal PbS solution. After cooling down to room temperature, PbS-QDs were isolated by adding acetone and centrifugation. The supernatant was discarded and the precipitate was purified by successive dispersion in toluene and precipitation with a mixture of acetone and methanol. The obtained PbS-QDs precipitate was dried by an N_2 flow and finally dispersed in octane at a concentration of 50 mg/mL.

Synthesis of BTPA-4. A solution of *N*,*N*-bis(4-methoxyphenyl)-4-(4,4,5,5-tetramethyl-1,3,2-dioxaborolan-2-yl)benzenamine (354 mg, 0.82 mmol), spiro-9-(2,7-dibromofluorene)-9'-xanthene (200 mg, 0.41 mmol), $Pd(PPh_3)_4$ (40 mg, 0.04 mmol), and K_2CO_3 (2 M solution, 0.5 mL) in THF (15 mL) was stirred under nitrogen in the dark at 85°C for 48 h. After cooling to room temperature, the mixture was extracted with $CHCl_3$ by adding aqueous $NaHCO_3$ solution. Then the organic layer was dried over $MgSO_4$ and concentrated under reduced pressure to give the crude product. Finally, the crude product was purified by silica gel column chromatography eluted with hexane/ethyl acetate (5/1) to give a yellow solid BTPA-4 (weight: 210 mg, mole: 0.22 mmol, yield: 55%). ^{1}H NMR (400 MHz, $CDCl_3$): δ ppm: 7.82 (d, 2 H, J = 7.6 Hz), 7.59 (d, 2 H, J = 9.6 Hz), 7.37 (s, 2 H), 7.33 (d, 4 H, J = 8.8 Hz), 7.25 (t, 2 H, J = 6.8 Hz), 7.19 (t, 2 H, J = 7.6 Hz), 7.06 (m, 8 H), 6.93 (m, 4 H), 6.83 (d, 8 H, J = 9.2 Hz), 6.78 (d, 2 H, J = 8.0 Hz), 6.55 (d, 2 H, J = 7.6 Hz), 3.79 (s, 12 H). ^{13}C NMR (100 MHz, $CDCl_3$): δ ppm: 155.8, 155.7, 151.3, 148.0, 140.8, 140.7, 137.8, 132.7, 128.1, 128.0, 127.3, 126.4, 126.1, 125.0, 123.5, 123.3, 120.6, 120.0, 116.6, 114.6, 55.4, 54.3. APCI-HRMS *m/z* ($[M+H]^+$): calcd: 939.3798, Found: 939.4090. Anal. calcd for $C_{65}H_{50}N_2O_5 \cdot 0.2\ CHCl_3$: C, 81.32; N, 2.91; H, 5.25. Found: C, 81.18; N, 2.93; H, 5.17.

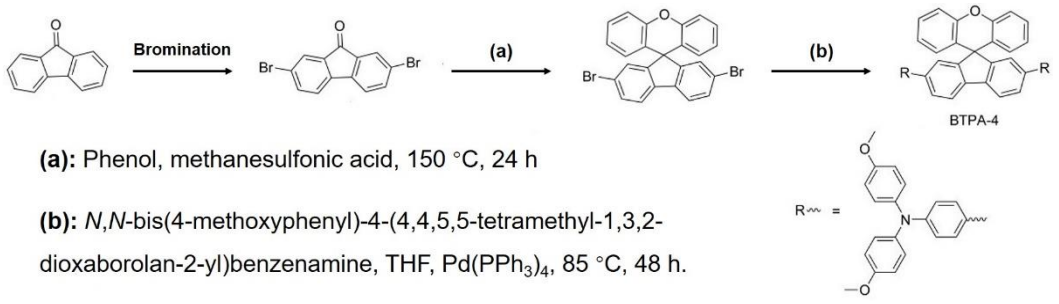

Scheme 4-1. Synthetic route of BTPA-4.

Fabrication of solar cells. PbS-QDs-based bulk heterojunction solar cells were constructed by combining ZnO-nanowires (ZnO-NWs) arrays with PbS-QDs, whose first absorption peak was 910 nm. The ZnO-NWs arrays with 1.5 μm thickness were formed on ZnO compact layer (ZnO-CL) by a hydrothermal method. To prepare the sol–gel precursor for the ZnO compact layer, zinc acetate dehydrate and ethanolamine were dissolved in 2-methoxyethanol to obtain the 0.5 M zinc precursor (solution-1). Then, 300 μL of solution-1 was dropped onto cleaned FTO glasses and spun-cast at 1000 rpm for 2 s plus 3500 rpm for 30 s, followed by baking at temperature 150°C for 5 min in air. These spin-coat and annealing processes were repeated to generate a uniform ZnO compact seed layer with a thickness of around 100 nm. To grow ZnO-NWs, the seed-coated FTO substrates were floated face down in Scott bottles containing the aqueous solution-2 (mixture of 25 mM zinc nitrate hexahydrate and 25 mM HMTA), and heated at 90°C for 4 h. Then, the substrates were rinsed with pure water, dried with a nitrogen flow, and annealed at temperature 350°C for 30 min.

PbS-QDs layers were deposited on ZnO-NWs arrays using a layer-by-layer method. For each layer, 120 μL of colloidal PbS-QDs was spin-cast onto the ZnO-NWs substrate at 2500 rpm for 15 s. Then, hexadecyltrimethylammonium bromide (CTAB) solution (30 mM in methanol) was dropped on the substrate and spun dry after a 1 min wait followed by rinsing three times with methanol. The PbS-EDT layers was covered on PbS-CTAB layer by 2.4 mM EDT (0.02% vol.) acetonitrile solution for 1 min before being spun at 2500 rpm for 15 s. The spinning substrate was washed by 400 μL of acetonitrile, followed by spinning for 20 s to dry the film. The above process was repeated to obtain two layers of PbS-EDT. The BTPA-4 layer was covered on the PbS-QDs layer by spin-casting the mixture of 10 mM BTPA-4, 57.6 μL 4-*tert*-butylpyridine (TBP), 35 μL bis (trifluoromethane) sulfonimide lithium salt (LiTFSI, 520 mg/mL in acetonitrile), and 1 mL chlorobenzene at 4000 rpm for 30 s. The Spiro-OMeTAD layer was covered on the PbS-QDs layer by spin-casting the mixture of 75 mg Spiro-OMeTAD, 28.8 μL TBP, 17.5 μL LiTFSI acetonitrile solution and 1 mL chlorobenzene at 4000 rpm for 30 s. Finally, 100 nm Au electrode was deposited onto the HSL by thermal evaporation through a shadow mask to create four identical cells on each substrate, each solar cell with an active area of 0.25 cm^2.

4.3 Results and Discussion

4.3.1 The Structure of PbS QD and BTPA-4

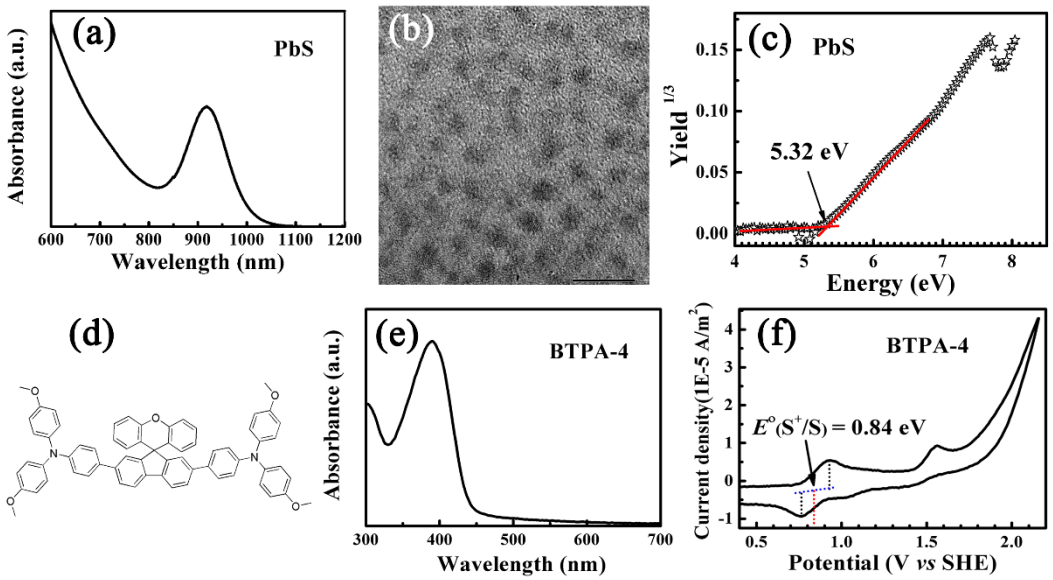

Figure 4-1. (a) Optical absorption spectrum of PbS-QDs in octane. (b) TEM image of PbS-QDs, the scale bar represents 10 nm. (c) Photoelectron yield spectrum of PbS-QDs film which was treated with hexadecyltrimethylammonium bromide (CTAB) (the threshold energy for the photoelectron emission was estimated on the basis of the third root of the photoelectron yield plotted against the incident photon energy). (d) Molecular structure of BTPA-4. (e) Optical absorption spectrum of BTPA-4 in dichloromethane (DCM). (f) Cyclic voltammogram in DCM, the potential values being obtained with ferrocene as the reference.

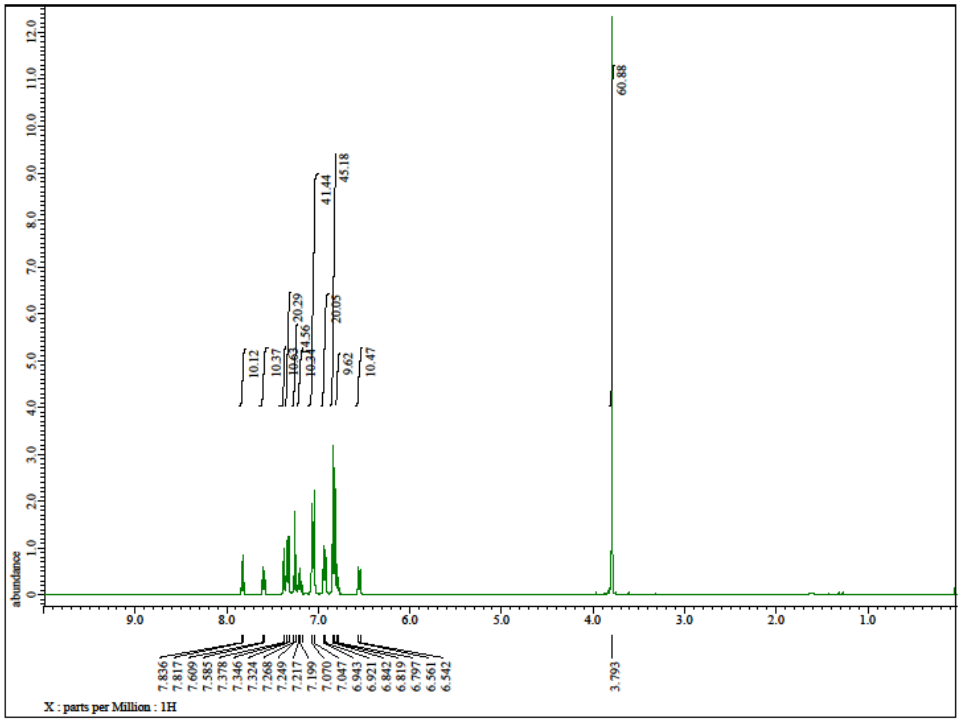

Figure 4-2. The ^{1}H NMR spectrum of BTPA-4 in $CDCl_3$.

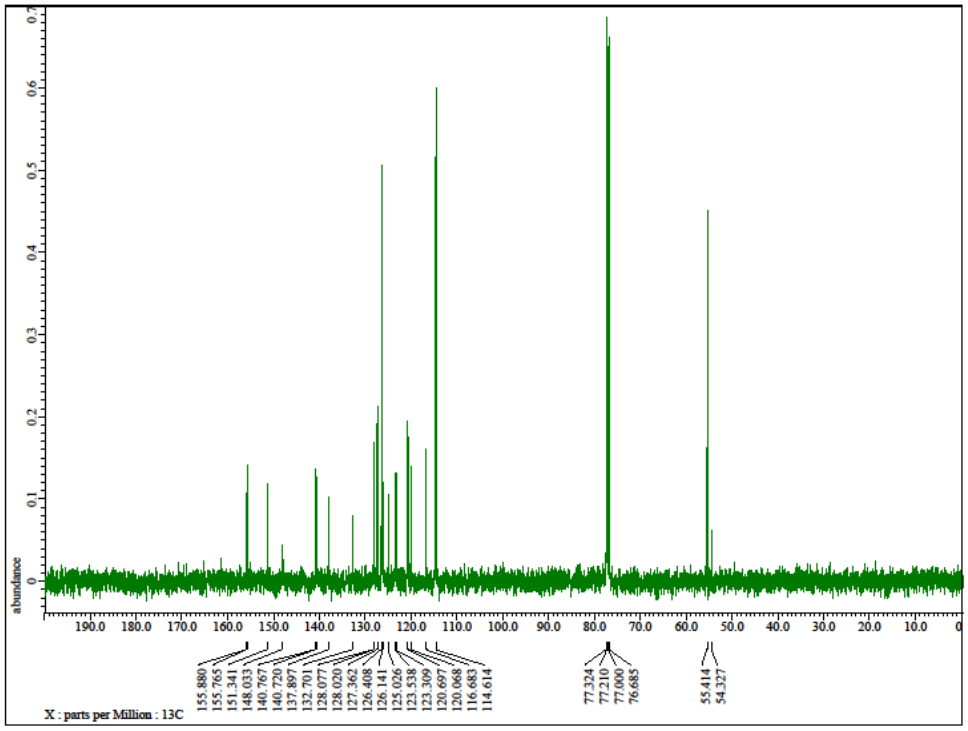

Figure 4-3. The ^{13}C NMR spectrum of BTPA-4 in $CDCl_3$.

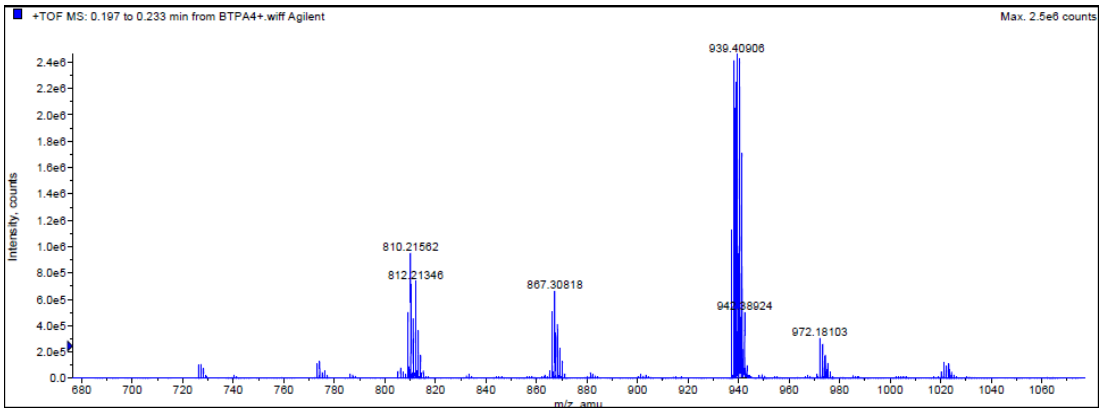

Figure 4-4. The APCI–HRMS of BTPA-4.

To clearly investigate the applicability of BTPA-4 in PbS CQDSCs, energy levels of PbS QDs and BTPA-4 were urgently needed. On one hand, PbS-QDs with oleic acid (OA) capping ligands were synthesized according to a previously reported method.[117] Figure 4-1a shows the optical absorption spectrum of the monodisperse PbS-QDs in octane. The first exciton absorption peak of PbS-QDs with the average size of PbS-QDs being approximately 2.7 nm in diameter, as shown in Figure 4-1b, is at 910 nm, which corresponds to its band gap energy of 1.36 eV. After solid state surface ligand exchange, the valence band maximum (VBM) position of the PbS-QDs film, which was treated by CTAB, was located at -5.32 eV as obtained by using photoelectron yield spectroscopy (Figure 4-1c). On the other hand, the molecular structure of BTPA-4 is depicted in Figure 4-1d, the ^{1}H NMR, ^{13}C NMR and HRMS spectra of BTPA-4 are shown in Figure 4-2, Figure 4-3 and Figure 4-4, respectively. The band gap (2.9 eV) of BTPA-4 can be calculated from the intersection of its absorption spectrum, which is shown in Figure 4-1e. The highest occupied molecular orbital (HOMO) energy level of BTPA-4 was determined from the following equation: E_{HOMO} = -4.5-$E°(S^{+}/S)$ (eV), where $E°(S^{+}/S)$ is the first oxidation potential value vs SHE (standard hydrogen electrode),[158] which was obtained from cyclic voltammetry, Figure 4-1f, as 0.84 V. Thus, the HOMO energy level of BTPA-4 can be calculated approximately as -5.3 eV.

4.3.2 The Performance of CQDSCs with BTPA-4 as Hole Selective Layer

The cross-section SEM image of the fabricated PbS CQDSCs is presented in Figure 4-5a, which confirms the *p-i-n* bulk heterojunction structure of the device as illustrated

in Figure 4-5b. It can be concluded that the thickness of the BTPA-4 layer is about 200 nm. Especially the BTPA-4 layer well contacts both with the PbS-QDs layer and the Au electrode. Figure 4-5c shows the diagram of energy level alignment in ZnO nanowires (NWs)/PbS-QDs/BTPA-4/Au solar cells, where the energy levels of PbS-QDs and BTPA-4 were estimated from the above discussion,[117, 159-160] while the energy levels of ZnO and Au were taken from literature.[117, 161] It is shown that the HOMO level energy of BTPA-4 matches well with that of PbS QDs, which can provide an energetically favorable path for the hole transport from PbS-QDs layer to Au electrode. In contrast, the lowest unoccupied molecular orbital (LUMO) energy of the BTPA-4 is higher than the LUMO level energy of PbS-QDs, which can set up a barrier for electron injection from PbS-QDs to Au electrode. It indicates that BTPA-4 has the potential as a hole-selective (or electron-blocking) layer to be used in the PbS CQDSCs.

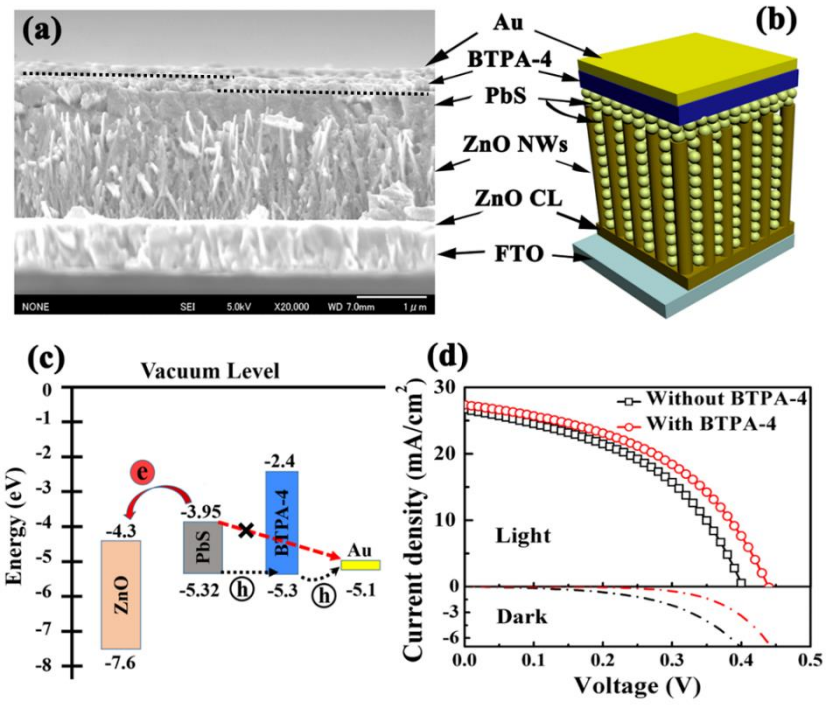

Figure 4-5. (a) Cross-section scanning electronic microscopy (SEM) image of the ZnO-NWs/PbS-QDs/BTPA-4/Au CQDSCs. (b) Schematic drawing of the *p-i-n* heterojunction PbS CQDSCs. (c) Energy level diagram of the ZnO, PbS-QDs, BTPA-4, and Au. (d) Comparison of the photocurrent density-voltage (*J-V*) curves of PbS CQDSCs with or without BTPA-4 as hole-selective layer.

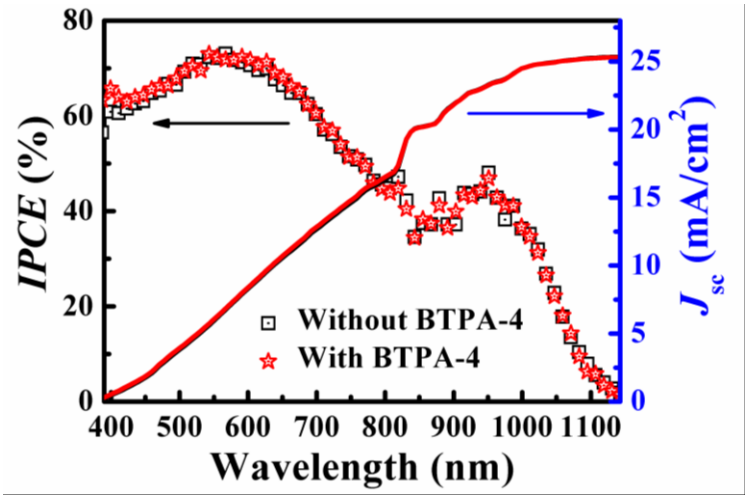

Figure 4-6. *IPCE* spectra and integrated J_{sc} of PbS CQDSCs with and without BTPA-4.

Figure 4-5d and Table 4-1 show the light and dark current density-voltage (*J-V*) curves and corresponding performance parameters of PbS CQDSCs with and without BTPA-4. The introduction of BTPA-4 layer strongly enhances the performance of PbS CQDSCs. The short-circuit photocurrent density (J_{sc}) of PbS CQDSCs shows no significant difference (the IPCE spectra of PbS CQDSCs with and without BTPA-4 are less difference), see Figure 4-6. The addition of the HSL does not produce an increase of the series resistance (R_s) of the device as it has been analyzed by impedance spectroscopy (*IS*) in following discussion. However, the best PbS CQDSCs with BTPA-4 HSL shows a PCE of 5.55%, which is around 15% higher than that without BTPA-4 layer (4.84%), mainly due to an enhancement of the open circuit voltage (V_{oc}).

Table 4-1. Performance details of PbS CQDSCs with and without BTPA-4 layer. Light intensity for the measurement is AM1.5 G 100 mW/cm^2 [a]

Devices	J_{sc} (mA/cm^2)	V_{oc} (V)	*FF* (%)	*PCE* (%)
Without BTPA-4	26.8±0.3 (26.6)	0.396±0.008 (0.402)	45.1±0.4 (45.3)	4.72±0.12 (4.84)
With BTPA-4	27.2±0.3 (27.0)	0.439±0.005 (0.442)	46.1±0.5 (46.5)	5.44±0.11 (5.55)

[a] Numbers in parentheses represent the values obtained for the best-performing cell. To account for experimental errors, eight devices of each type were measured to give

the reported averages and deviations. All of the devices were stored and measured in air.

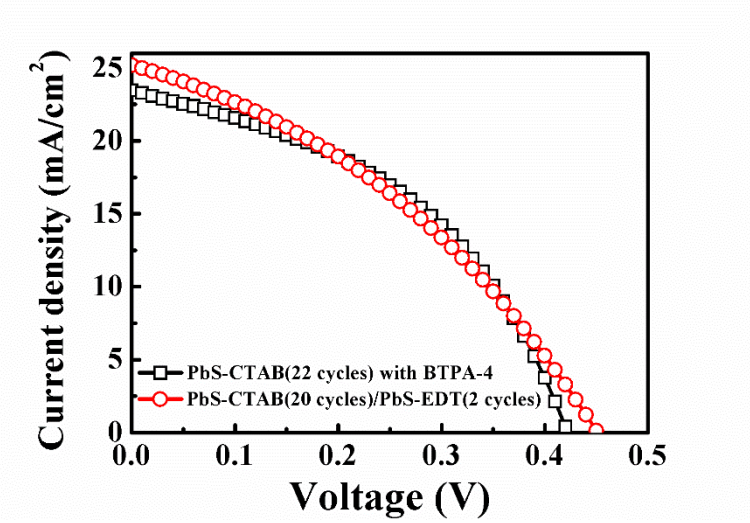

Figure 4-7. *J-V* curves of PbS CQDSCs using BTPA-4 and PbS-EDT as hole-selective layer.

Table 4-2. Performance details of PbS CQDSCs with BTPA-4 and PbS-EDT as hole-selective layer.

Devices	J_{sc} (mA/cm^2)	V_{oc} (V)	*FF* (%)	*PCE* (%)
With BTPA-4	23.5	0.422	43.6	4.32
With PbS-EDT	25.2	0.451	36.2	4.12

Although the V_{oc} and J_{sc} of PbS CQDSCs with BTPA-4 HSL are slightly lower than those of PbS CQDSCs with PbS-EDT, see in Figure 4-7 and Table 4-2, the fill factor (*FF*) of PbS CQDSCs with BTPA-4 is larger than that of device with PbS-EDT, resulting in a higher PCE. BTPA-4 can also work as HSL for different sizes PbS-QDs based CQDSCs (see Figure 4-8 and Table 4-4), due to the fact that of the HOMO level of PbS-QDs presents little change with the sizes of PbS-QDs (E_g >1.2 eV).[154, 162]

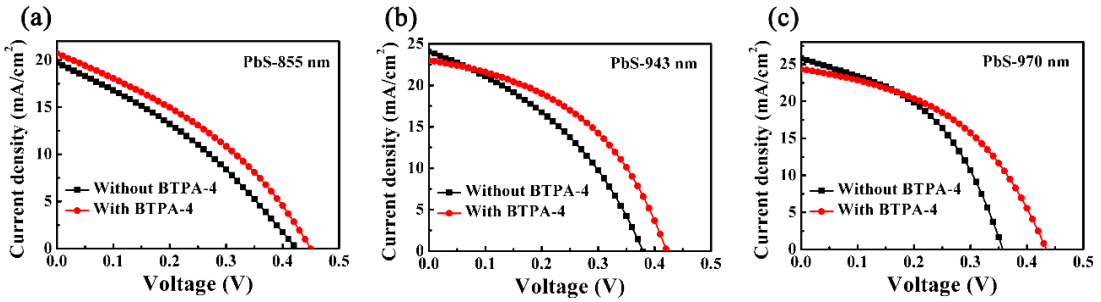

Figure 4-8. *J-V* curves of different sizes PbS based CQDSCs with and without BTPA-4 as hole-selective layer. (a) PbS-QDs with the first exciton peak at 855 nm. (b)PbS-QDs with the first exciton peak at 943 nm. (c) PbS-QDs with the first exciton peak at 970 nm.

Table 4-4. Performance details of different sizes PbS-QDs based CQDSCs with and without BTPA-4 layer. Light intensity for the measurement is AM1.5 G 100 mW/cm^2

First exciton Peak	BTPA-4	J_{sc} (mA/cm^2)	V_{oc} (V)	*FF* (%)	*PCE* (%)
PbS-855 nm	Without	19.7	0.425	32.9	2.75
	With	20.7	0.450	35.5	3.30
PbS-943 nm	Without	24.4	0.384	37.1	3.50
	With	23.0	0.422	44.6	4.33
PbS-970 nm	Without	25.8	0.357	44.8	4.14
	With	24.3	0.434	44.6	4.70

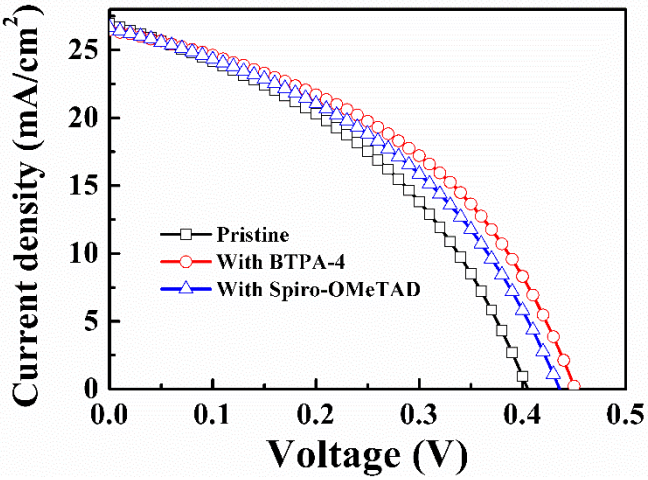

Figure 4-9. *J-V* curves of PbS CQDSCs using BTPA-4 and Spiro-OMeTAD as hole-selective layer.

Table 4-5. Performance details of PbS CQDSCs with BTPA-4 and Spiro-OMeTAD as hole-selective layer.

Devices	J_{sc} (mA/cm^2)	V_{oc} (V)	*FF* (%)	*PCE* (%)
Pristine	26.9	0.405	40.2	4.39
With BTPA-4	26.5	0.451	43.2	5.16
With Spiro-OMeTAD	26.7	0.436	41.3	4.80

As a comparison to BTPA-4, a commonly used hole transport material Spiro-OMeTAD, with "spiro" structure in common with BTPA-4, also was introduced into PbS CQDSCs. Analogous to the devices with BTPA-4, the V_{oc} of PbS CQDSCs with Spiro-OMeTAD also were improved than that of the pristine devices, in Figure 4-9 and Table 4-5. However, comparing with PbS CQDSCs with BTPA-4, the V_{oc} for the devices based on Spiro-OMeTAD is lower. This may be due to the fact that Spiro-OMeTAD (-5.2 eV) has a higher HOMO energy level than that of BTPA-4 (-5.3 eV).[163-164]

These results confirm that the incorporation of the BTPA-4 layer between the PbS-QDs layer and Au electrode forming a *p-i-n* heterojunction structure, is feasibly successful. On one hand, this architecture avoids a Schottky barrier at the PbS-QDs layer/Au electrode interface,[152] resulting in devices with higher *FF*. On the other hand, BTPA-4 can block the electron injection from PbS-QDs to Au electrode, owing its high LUMO energy level (see Figure 4-5c).

4.3.4 V_{oc} Decay and Impedance Spectra of PbS CQDSCs with BTPA-4 as Hole Selective Layer

In order to reveal the effect of BTPA-4 as HSL on charge carrier recombination, the transient open circuit photovoltage (V_{oc}) decay measurements were carried out. Figure 4-10a shows the transient open circuit photovoltage decay curves of PbS CQDSCs with and without the BTPA-4 layer. It can be clearly observed that samples with BTPA-4 exhibit a much slower decay, which provides a direct proof of the reduction

of charge recombination when BTPA-4 is used as a HSL. Generally, in our samples, three photovoltage decay paths are observed: (1) hole trapping in PbS-QDs and electron trapping in ZnO-NWs,[117] (2) charge recombination at ZnO-NWs/PbS-QDs interface, and (3) charge recombination at PbS-QDs/Au electrode interface. Thus, the decay curves can be roughly divided into three parts corresponding to these three charge recombination paths in the PbS CQDSCs. To quantitatively analyze the photovoltage decay processes, the decay curves can be fitted by a triple exponential decay according to the following equation:

$$y(t) = A_1 e^{-t/\tau_1} + A_2 e^{-t/\tau_2} + A_3 e^{-t/\tau_3} \qquad (4\text{-}1)$$

where A_1, A_2 and A_3 are proportionality constants and τ_1, τ_2 and τ_3 are time constants.[165] The fitted curves are shown in Figure 4-9a (solid lines) and the corresponding parameters are shown in Table 4-5. According to the fitting data, for the fast voltage decay process, τ_1 and τ_2 are similar for samples with and without BTPA-4, which should belong to photovoltage decay path (1) and path (2), respectively. Interestingly, for the slow voltage decay process, τ_3 of PbS CQDSCs with BTPA-4 is increased from 21.2 ms to 50.8 ms. This relatively slower voltage decay process of PbS CQDSCs with BTPA-4 may be attributed to the reduction of the interfacial recombination at PbS-QDs/Au electrode interface.

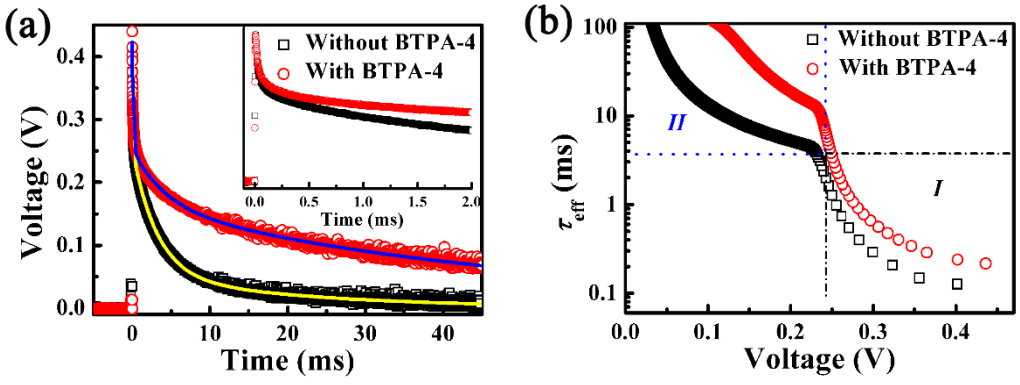

Figure 4-10. (a) Transient open circuit photovoltage (V_{oc}) decay curves for PbS CQDSCs with and without BTPA-4. The inset is an expanded scale of the short time

region of the decay showing the fast V_{oc} decay process of PbS CQDSCs. (b) Effective carrier lifetime calculated from the voltage decay curves shown in (a).

To further gain an insight into the charge recombination processes in PbS CQDSCs, we also evaluated the recombination process based on the effective carrier lifetime (τ_{eff}), which can be defined by the following equation:[135, 165-166]

$$\tau_{\text{eff}} = -\left(\frac{kT}{q}\right)/\left(\frac{dV_{\text{oc}}}{dt}\right) \qquad (4\text{-}2)$$

where k is the Boltzmann constant, T is the temperature, q is the elementary charge. The τ_{eff} was calculated from the voltage decay curves (Figure 4-10a), which is shown in Figure 4-10b. Interestingly, the photovoltage-dependent effective carrier lifetime curves can be separated into two sections, I and II, see Figure 4-10b. In section I, the values of τ_{eff} for both PbS CQDSCs with and without BTPA-4 are close and below 3 ms. It indicates that the BTPA-4 layer has a reduced effect on this recombination process. In section II, the value of τ_{eff} in PbS CQDSCs with BTPA-4 is about 5 times higher than that of the device without BTPA-4. This means that the slower recombination in section II is mostly dominated by interfacial recombination at the PbS-QDs/Au electrode interface. Based on the above results, it can be concluded that BTPA-4 as HSL can significantly diminish the interfacial recombination, thus enhancing the V_{oc} and PCE of PbS CQDSCs.

Table 4-6. Fitted proportionality constants and time constants obtained from the transient open-circuit photovoltage decay curves of the PbS CQDSCs.

Device	A_1 (A_1/(A_1+A_2 +A_3))	τ_1 (μs)	A_2 (A_2/(A_1+A_2 +A_3))	τ_2 (ms)	A_3 (A_3/(A_1+A_2+ A_3))	τ_3 (ms)
Without BTPA-4	0.149	63.2±0.8	0.198	3.1±0.1	0.054	21.2±0.1
With BTPA-4	0.150	139±2	0.102	4.2±0.1	0.188	50.8±0.1

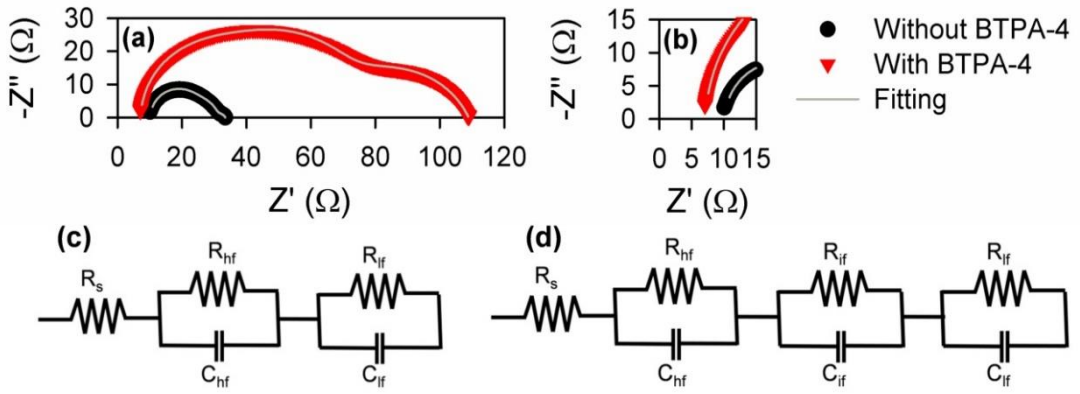

Figure 4-11. Nyquist plot of PbS CQDSCs with and without BTPA-4 HSL in dark with 0.3 V applied bias, (a) full spectra and (b) zoom of the high frequency region where series resistance, R_s, can be easily obtained from the crossing of the impedance spectra with the horizontal axis. Depending on the applied voltage two or three arc features are observed in the impedance spectra. These spectra have been fitted using the equivalent circuit plotted in (c) and (d) respectively. In addition to a R_s each arc feature is fitted by the RC circuit at high, intermediate and low frequencies (hf, if and lf respectively).

Impedance spectroscopy provides a complementary characterization pointing also in this direction. Recombination resistance, R_{rec}, of both kinds of samples has been obtained from the fitting of the impedance spectra using the equivalent circuits plotted in Figure 4-11, based on the work of Wang et al.[167] Briefly, the sum of the low and intermediate frequency resistances, see Figure 4-11, are directly related with the R_{rec} of the system, allowing a qualitative interpretation of the recombination process. Figure 4-12 shows the R_{rec} obtained for samples with and without BTPA-4. As R_{rec} is inversely proportional to the recombination rate, impedance measurements confirm the lower recombination in the devices with the HSL as demonstrated by the lower dark currents and the transient open circuit photovoltage decay measurements, in Figure 4-5d and Figure 4-10a, respectively.

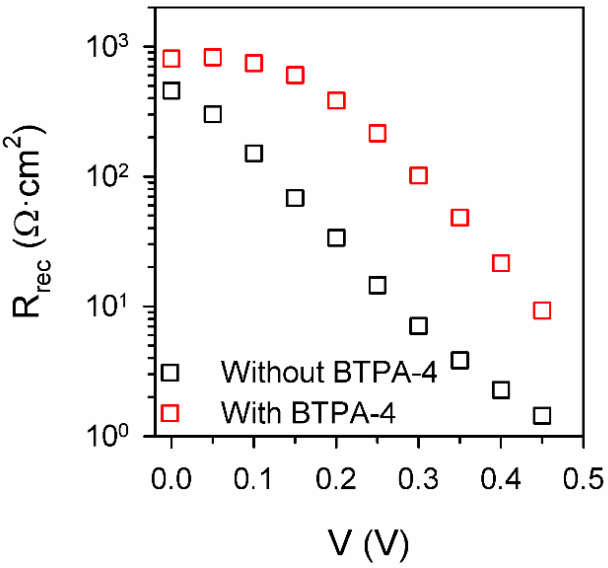

Figure 4-12. Recombination resistance (R_{rec}) of devices with and without BTPA-4 obtained by impedance spectroscopy.

4.3.5 The Stability of PbS CQDSCs with BTPA-4

The stability is a very important issue for the performance evaluation of CQDSCs. Therefore, we also investigated the long-term stability of PbS CQDSCs with and without BTPA-4 layer, which were kept and tested in air without the control of humidity. As shown in Figure 4-13, both the PbS CQDSCs with and without BTPA-4 exhibit excellent long-term storage stability for over 100 days and all of the photovoltaic parameters exhibited overall increase at the first 8 days. After 100 days, the PCE of PbS CQDSCs with BTPA-4 can maintain 5.14% which is a little decrease compared with its maximum value. The PCE value of PbS CQDSCs with BTPA-4 is still higher than that of PbS CQDSCs without BTPA-4 (4.3%), especially for V_{oc}. This result indicates that BTPA-4 is stable enough for the application as a HSL of CQDSCs.

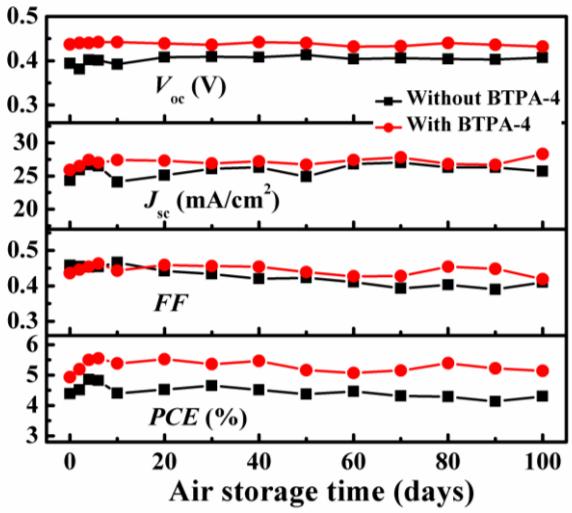

Figure 4-13. Stability evaluation of PbS CQDSCs with and without BTPA-4. The devices were stored and tested in an ambient atmosphere (room temperature: ~ 20°C, indoor relative humidity: 28% ~ 65%).

4.4 Conclusions

In summary, organic small molecule BTPA-4 which has a suitable energy level was used into PbS CQDSCs as a hole-selective layer between the PbS-QDs layer and Au electrode. The *PCE* of PbS CQDSCs was considerably improved by introducing the BTPA-4 layer. BTPA-4 as hole-selective layer can effectively reduce the interfacial charge recombination at PbS-QDs/Au electrode interface and lead to the enhanced V_{oc}. The mechanism behind this achievement was explored using open-circuit voltage decay and impedance spectroscopy. It was observed that the BTPA-4 significantly reduced the interfacial charge recombination, increasing consequently the effective carrier lifetime in PbS CQDSCs. Due to the diminished interfacial recombination in the solar cells, the PCE of PbS CQDSCs with BTPA-4 is obtained as high as 5.55%, which is an increase by about 15% comparing with the cell without BTPA-4 and maintains it in the long-term period (over 100 days). The results demonstrate that BTPA-4 may have diverse applications in enhancing photovoltaic devices.

The originalities of this work are: (1) novel hole transport material BTPA-4 was synthesized; (2) organic small molecule was used to suppress the interfacial recombination in QDSCs for the first time.

Chapter 5: Organic-Inorganic Hybrid Perovskite Solar Cells with Novel Hole Transport Materials

5.1 Introduction

In recent years, perovskite solar cells (PSCs) have attracted more and more world-wide interest for practical applications due to their excellent absorption characteristics, superior charge transporting property, and high power conversion efficiencies (PCE).[168-171] Up to now, the PCE of over 20% has been reported.[172] Hole transport materials (HTMs), which also work as protection layer against humidity, are one of the most important components in PSCs. Small molecular HTMs, such as squaraine derivatives,[173] carbazole derivatives,[174-177] linear conjugated molecules,[178] Spiro-OMeTAD (2,2',7,7'-tetrakis(*N*,*N*'-di-*p*-methoxyphenylamine)-9,9'-spirobifluorene) derivatives,[179-180] oligothiophene derivatives,[181] butadiene derivatives,[182] a 1,3,4-oxadiazole derivative,[183] triphenylamine derivatives,[184-185] various thiophene derivatives,[181, 186-192] a tetrathiafulvalene derivative,[193] and silafluorene derivatives,[194] have been utilized in efficient PSCs owing to their excellent charge carrier transport property. Besides being used as the building blocks of π-conjugated polymers and oligomers,[195-196] spiro-type compounds have been successfully synthesized as the central bridge in small molecular HTMs to improve their good charge transporting property, inhibit aggregation on the perovskite surface, and suppress the charge recombination.[179, 191, 197-198] The Spiro-OMeTAD, which is a spirobifluorene (SBF) derivative with its unique steric hindrance effect, has been the main HTM studied in PSCs. However, high synthesis cost and complex purification along with the requirement of dopants are the major constraining factors in its commercial large scale applications of the solid-state PSCs. It is of great challenge to develop new spiro-type molecules with convenient synthetic methods.

Table 5-1. Comparison of estimated materials synthesis cost for the synthesis of studied HTMs and Spiro-OMeTAD.[a]

HTMs	Steps	Reagents(materials) cost ($/g)	Workup cost ($/g)	Total cost ($/g)
BTPA-4	3	13.72	17.13	30.85
BTPA-5	3	12.29	15.96	28.25
BTPA-6	3	17.65	17.67	35.32
Spiro-OMeTAD	6	6.14	85.06	91.20

[a] For every reaction step, the total cost of every reactant, catalyst, reagent and solvent was calculated to get 1 gram of the target HTM to be settled in US dollar.

The synthesis of functionalized spiro(fluorene-9,9'-xanthene) (SFX) significantly decreases the production cost compared with that of SBF (see Table 5-1). The addition of oxygen atom from spiro-type SBF to SFX can not only provide the opportunity to improve both the solubility and processability, but also offer the ability to tune their optical properties. We have recently reported the synthesis of BTPA-4 (see Figure 5-1 for structure) and employed it as a hole-selective layer (HSL) in heterojunction PbS colloidal quantum dot solar cells (CQDSCs).[199] The BTPA-4 HSL outperformed Spiro-OMeTAD HSL in CQDSCs, which suggested that the SFX unit in BTPA-4 is a promising structural unit in designing HTMs for PSCs as well.

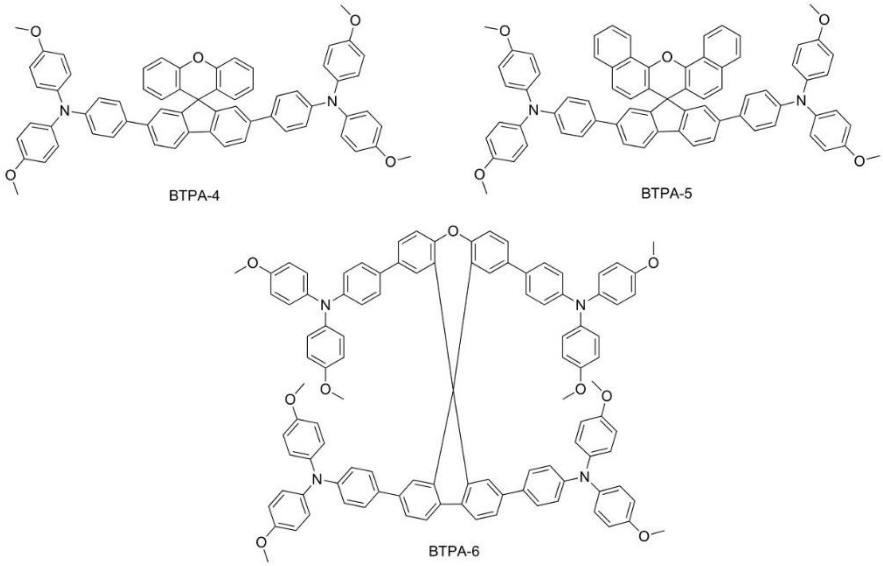

Figure 5-1. Molecular structures of three HTMs studied.

Herein, Dr. Wu of Nihon University synthesized SFX-bridged triphenylamine-based HTMs, BTPA-4 and two novel HTMs with a varied bridge structure (BTPA-5) and with different numbers (four) of the triphenylamine units (BTPA-6) as shown in Figure 5-1. These materials can be prepared with costs about one third of that for the preparation of Spiro-OMeTAD (see Table 5-1). We cooperated with Prof. Otsuki and Dr. Wu investigated the perovskite solar cell performance of these three materials as the HTMs with Spiro-OMeTAD as a reference compound.

5.2 Experimental Methods

The synthetic route of BTPA-5, and BTPA-6 is shown in Scheme 5-1. All these three HTMs need only three reaction steps from the starting material 9-fluorenone, which is much more convenient compared with the synthesis of spiro-OMeTAD as shown in Table 5-1.

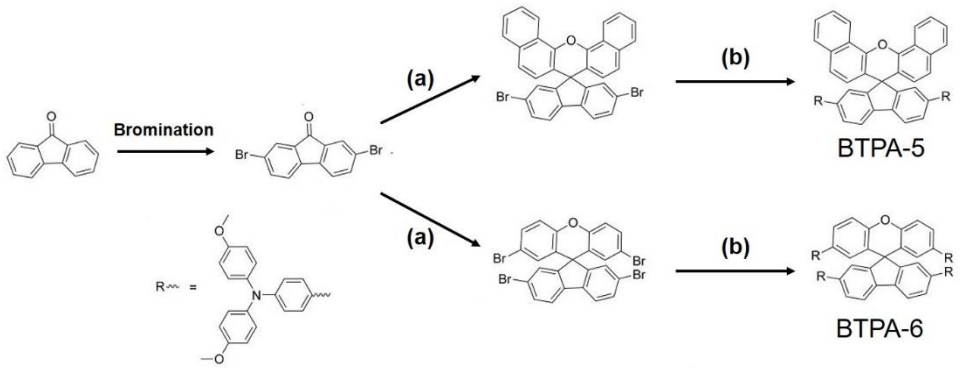

Scheme 5-1. Synthetic route of BTPA-5 and BTPA-6. (a) naphthalen-1-ol for BTAP-5, or 4-bromophenol for BTPA-6, methanesulfonic acid, 150 °C, 24 h; (b) *N*,*N*-bis(4-methoxyphenyl)-4-(4,4,5,5-tetramethyl-1,3,2-dioxaborolan-2-yl)benzenamine, tetrohydrofuran (THF), $Pd(PPh_3)_4$, 85 °C, 48 h.

Synthesis of BTPA-5. BTPA-5 was synthesized following a procedure similar to that we used for BTPA-4, [199] except that naphthalen-1-ol (400 mg, 0.68 mmol) was used instead of phenol. BTPA-5 was obtained as a yellow solid (408 mg, 0.39 mmol, 58%). ^{1}H NMR (400 MHz, $CDCl_3$): δ ppm: 8.76 (d, 2 H, J = 8.4 Hz), 7.87 (d, 2 H, J = 8.4 Hz), 7.74 (d, 2 H, J = 8.4 Hz), 7.69 (d, 2 H, J = 7.6 Hz), 7.61 (d, 2 H, J = 8.0 Hz), 7.54 (t, 2 H, J = 7.2 Hz), 7.30 (s, 2 H), 7.25 (d, 2 H, J = 8.0 Hz), 7.24 (d, 4 H, J = 8.0

Hz), 6.96 (d, 8 H, *J* = 8.4 Hz), 6.82 (d, 4 H, *J* = 8.4 Hz), 6.74 (d, 8 H, *J* = 9.2 Hz), 6.51 (d, 2 H, *J* = 8.8 Hz), 3.74 (s, 12 H). ^{13}C NMR (100 MHz, $CDCl_3$): δ ppm: 156.8, 155.6, 147.9, 145.7, 140.8, 140.7, 138.0, 133.4, 132.6, 127.5, 127.3, 126.5, 126.2, 126.1, 125.8, 124.5, 124.2, 123.0, 121.6, 120.8, 120.0, 118.2, 114.5, 55.3, 54.3. APCI-HRMS *m/z* ($[M+H]^+$): calcd: 1039.4111, found: 1039.4110. Anal. calcd for $C_{73}H_{54}N_2O_5 \cdot 0.2\ CHCl_3$: C, 82.70; H, 5.14; N, 2.64. Found: C, 82.82; H, 5.06; N, 2.58.

Synthesis of BTPA-6. BTPA-6 was synthesized following a procedure similar to that we used for BTPA-4, except that 4-bromophenol (400 mg, 0.62 mmol) was used instead of phenol. BTPA-6 was obtained as a yellow solid (450 mg, 0.29 mmol, 47%). ^{1}H NMR (400 MHz, $CDCl_3$): δ ppm: 7.79 (d, 2 H, *J* = 8.2 Hz), 7.57 (d, 2 H, *J* = 8.0 Hz), 7.41~7.27 (m, 10 H), 7.04 (d, 12 H, *J* = 9.2 Hz), 6.99 (d, 8 H, *J* = 8.8 Hz), 6.91 (d, 4 H, *J* = 8.4 Hz), 6.80 (m, 20 H), 6.68 (s, 2 H), 3.78 (s, 12 H), 3.77 (s, 12 H). ^{13}C NMR (100 MHz, $CDCl_3$): δ ppm: 156.0, 155.8, 150.6, 148.1, 147.7, 140.9, 140.7, 138.1, 136.1, 132.9, 132.5, 127.6, 127.2, 125.9, 125.3, 123.5, 120.9, 120.8, 120.3, 117.2, 114.7, 55.5, 54.7. APCI-HRMS *m/z* ($[M+2H]^{2+}$): calcd: 1546.6394, found: 1546.6373. Anal. calcd for $C_{105}H_{84}N_4O_9 \cdot 0.2\ CHCl_3$: C, 78.92; H, 5.30; N, 3.49. Found: C, 78.93; H, 5.27; N, 3.49.

Fabrication of PSCs. First, a cleaned FTO-substrate was coated with a thickness of 60 nm TiO_2 compact layer (TiO_2-CL). Then a mesoporous TiO_2 film was deposited on the TiO_2-CL coated substrate by spin coating (3000 rpm, 30s) from an ethanol solution of diluted TiO_2 paste (30 nm particle Dyesol-30NRD, Dyesol) with a mass ratio of 1:4 followed by drying at 120 °C for 5 min and sintered for 510 °C for 40 min in air. After annealing, the mesoporous TiO_2 (mp-TiO_2) substrates were quickly transferred to a N_2 glovebox at high temperature (above 100 °C). Subsequently, a 1.25 M $CH_3NH_3PbI_3$ perovskite precursor dimethyl sulfoxide solution, which was stirred at 70 °C for 1 h, was deposited on the 60 °C heat-treated mp-TiO_2 substrate by two consecutive spin coating steps at 1000 rpm for 10 s followed by 5000 rpm for 30 s. After starting the second spin-coating stage, 400 μL of chlorobenzene was dropped onto the spinning substrate at last 10 s. Then the substrate was heat-treated at 100 °C for 30 min on a hotplate.

The HTM solutions were then deposited on the individual perovskite films by spin-coating and these solutions were prepared by the following details. HTMs were each dissolved in 1 mL chlorobenzene (20 mM for BTPA-4, BTPA-5, and BTPA-6) or spiro-OMeTAD (60 mM) with 4-*tert*-butylpyridine (t-BP, 24 μL) and a certain amount of bis(trifluoromethylsulfonyl)imide lithium salt (LiTFSI). For BTPA-4, BTPA-5, and BTPA-6, 0.032 mM LiTFSI acetonitrile solution (17.5 μL) was used, while for Spiro-OMeTAD, 0.043 mM LiTFSI acetonitrile solution (72 μL) was used. The spin-coating process was carried out at 4000 rpm for 30 s. All the hole conducting materials were spin-coated on $CH_3NH_3PbI_3$/mp-TiO_2/TiO_2-CL/FTO. Finally, 100 nm thickness gold was deposited by thermal evaporation under vacuum to complete the fabrication of the solar cells. The active areas of all the cells were 0.35 cm^2.

5.3 Results and Discussion

5.3.1 Optical Property

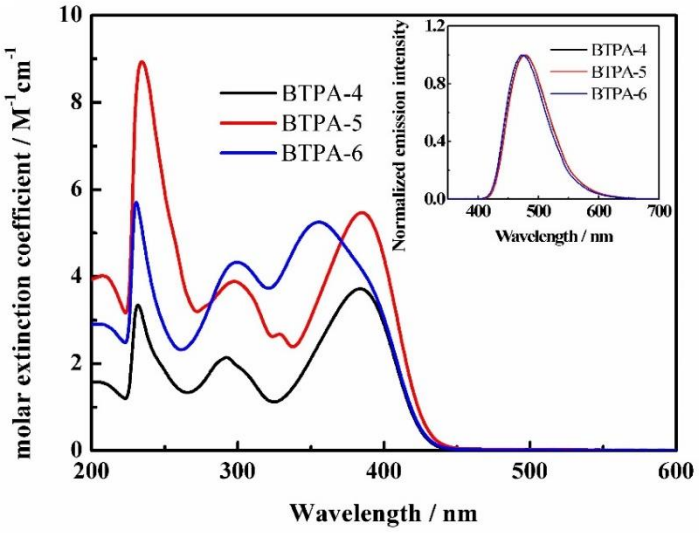

Figure 5-2. UV−Vis absorption spectra of BTPA-4, BTPA-5, and BTPA-6 in CH_2Cl_2 solution (2.0×10^{-5} mol L^{-1}). Inset shows their normalized photoluminescence spectra in CH_2Cl_2 solution.

The UV-Vis absorption spectra of BTPA-4, BTPA-5, and BTPA-6 in CH_2Cl_2 solution along with their normalized photoluminescence (PL) spectra are shown in

Figure 5-2 and the relevant data are summarized in Table 5-2. The π-π* absorption bands for BTPA-4, BTPA-5, and BTPA-6 are observed at 384 nm, 385 nm, and 356 nm, respectively. BTPA-5 with additional benzo groups, compared to BTPA-4, shows only slight changes in absorption wavelengths but exhibited a significant increase in the absorption coefficients. Although BTPA-6 shows a blue-shifted absorption peak compared to BTPA-4 and BTPA-5, there is another shoulder with lower molar extinction coefficient for BTPA-6 at the same peak position for BTPA-4 and BTPA-5. These observations well agreed with the calculated results (TDDFT, B3LYP/6-31G), which showed that the excitation energies from the HOMO to the LUMO were 410 nm for BTPA-4, 411 nm for BTPA-5, and 407 nm for BTPA-6, with the oscillator strengths about 1.5. Additionally, these three HTMs possess the similar absorption edges and PL spectra (478 nm for BTPA-4, 479 nm for BTPA-5, 473 nm for BTPA-6), which implies small influences of the structural variations of the SFX core on the singlet excited state energy levels.

Table 5-2. The photochemical and electrochemical properties of the three HTMs.

Materials	E_{HOMO} (eV vs vacuum) [a]	$E_{0\text{-}0}$ (eV) [b]	E_{LUMO} (eV vs vacuum) [c]	Conductivity (S cm^{-1}) [d]
BTPA-4	-5.35	2.90	-2.45	1.49×10^{-4}
BTPA-5	-5.37	2.89	-2.48	6.42×10^{-5}
BTPA-6	-5.34	2.91	-2.43	5.60×10^{-5}

[a] HOMO potential vs vacuum was obtained from HOMO = – 4.5 – E_{ox}; [b] $E_{0\text{-}0}$ was calculated from the intersection of the normalized absorption and florescence spectra; [c] LUMO potential was obtained from: LUMO = HOMO + $E_{0\text{-}0}$; [159-160, 200] [d] Pristine HTM without doping.

5.3.2 Electrochemical Properties

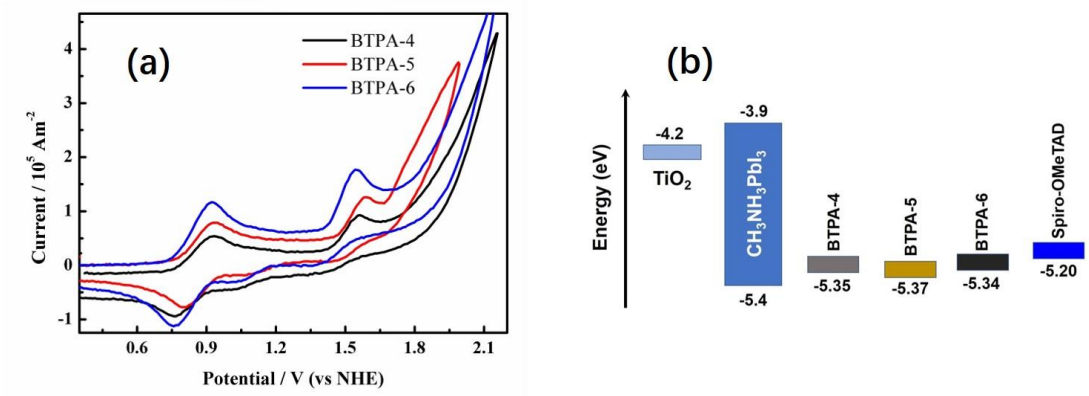

Figure 5-3. Energy levels of the HTMs. (a) Cyclic voltammograms of BTPA-4, BTPA-5, and BTPA-6 in CH_2Cl_2 containing 0.1 M $TBAPF_6$; (b) Energy diagram of $CH_3NH_3PbI_3$ perovskite solar cell with various HTMs.

To investigate their redox property, cyclic voltammetry was carried out in CH_2Cl_2 solution. The voltammetry curves are shown in Figure 5-3a and the relevant data are summarized in Table 5-2. The HOMO energy levels of these three HTMs were determined on the basis of the following equation: $E_{HOMO} = -4.5 - E°(S^+/S)$ (eV),[158] where $E°(S^+/S)$ is the first oxidation potential value vs SHE (standard hydrogen electrode). Their $E°(S^+/S)$ are 0.85 V for BTPA-4, 0.87 V for BTPA-5, and 0.84 V for BTPA-6, respectively. All the three materials show rather similar HOMO energy levels to each other, with -5.35 eV, -5.37 eV, and -5.34 eV for BTPA-4, BTPA-5, and BTPA-6, respectively. Figure 3b shows the energy level diagram of all the components in PSCs. The HOMO energy levels of our three HTMs are located above the valence-band level of the perovskite $CH_3NH_3PbI_3$ (−5.44 eV [201]) as can be seen by the band alignment, and thus have matched energy levels for $CH_3NH_3PbI_3$ PSCs with TiO_2 as the electron transport layer.

5.3.3 Water Contact Angle

Figure 5-4. Water contact angles of BTPA-4, BTPA-5, and BTPA-6 coated films on glass.

It has been known that perovskite materials are easily decomposed by humidity due to the hygroscopic ammonium salts.[202-203] HTMs also play an important role of preventing water penetration into the surface of perovskite material and thus it is valuable to investigate water contact angles of HTMs. As shown in Figure 5-4, the water contact angles of the HTM-coated films were 76° for BTPA-4, 75° for BTPA-5, and 73° for BTPA-6. In comparison with reported 70° for Spiro-OMeTAD,[203] these three HTMs show gently higher hydrophobic properties, which may enhance their perovskite solar cell stabilities.

5.3.4 Device Performance of PSCs

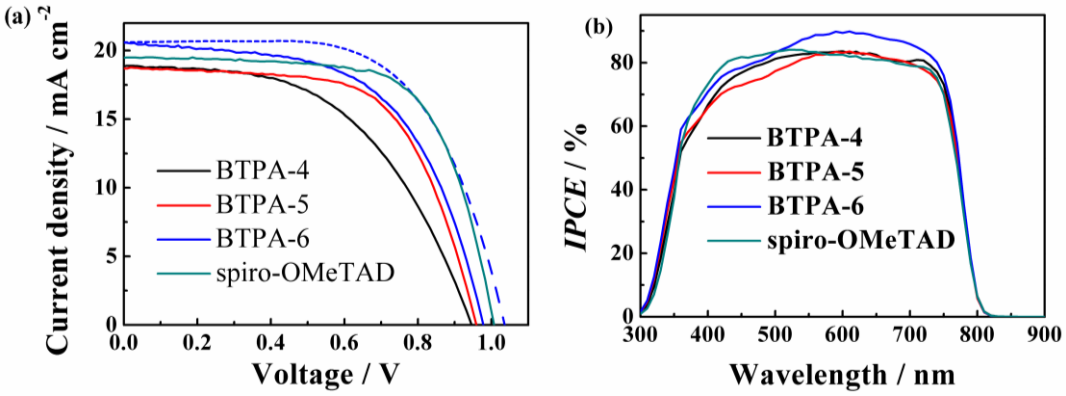

Figure 5-5. Device performance of PSCs based on BTPA-4, BTPA-5, BTPA-6, and Spiro-OMeTAD in the forward scan (solid line) and in the reverse scan (dashed line for BTPA-6). (a) Current density-voltage curves, (b) IPCE curves

Then we fabricated PSCs with BTPA-4, BTPA-5, or BTPA-6 and Spiro-OMeTAD for comparison as HTMs in the presence of dopants including LiTFSI and t-BP. The addition of these dopants has shown mixed effects on the overall performance of PSCs. Doping the HTMs with LiTFSI promote ingression of oxygen which eventually leads to better hole extraction due to their deliquescent behaviour.[193] However, to control the amount of oxidized Spiro-OMeTAD via addition of LiTFSI has yet remained as a challenge for consistent results.[204] Thereby we have used a low molar concentration of LiTFSI in our HTMs during the fabrication of PSCs. The corresponding

photovoltaic performances of PSCs measured under AM1.5, 100 mW cm^{-2} are collected in Table 5-3. Figure 5-5 showed the current density–voltage (*J–V*) characteristics obtained using these HTMs with the reverse or forward scans under 100 mW cm^{-2} (AM1.5G) solar illumination. The device with BTPA-6 possesses a short-circuit current density (J_{sc}) of 20.57 mA cm^{-2}, an open-circuit voltage (V_{oc}) of 978 mV, and a fill factor (*FF*) of 0.575, yielding PCE of 11.57% for the forward scan and 20.61 mA cm^{-2}, 1036 mV, 0.647, 13.81% in the reverse scan, respectively. Small differences were obtained between the forward and reverse scans in J_{sc} while a little larger difference was observed in V_{oc} and FF values. The standard Spiro-OMeTAD-based PSC was fabricated in similar condition (without overnight storage in low humidity) showed a PCE of 13.25% with a J_{sc} of 19.50 mA cm^{-2}, a V_{oc} of 1007 mV, and FF of 0.674. The incident photon-to-current conversion efficiency (IPCE) spectra of these solar cell devices as a function of wavelength are shown in Figure 5-5b. BTPA-4 based PSC showed IPCE of 80% over the visible region and >70% in the 400 nm-470nm range. BTPA-5 showed IPCE of 80% within 530nm to 800nm region. It is noticed that BTPA-6 exhibits the best IPCE value particularly in the 500–800 nm range, which was higher than the Spiro-OMeTAD based PSC in the same wavelength and in good accordance with the largest observed J_{sc}.

Table 5-3. The PSC parameters of BTPA-4, BTPA-5, BTPA-6, and Spiro-OMeTAD.

HTM	J_{sc} (mA cm^{-2})	V_{oc} (V)	FF	PCE (%)	Scan direction
BTPA-4	18.91	0.946	0.515	9.21	forward
BTPA-5	18.70	0.959	0.630	11.30	forward
BTPA-6	20.57	0.978	0.575	11.57	forward
	20.61	1.036	0.647	13.81	reverse
Spiro-OMeTAD	19.50	1.007	0.674	13.25	forward

The Nyquist plots for three PSC devices with one of BTPA-4, BTPA-5, and BTPA-6 as the HTMs as well as the standard Spiro-OMeTAD PSC device under a bias potential ranging from 0 to 900 mV in the dark with the frequency range from 1 M Hz

to 1 Hz are given in Figures 5-6a–d. Approximately three interfacial processes with different time constants can be extracted from the EIS spectra. These processes are, in the order of increasing frequency ranges, a process which is associated with slow dynamics possibly related to the hysteresis behaviors in the perovskite,[205] the charge recombination at the TiO_2/perovskite/HTM interface modeled by a recombination resistance (R_{rec}) in parallel with a chemical capacitance (C_{rec}), and the charge transfer at the HTM/Au interface modeled by a resistance (R_{HTM}) in parallel with a capacitance (C_{HTM}).[206] We have fitted the latter two processes in addition to the series resistance R_s with the equivalent circuit shown in Figure 5-6g. The fitted R_s values were found to be in the order of BTPA-4 > BTPA-6 > BTPA-5 > Spiro-OMeTAD, which was in accord with the order of *FF* of the respective devices in the forward scan. As shown in Figures 5-6a–d), it is noticed that the arcs representing the slow processes at low frequency ranges and the recombination at medium frequency ranges markedly decrease with increasing bias from 0 V to 0.9 V due to the gradual elevation of the Fermi level of mesoscopic TiO_2 and the enhancement of recombination. This trend is manifested in the decreasing R_{rec} with increasing bias voltages, as shown in Figure 5-6e. At the same forward bias voltage, the order of the recombination resistance was found to be in the order of BTPA-4 < BTPA-5 < BTPA-6 < Spiro-OMeTAD, indicating that the electron blocking capability of the HTM is in this order. This is also apparent from the Nyquist plots of PSCs with different HTMs at the same 0.8 V bias. This trend is in good agreement with the V_{oc} trend of their corresponding solar cells in the forward scan as shown in Table 5-3.

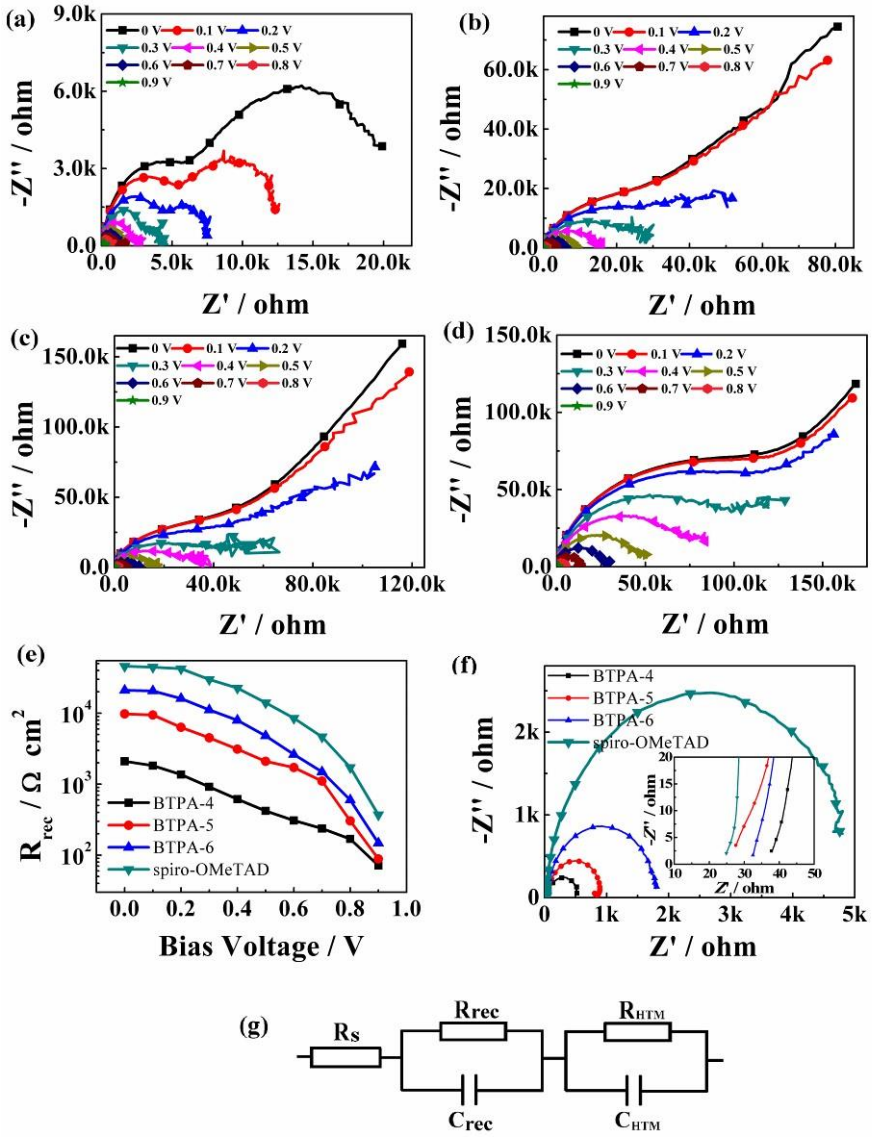

Figure 5-6. Electrochemical impedance spectroscopy for PSC devices with different HTMs measured at different bias potentials in dark conditions. Nyquist plots for PSCs with (a) BTPA-4, (b) BTPA-5, (c) BTPA-6, (d) Spiro-OMeTAD. (e) Dependence of the fitted charge transfer resistance (R_{rec}) on the bias potentials from 0 V to 0.9 V. (f) Comparison of different HTMs at the same bias potential of 800 mV; (g) Equivalent circuit model.

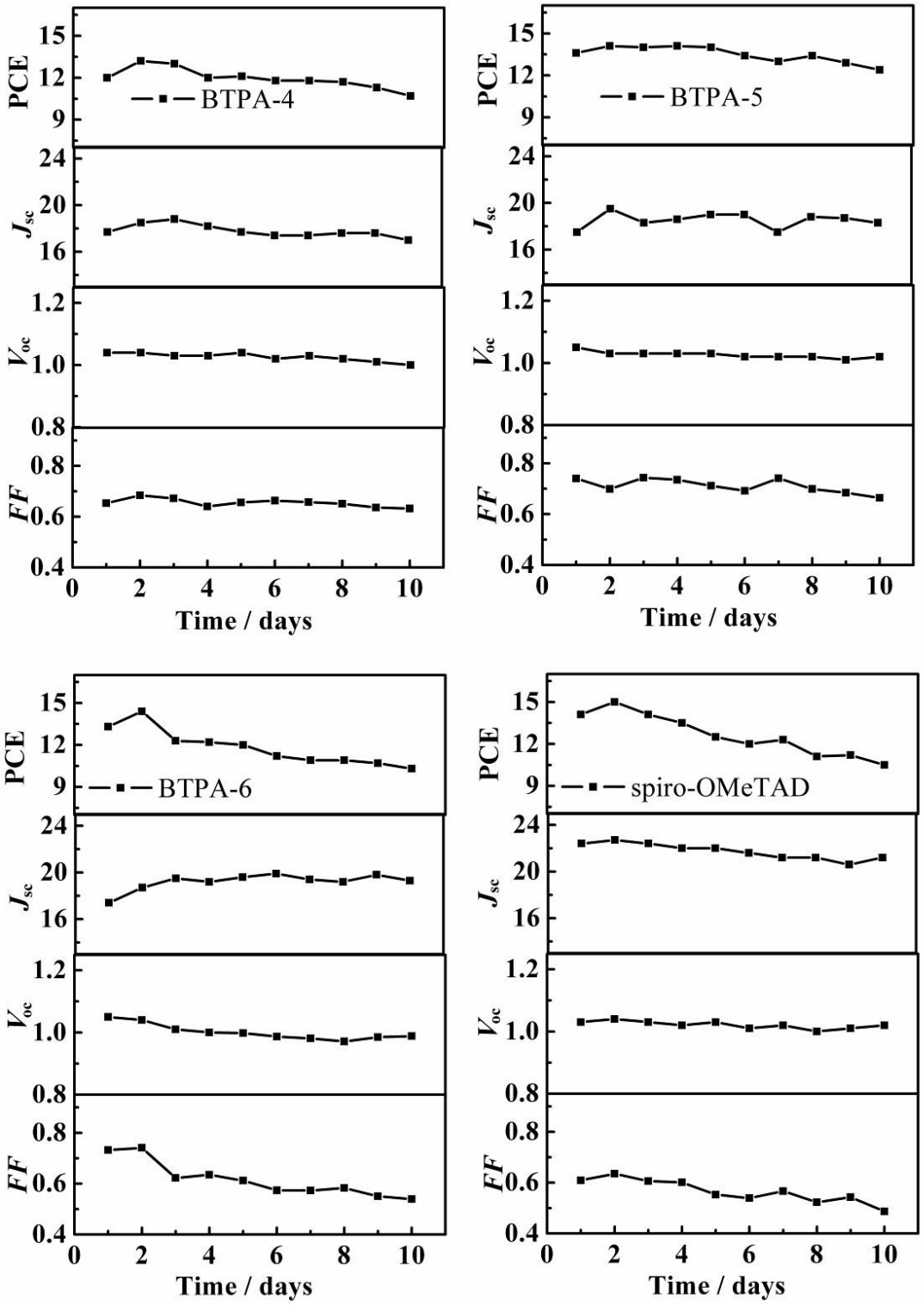

Figure 5-7. The long–term stability of the PSCs based on BTPA-4, BTAP-5, BTPA-6, and Spiro-OMeTAD. Data were obtained by the reverse scan.

The long-term stability is also a vital issue for PSCs. We investigate the stability of the PSC devices based on BTPA-4, BTPA-5, BTPA-6, and the standard Spiro-OMeTAD, which were kept in the dark with the humidity of 25%. The PSCs were measured over a period of 10 days to observe their performances in the long run. After one day, the solar cell efficiencies for these four HTMs were significantly increased and after that day, the device performances were declined as the aging time increased, which may be ascribed to the slow infiltration of water from air.[207] The highest PCEs in the reverse scan at the second day were 13.2% for BTPA-4, 14.1% for BTPA-5, 14.4% for BTPA-6, and 15.0% for Spiro-OMeTAD, respectively. The respective PCEs became 10.7%, 12.4%, 10.3%, and 10.5%. It is remarkable that the PSC with BTPA-5 exhibited a better PCE than the cells with the other HTMs, even exceeding a cell with Spiro-OMeTAD by a margin as large as 2%. Furthermore, the cells with BTPA-4 and BTPA-6 showed comparable efficiencies with a cell with Spiro-OMeTAD after 10 days. Here a conclusion can be made that BTPA-4, BTPA-5, and BTPA-6 based devices showed better long-term stability than Spiro-OMeTAD based one, which is in good agreement with the result of water contact angle test.

5.4 Conclusions

In conclusion, we have developed two novels small molecular HTMs, BTPA-5 and BTPA-6, by employing the SFX core as the central bridge in triarylamine-based materials. In addition, we have also applied analogous BTPA-4, which we have developed for CQDSCs, as a HTM in PSCs for the first time. These there HTMs exhibit characteristics of easy synthesis, low-cost, well-matched HOMO level alignment, and high solubility in commonly used organic solvents, which makes them suitable for $CH_3NH_3PbI_3$-based PSCs. We have then investigated the effect of the molecular structural modification of these three HTMs on their optical properties, electrochemical properties, water contact angles as well as device performances in detail. Among them, the BTPA-6-based solar cell device yielded a PCE of 11.57% in the forward scan with the best J_{sc} and V_{oc} values due to the highest IPCE value in the visible region and the largest recombination resistance, which was comparable to the cell fabricated with the standard Spiro-OMeTAD. Notably, the SFX derivatives

(BTPA-4, BTPA-5, and BTPA-6) based devices showed superior long-term stability than Spiro-OMeTAD based one. Particularly, the present results highlight BTPA-6 with its low cost and facile synthesis as highly competitive a HTMs for future large-scale application in PSCs.

The originalities of this work are: (1) low cost hole transport materials BTPA-5 and BTPA-6 were synthesized; (2) BTPA-4, BTPA-5, and BTPA-6 were used to be as hole transport layer in perovskite for the first time.

Chapter 6: Summary and Prospective

Long-term air-stable and high efficiency PbSe CQDSCs were obtained by using TBAI as ligand in solid state ligand-exchange process, and it is realized that the whole processes: from PbSe QDs washing step to PbSe CQDSCs fabrication, storage and measurements are all in ambient atmosphere. In addition, ligand-dependent performance of PbSe QD films and CQDSCs were systematically investigated. We confirmed that TBAI treatment can produce more air-stable and higher charge transfer rate PbSe QD films than mercapto organic short ligands (EDT and MPA). Due to less surface trap density and higher charge transfer rate in the solar cells, the PCE of TBAI treated large size PbSe CQDSCs is obtained as high as 3.53%. The mechanism behind this achievement was explored. It was informed that the TBAI treatment significantly reduced the intrinsic hole trapping-assisted recombination in PbSe layer and improved the effective carrier lifetime in the PbSe CQDSCs.

BTPA-4 as hole-selective layer can effectively reduce the interfacial charge recombination at PbS-QDs/Au electrode interface and lead to the enhanced V_{oc}. It was observed that the BTPA-4 significantly reduced the interfacial charge recombination, increasing consequently the effective carrier lifetime in PbS CQDSCs. Due to the diminished interfacial recombination in the solar cells, the PCE of PbS CQDSCs with BTPA-4 is obtained as high as 5.55%, which is an increase by about 15% comparing with the cell without BTPA-4 and maintains it in the long-term period (over 100 days).

Three hole transport materials BTPA-4, BTPA-5 and BTPA-6, by employing the SFX core as the central bridge in triarylamine-based materials were introduced into PSCs. These three HTMs exhibit characteristics of easy synthesis, low-cost, well-matched HOMO level alignment, and high solubility in commonly used organic solvents, which makes them suitable for $CH_3NH_3PbI_3$-based PSCs. We have then investigated the effect of the molecular structural modification of these three HTMs on their optical properties, electrochemical properties, water contact angles as well as device performances in detail. Among them, the BTPA-6-based PSC device yielded a PCE of 11.57% in the forward scan with the best J_{sc} and V_{oc} values due to the highest IPCE value in the visible region and the largest recombination resistance, which was

comparable to the cell fabricated with the standard Spiro-OMeTAD.

For CQDSCs, reducing the surface defects of QDs and the interfacial recombination in solar cells are still the most effective way to get high performance CQDSCs. Finding a new efficient surface ligand, developing new QDs deposition technology and treatment method, effectively using the hot carrier of QD will become the future development direction. For PSCs, getting stable and less toxic devices are the most important issues. Developing inorganic perovskite materials and perovskite quantum dot will become the future development direction. Moreover, charge dynamics investigation of CQDSCs and PSCs will also take a large part and play an important role in the future development.

Bibliography

[1] Muraoka, K.; Wagner, F.; Yamagata, Y.; Donne, A. J. H. "Short- and long-range energy strategies for Japan and the world after the Fukushima nuclear accident", Journal of Instrumentation, 2016, 11, 18.

[2] EIA. "U.S. energy consumption by energy source, 2015". http://www.eia.gov/energyexplained/?page=renewable_home.

[3] Tang, Jiang. "Materials Engineering for Stable and Efficient PbS Colloidal Quantum Dot Photovoltaics", ProQuest, 2010.

[4] Gray, Jeffery L. "Handbook of Photovoltaic Science and Enginnering″. John Wiley and Sons Ltd.: 2002.

[5] Green, M. A. "Solar cells: Operating principles, technology, and system applications″. Englewood Cliffs, NJ, Prentice-Hall, Inc.,: 1982.

[6] NREL. Efficiency Chart; 2017.

[7] Green, Martin A.; Emery, Keith; Hishikawa, Yoshihiro; Warta, Wilhelm; Dunlop, Ewan D.; Levi, Dean H.; Ho-Baillie, Anita W. Y. "Solar cell efficiency tables (version 49)", Progress in Photovoltaics: Research and Applications, 2017, 25, 3-13.

[8] Gibbs, Markelle Lewis. "Construction and Analysis of PbSe Quantum Dot Heterojunction Solar Cells", ProQuest, 2014.

[9] Chopra, K. L.; Paulson, P. D.; Dutta, V. "Thin-film solar cells: an overview", Progress in Photovoltaics: Research and Applications, 2004, 12, 69-92.

[10] Shockley, William; Queisser, Hans J. "Detailed Balance Limit of Efficiency of p-n Junction Solar Cells", Journal of Applied Physics, 1961, 32, 510-519.

[11] Midgett, Aaron G. "Ultrafast Optical Studies of Multiple Exciton Generation in Lead Chalcogenide Quantum Dots", ProQuest, 2010.

[12] Cirloganu, Claudiu M.; Padilha, Lazaro A.; Lin, Qianglu; Makarov, Nikolay S.; Velizhanin, Kirill A.; Luo, Hongmei; Robel, Istvan; Pietryga, Jeffrey M.; Klimov,

Victor I. "Enhanced Carrier Multiplication in Engineered Quasi-Type-II Quantum Dots", Nature Communications, 2014, 5, 4148.

[13] Klimov, V. I.; Mikhailovsky, A. A.; McBranch, D. W.; Leatherdale, C. A.; Bawendi, M. G. "Quantization of Multiparticle Auger Rates in Semiconductor Quantum Dots", Science, 2000, 287, 1011-1013.

[14] Pietryga, Jeffrey M.; Zhuravlev, Kirill K.; Whitehead, Michael; Klimov, Victor I.; Schaller, Richard D. "Evidence for Barrierless Auger Recombination in PbSe Nanocrystals: A Pressure-Dependent Study of Transient Optical Absorption", Physical Review Letters, 2008, 101, 217401.

[15] Nozik, A. J. "Quantum Dot Solar Cells", Physica E: Low-dimensional Systems and Nanostructures, 2002, 14, 115-120.

[16] Hanna, Mark C.; Beard, Matthew C.; Nozik, Arthur J. "Effect of Solar Concentration on the Thermodynamic Power Conversion Efficiency of Quantum-Dot Solar Cells Exhibiting Multiple Exciton Generation", Journal of Physical Chemistry Letters, 2012, 3, 2857-2862.

[17] Kim, Mee Rahn; Ma, Dongling. "Quantum-Dot-Based Solar Cells: Recent Advances, Strategies, and Challenges", The Journal of Physical Chemistry Letters, 2014, 6, 85-99.

[18] Prinz, Gary A. "Magnetoelectronics", Science, 1998, 282, 1660-1663.

[19] Grunberg, P. "Layered magnetic structures: History, highlights, applications", Physics Today, 2001, 54, 31-37.

[20] Dedigamuwa, Gayan S. "Fabrication and Characterization of Surfactant-Free Lead Selenide Quantum Dot Films and Lead Selenide-Polymer Hybrid Structures", ProQuest, 2010.

[21] Vanmaekelbergh, Daniel; Liljeroth, Peter. "Electron-Conducting Quantum Dot Solids: Novel Materials Based on Colloidal Semiconductor Nanocrystals", Chemical Society Reviews, 2005, 34, 299-312.

[22] Semonin, Octavi E.; Luther, Joseph M.; Beard, Matthew C. "Quantum Dots for Next-Generation Photovoltaics", Materials Today, 2012, 15, 508-515.

[23] Hughes, Barbara Katherine. "Manipulation of Composition, Morphology, and Surface Chemistry of Semiconductor Quantum Dots for Enhanced Photophysics", ProQuest, 2005.

[24] Klimov, Victor I. "Optical Nonlinearities and Ultrafast Carrier Dynamics in Semiconductor Nanocrystals", The Journal of Physical Chemistry B, 2000, 104, 6112-6123.

[25] Chen, Guanying; Seo, Jangwon; Yang, Chunhui; Prasad, Paras N. "Nanochemistry and Nanomaterials for Photovoltaics", Chemical Society Reviews, 2013, 42, 8304-8338.

[26] Kramer, Illan J.; Sargent, Edward H. "Colloidal Quantum Dot Photovoltaics: A Path Forward", ACS Nano, 2011, 5, 8506-8514.

[27] Luther, Joseph M.; Law, Matt; Beard, Matthew C.; Song, Qing; Reese, Matthew O.; Ellingson, Randy J.; Nozik, Arthur J. "Schottky Solar Cells Based on Colloidal Nanocrystal Films", Nano Letters, 2008, 8, 3488-3492.

[28] Ma, Wanli; Swisher, Sarah L.; Ewers, Trevor; Engel, Jesse; Ferry, Vivian E.; Atwater, Harry A.; Alivisatos, A. Paul. "Photovoltaic Performance of Ultrasmall PbSe Quantum Dots", ACS Nano, 2011, 5, 8140-8147.

[29] Clifford, Jason P.; Johnston, Keith W.; Levina, Larissa; Sargent, Edward H. "Schottky Barriers to Colloidal Quantum Dot Films", Applied Physics Letters, 2007, 91, 253117.

[30] Klem, Ethan J. D.; MacNeil, Dean D.; Cyr, Paul W.; Levina, Larissa; Sargent, Edward H. "Efficient Solution-Processed Infrared Photovoltaic Cells: Planarized All-Inorganic Bulk Heterojunction Devices via Inter-Quantum-Dot Bridging During Growth from Solution", Applied Physics Letters, 2007, 90, 183113.

[31] Zaban, A.; Mićić, O. I.; Gregg, B. A.; Nozik, A. J. "Photosensitization of Nanoporous TiO2 Electrodes with InP Quantum Dots", Langmuir, 1998, 14, 3153-3156.

[32] Robel, István; Subramanian, Vaidyanathan; Kuno, Masaru; Kamat, Prashant V.

"Quantum Dot Solar Cells. Harvesting Light Energy with CdSe Nanocrystals Molecularly Linked to Mesoscopic TiO_2 Films", Journal of the American Chemical Society, 2006, 128, 2385-2393.

[33] Jiao, Shuang; Du, Jun; Du, Zhonglin; Long, Donghui; Jiang, Wuyou; Pan, Zhenxiao; Li, Yan; Zhong, Xinhua. "Nitrogen-Doped Mesoporous Carbons as Counter Electrodes in Quantum Dot Sensitized Solar Cells with a Conversion Efficiency Exceeding 12%", The Journal of Physical Chemistry Letters, 2017, 8, 559-564.

[34] Shen, Q.; Kobayashi, J.; Diguna, L. J.; Toyoda, T. "Effect of ZnS Coating on the Photovoltaic Properties of CdSe Quantum Dot-Sensitized Solar Cells", Journal of Applied Physics, 2008, 103, 084304.

[35] Leschkies, Kurtis S.; Beatty, Timothy J.; Kang, Moon Sung; Norris, David J.; Aydil, Eray S. "Solar Cells Based on Junctions between Colloidal PbSe Nanocrystals and Thin ZnO Films", ACS Nano, 2009, 3, 3638-3648.

[36] Luther, J. M.; Gao, J. B.; Lloyd, M. T.; Semonin, O. E.; Beard, M. C.; Nozik, A. J. "Stability Assessment on a 3% Bilayer PbS/ZnO Quantum Dot Heterojunction Solar Cell", Advanced Materials, 2010, 22, 3704-3707.

[37] Pattantyus-Abraham, Andras G.; Kramer, Illan J.; Barkhouse, Aaron R.; Wang, Xihua; Konstantatos, Gerasimos; Debnath, Ratan; Levina, Larissa; Raabe, Ines; Nazeeruddin, Mohammad K.; Graetzel, Michael; Sargent, Edward H. "Depleted-Heterojunction Colloidal Quantum Dot Solar Cells", ACS Nano, 2010, 4, 3374-3380.

[38] Chang, Jin; Kuga, Yuki; Mora-Sero, Ivan; Toyoda, Taro; Ogomi, Yuhei; Hayase, Shuzi; Bisquert, Juan; Shen, Qing. "High Reduction of Interfacial Charge Recombination in Colloidal Quantum Dot Solar Cells by Metal Oxide Surface Passivation", Nanoscale, 2015, 7, 5446-5456.

[39] Jean, Joel; Chang, Sehoon; Brown, Patrick R.; Cheng, Jayce J.; Rekemeyer, Paul H.; Bawendi, Moungi G.; Gradečak, Silvija; Bulović, Vladimir. "ZnO Nanowire Arrays for Enhanced Photocurrent in PbS Quantum Dot Solar Cells", Advanced Materials, 2013, 25, 2790-2796.

[40] Tang, Jiang; Kemp, Kyle W.; Hoogland, Sjoerd; Jeong, Kwang S.; Liu, Huan; Levina, Larissa; Furukawa, Melissa; Wang, Xihua; Debnath, Ratan; Cha, Dongkyu; Chou, Kang Wei; Fischer, Armin; Amassian, Aram; Asbury, John B.; Sargent, Edward H. "Colloidal-Quantum-Dot Photovoltaics Using Atomic-Ligand Passivation", Nature Materials, 2011, 10, 765-771.

[41] Chuang, Chia-Hao M.; Brown, Patrick R.; Bulović, Vladimir; Bawendi, Moungi G. "Improved Performance and Stability in Quantum Dot Solar Cells through Band Alignment Engineering", Nature Materials, 2014, 13, 796-801.

[42] Liu, Mengxia; de Arquer, F. Pelayo García; Li, Yiying; Lan, Xinzheng; Kim, Gi-Hwan; Voznyy, Oleksandr; Jagadamma, Lethy Krishnan; Abbas, Abdullah Saud; Hoogland, Sjoerd; Lu, Zhenghong; Kim, Jin Young; Amassian, Aram; Sargent, Edward H. "Double-Sided Junctions Enable High-Performance Colloidal-Quantum-Dot Photovoltaics", Advanced Materials, 2016, n/a-n/a.

[43] Lan, Xinzheng; Voznyy, Oleksandr; García de Arquer, F. Pelayo; Liu, Mengxia; Xu, Jixian; Proppe, Andrew H.; Walters, Grant; Fan, Fengjia; Tan, Hairen; Liu, Min; Yang, Zhenyu; Hoogland, Sjoerd; Sargent, Edward H. "10.6% Certified Colloidal Quantum Dot Solar Cells via Solvent-Polarity-Engineered Halide Passivation", Nano Letters, 2016, 16, 4630-4634.

[44] Kim, Sungwoo; Noh, Jaehong; Choi, Hyekyoung; Ha, Heonseok; Song, Jung Hoon; Shim, Hyung Cheoul; Jang, Jihoon; Beard, Matthew C.; Jeong, Sohee. "One-Step Deposition of Photovoltaic Layers Using Iodide Terminated PbS Quantum Dots", The Journal of Physical Chemistry Letters, 2014, 5, 4002-4007.

[45] Kiani, Amirreza; Sutherland, Brandon R.; Kim, Younghoon; Ouellette, Olivier; Levina, Larissa; Walters, Grant; Dinh, Cao-Thang; Liu, Mengxia; Voznyy, Oleksandr; Lan, Xinzheng; Labelle, Andre J.; Ip, Alexander H.; Proppe, Andrew; Ahmed, Ghada H.; Mohammed, Omar F.; Hoogland, Sjoerd; Sargent, Edward H. "Single-Step Colloidal Quantum Dot Films for Infrared Solar Harvesting", Applied Physics Letters, 2016, 109, 183105.

[46] Choi, Hyekyoung; Lee, Jong-Gun; Mai, Xuan Dung; Beard, Matthew C.; Yoon, Sam S.; Jeong, Sohee. "Supersonically Spray-Coated Colloidal Quantum Dot

Ink Solar Cells", Scientific Reports, 2017, 7, 622.

[47] Mohamed, H. A. "Theoretical Study of the Efficiency of CdS/PbS Thin Film Solar Cells", Solar Energy, 2014, 108, 360-369.

[48] Mitzi, David B. "Templating and Structural Engineering in Organic-Inorganic Perovskites", Journal of the Chemical Society, Dalton Transactions, 2001, 1-12.

[49] Glazer, A. M. "Classification of Tilted Octahedra in Perovskites", Acta Crystallogr., Sect. B, 1972, 28, 3384-92.

[50] Nam-Gyu Park; Michael Grätzel; Miyasaka, Tsutomu. "Organic-Inorganic Halide Perovskite Photovoltaics″. 1 ed.; Springer International Publishing: 2016; p VIII, 366.

[51] Green, Martin A.; Ho-Baillie, Anita; Snaith, Henry J. "The Emergence of Perovskite Solar Cells", Nature Photonics, 2014, 8, 506-514.

[52] Søndenå, Rune; Ravindran, P.; Stølen, Svein; Grande, Tor; Hanfland, Michael. "Electronic structure and magnetic properties of cubic and hexagonal $SrMnO_3$", Physical Review B, 2006, 74, 144102.

[53] Docampo, Pablo; Bein, Thomas. "A Long-Term View on Perovskite Optoelectronics", Accounts of Chemical Research, 2016, 49, 339-346.

[54] Al-Dainy, G. A.; Bourdo, S. E.; Saini, V.; Berry, B. C.; Biris, A. S. "Hybrid Perovskite Photovoltaic Devices: Properties, Architecture, and Fabrication Methods", Energy Technology, 2017, 5, 373-401.

[55] Li, C. H.; Lu, X. G.; Ding, W. Z.; Feng, L. M.; Gao, Y. H.; Guo, Z. G. "Formability of ABX(3) (X = F, Cl, Br, I) Halide Perovskites", Acta Crystallographica Section B-Structural Science, 2008, 64, 702-707.

[56] Mitzi, David B. "Organic−Inorganic Perovskites Containing Trivalent Metal Halide Layers: The Templating Influence of the Organic Cation Layer", Inorganic Chemistry, 2000, 39, 6107-6113.

[57] McKinnon, Nicole K.; Reeves, David C.; Akabas, Myles H. "5-HT3 Receptor Ion Size Selectivity Is a Property of the Transmembrane Channel, Not the

Cytoplasmic Vestibule Portals", The Journal of General Physiology, 2011, 138, 453-466.

[58] Cohen, B. N.; Labarca, C.; Davidson, N.; Lester, H. A. "Mutations In M2 Alter the Selectivity of the Mouse Nicotinic Acetylcholine-Receptor for Organic and Alkali-Metal Cations", Journal of General Physiology, 1992, 100, 373-400.

[59] Umari, Paolo; Mosconi, Edoardo; De Angelis, Filippo. "Relativistic GW Calculations on $CH_3NH_3PbI_3$ and $CH_3NH_3SnI_3$ Perovskites for Solar Cell Applications", Scientific Reports, 2014, 4, 4467.

[60] Tan, Hairen; Jain, Ankit; Voznyy, Oleksandr; Lan, Xinzheng; García de Arquer, F. Pelayo; Fan, James Z.; Quintero-Bermudez, Rafael; Yuan, Mingjian; Zhang, Bo; Zhao, Yicheng; Fan, Fengjia; Li, Peicheng; Quan, Li Na; Zhao, Yongbiao; Lu, Zheng-Hong; Yang, Zhenyu; Hoogland, Sjoerd; Sargent, Edward H. "Efficient and Stable Solution-Processed Planar Perovskite Solar Cells via Contact Passivation", Science, 2017, DOI: 10.1126/science.aai9081.

[61] Mahmud, Md Arafat; Elumalai, Naveen Kumar; Upama, Mushfika Baishakhi; Wang, Dian; Chan, Kah Howe; Wright, Matthew; Xu, Cheng; Haque, Faiazul; Uddin, Ashraf. "Low Temperature Processed ZnO Thin Film as Electron Transport Layer for Efficient Perovskite Solar Cells", Solar Energy Materials and Solar Cells, 2017, 159, 251-264.

[62] Liu, Dianyi; Kelly, Timothy L. "Perovskite Solar Cells with a Planar Heterojunction Structure Prepared Using Room-Temperature Solution Processing Techniques", Nature Photonics, 2014, 8, 133-138.

[63] Son, Dae-Yong; Im, Jeong-Hyeok; Kim, Hui-Seon; Park, Nam-Gyu. "11% Efficient Perovskite Solar Cell Based on ZnO Nanorods: An Effective Charge Collection System", The Journal of Physical Chemistry C, 2014, 118, 16567-16573.

[64] You, Jingbi; Meng, Lei; Song, Tze-Bin; Guo, Tzung-Fang; Yang, Yang; Chang, Wei-Hsuan; Hong, Ziruo; Chen, Huajun; Zhou, Huanping; Chen, Qi; Liu, Yongsheng; De Marco, Nicholas; Yang, Yang. "Improved Air Stability of Perovskite Solar Cells via Solution-Processed Metal Oxide Transport Layers",

Nature Nanotechnology, 2016, 11, 75-81.

[65] Eperon, Giles E.; Stranks, Samuel D.; Menelaou, Christopher; Johnston, Michael B.; Herz, Laura M.; Snaith, Henry J. "Formamidinium Lead Trihalide: a Broadly Tunable Perovskite for Efficient Planar Heterojunction Solar Cells", Energy & Environmental Science, 2014, 7, 982-988.

[66] Stoumpos, Constantinos C.; Malliakas, Christos D.; Kanatzidis, Mercouri G. "Semiconducting Tin and Lead Iodide Perovskites with Organic Cations: Phase Transitions, High Mobilities, and Near-Infrared Photoluminescent Properties", Inorganic Chemistry, 2013, 52, 9019-9038.

[67] Zhou, Zhongmin; Pang, Shuping; Liu, Zhihong; Xu, Hongxia; Cui, Guanglei. "Interface Engineering for High-Performance Perovskite Hybrid Solar Cells", Journal of Materials Chemistry A, 2015, 3, 19205-19217.

[68] Yang, Shida; Fu, Weifei; Zhang, Zhongqiang; Chen, Hongzheng; Li, Chang-Zhi. "Recent Advances in Perovskite Solar Cells: Efficiency, Stability and Lead-Free Perovskite", Journal of Materials Chemistry A, 2017, 5, 11462-11482.

[69] Dürr, M.; Yasuda, A.; Nelles, G. "On the Origin of Increased Open Circuit Voltage of Dye-Sensitized Solar Cells Using 4-Tert-Butyl Pyridine as Additive to the Electrolyte", Applied Physics Letters, 2006, 89, 061110.

[70] Cappel, Ute B.; Smeigh, Amanda L.; Plogmaker, Stefan; Johansson, Erik M. J.; Rensmo, Håkan; Hammarström, Leif; Hagfeldt, Anders; Boschloo, Gerrit. "Characterization of the Interface Properties and Processes in Solid State Dye-Sensitized Solar Cells Employing a Perylene Sensitizer", The Journal of Physical Chemistry C, 2011, 115, 4345-4358.

[71] Snaith, Henry J.; Moule, Adam J.; Klein, Cédric; Meerholz, Klaus; Friend, Richard H.; Grätzel, Michael. "Efficiency Enhancements in Solid-State Hybrid Solar Cells via Reduced Charge Recombination and Increased Light Capture", Nano Letters, 2007, 7, 3372-3376.

[72] Zhang, Lijun; Liu, Tongfa; Liu, Linfeng; Hu, Min; Yang, Ying; Mei, Anyi; Han, Hongwei. "The Effect of Carbon Counter Electrodes on Fully Printable

Mesoscopic Perovskite Solar Cells", Journal of Materials Chemistry A, 2015, 3, 9165-9170.

[73] Mei, Anyi; Li, Xiong; Liu, Linfeng; Ku, Zhiliang; Liu, Tongfa; Rong, Yaoguang; Xu, Mi; Hu, Min; Chen, Jiangzhao; Yang, Ying; Grätzel, Michael; Han, Hongwei. "A Hole-Conductor–Free, Fully Printable Mesoscopic Perovskite Solar Cell with High Stability", Science, 2014, 345, 295-298.

[74] Zuo, Fan; Williams, Spencer T.; Liang, Po-Wei; Chueh, Chu-Chen; Liao, Chien-Yi; Jen, Alex K. Y. "Binary-Metal Perovskites Toward High-Performance Planar-Heterojunction Hybrid Solar Cells", Advanced Materials, 2014, 26, 6454-6460.

[75] Liu, Jiang; Wang, Gang; Song, Zhen; He, Xulin; Luo, Kun; Ye, Qinyan; Liao, Cheng; Mei, Jun. "$FAPb_{1-x}Sn_xI_3$ Mixed Metal Halide Perovskites with Improved Light Harvesting and Stability for Efficient Planar Heterojunction Solar Cells", Journal of Materials Chemistry A, 2017, 5, 9097-9106.

[76] Serrano-Lujan, Lucia; Espinosa, Nieves; Larsen-Olsen, Thue Trofod; Abad, Jose; Urbina, Antonio; Krebs, Frederik C. "Tin- and Lead-Based Perovskite Solar Cells under Scrutiny: An Environmental Perspective", Advanced Energy Materials, 2015, 5, 1501119.

[77] Savory, Christopher N.; Walsh, Aron; Scanlon, David O. "Can Pb-Free Halide Double Perovskites Support High-Efficiency Solar Cells?", ACS Energy Letters, 2016, 1, 949-955.

[78] Kim, Younghoon; Yang, Zhenyu; Jain, Ankit; Voznyy, Oleksandr; Kim, Gi-Hwan; Liu, Min; Quan, Li Na; García de Arquer, F. Pelayo; Comin, Riccardo; Fan, James Z.; Sargent, Edward H. "Pure Cubic-Phase Hybrid Iodobismuthates AgBi2I7 for Thin-Film Photovoltaics", Angewandte Chemie International Edition, 2016, 55, 9586-9590.

[79] Ishii, Hisao; Kinjo, Hiroumi; Sato, Tomoya; Machida, Shin-ichi; Nakayama, Yasuo. "Photoelectron Yield Spectroscopy for Organic Materials and Interfaces". In Electronic Processes in Organic Electronics: Bridging Nanostructure, Electronic States and Device Properties, Springer Japan: Tokyo, 2015, 131-155.

[80] Semonin, Octavi E.; Luther, Joseph M.; Choi, Sukgeun; Chen, Hsiang-Yu; Gao, Jianbo; Nozik, Arthur J.; Beard, Matthew C. "Peak External Photocurrent Quantum Efficiency Exceeding 100% via MEG in a Quantum Dot Solar Cell", Science, 2011, 334, 1530-1533.

[81] Graetzel, M.; Janssen, R. A. J.; Mitzi, D. B.; Sargent, E. H. "Materials Interface Engineering for Solution-Processed Photovoltaics", Nature, 2012, 488, 304-312.

[82] Talapin, D. V.; Murray, C. B. "PbSe Nanocrystal Solids for n- and p-Channel Thin Film Field-Effect Transistors", Science, 2005, 310, 86-89.

[83] Sargent, Edward H. "Infrared Photovoltaics Made by Solution Processing", Nature Photonics, 2009, 3, 325-331.

[84] Kamat, Prashant V. "Quantum Dot Solar Cells. Semiconductor Nanocrystals as Light Harvesters", The Journal of Physical Chemistry C, 2008, 112, 18737-18753.

[85] Caruge, J. M.; Halpert, J. E.; Wood, V.; Bulovic, V.; Bawendi, M. G. "Colloidal Quantum-Dot Light-Emitting Diodes with Metal-Oxide Charge Transport Layers", Nature Photonics, 2008, 2, 247-250.

[86] Woo, J. Y.; Kim, K.; Jeong, S.; Han, C. S. "Enhanced Photoluminance of Layered Quantum Dot-Phosphor Nanocomposites as Converting Materials for Light Emitting Diodes", Journal of Physical Chemistry C, 2011, 115, 20945-20952.

[87] Luther, Joseph M.; Law, Matt; Song, Qing; Perkins, Craig L.; Beard, Matthew C.; Nozik, Arthur J. "Structural, Optical and Electrical Properties of Self-Assembled Films of PbSe Nanocrystals Treated with 1,2-Ethanedithiol", ACS Nano, 2008, 2, 271-280.

[88] Sukhovatkin, Vlad; Hinds, Sean; Brzozowski, Lukasz; Sargent, Edward H. "Colloidal Quantum-Dot Photodetectors Exploiting Multiexciton Generation", Science, 2009, 324, 1542-1544.

[89] Zhang, J.; Toentino, J.; Smith, E. R.; Zhang, J. B.; Beard, M. C.; Nozik, A. J.; Law, M.; Johnson, J. C. "Carrier Transport in PbS and PbSe QD Films Measured

by Photoluminescence Quenching", Journal of Physical Chemistry C, 2014, 118, 16228-16235.

[90] Fan, H. Y.; Yang, K.; Boye, D. M.; Sigmon, T.; Malloy, K. J.; Xu, H. F.; Lopez, G. P.; Brinker, C. J. "Self-Assembly of Ordered, Robust, Three-Dimensional Gold Nanocrystal/Silica Arrays", Science, 2004, 304, 567-571.

[91] Deka, Sasanka; Quarta, Alessandra; Lupo, Maria Grazia; Falqui, Andrea; Boninelli, Silmona; Giannini, Cinzia; Morello, Giovanni; De Giorgi, Milena; Lanzani, Guglielmo; Spinella, Corrado; Cingolani, Roberto; Pellegrino, Teresa; Manna, Liberato. "CdSe/CdS/ZnS Double Shell Nanorods with High Photoluminescence Efficiency and Their Exploitation As Biolabeling Probes", Journal of the American Chemical Society, 2009, 131, 2948-2958.

[92] Zaman, M. B.; Baral, T. N.; Zhang, J. B.; Whitfield, D.; Yu, K. "Single-Domain Antibody Functionalized CdSe/ZnS Quantum Dots for Cellular Imaging of Cancer Cells", Journal of Physical Chemistry C, 2009, 113, 496-499.

[93] Pavesi, L.; Dal Negro, L.; Mazzoleni, C.; Franzo, G.; Priolo, F. "Optical Gain in Silicon Nanocrystals", Nature, 2000, 408, 440-444.

[94] Klimov, V. I.; Mikhailovsky, A. A.; Xu, S.; Malko, A.; Hollingsworth, J. A.; Leatherdale, C. A.; Eisler, H. J.; Bawendi, M. G. "Optical Gain and Stimulated Emission in Nanocrystal Quantum Dots", Science, 2000, 290, 314-317.

[95] Papagiannouli, I.; Maratou, E.; Koutselas, I.; Couris, S. "Synthesis and Characterization of the Nonlinear Optical Properties of Novel Hybrid Organic-Inorganic Semiconductor Lead Iodide Quantum Wells and Dots", Journal of Physical Chemistry C, 2014, 118, 2766-2775.

[96] Sargent, E. H. "Colloidal Quantum Dot Solar Cells", Nature Photonics, 2012, 6, 133-135.

[97] Liu, F.; Zhu, J.; Wei, J. F.; Li, Y.; Hu, L. H.; Huang, Y.; Takuya, O.; Shen, Q.; Toyoda, T.; Zhang, B.; Yao, J. X.; Dai, S. Y. "Ex Situ CdSe Quantum Dot-Sensitized Solar Cells Employing Inorganic Ligand Exchange To Boost Efficiency", Journal of Physical Chemistry C, 2014, 118, 214-222.

[98] Zhang, Y. H.; Zhu, J.; Yu, X. C.; Wei, J. F.; Hu, L. H.; Dai, S. Y. "The Optical and Electrochemical Properties of CdS/CdSe Co-Sensitized TiO_2 Solar Cells Prepared by Successive Ionic Layer Adsorption and Reaction Processes", Solar Energy, 2012, 86, 964-971.

[99] Nozik, Arthur J. "Nanoscience and Nanostructures for Photovoltaics and Solar Fuels", Nano Letters, 2010, 10, 2735-2741.

[100] Hetsch, Frederik; Xu, Xueqing; Wang, Hongkang; Kershaw, Stephen V.; Rogach, Andrey L. "Semiconductor Nanocrystal Quantum Dots as Solar Cell Components and Photosensitizers: Material, Charge Transfer, and Separation Aspects of Some Device Topologies", The Journal of Physical Chemistry Letters, 2011, 2, 1879-1887.

[101] Davis, Nathaniel J. L. K.; Bohm, Marcus L.; Tabachnyk, Maxim; Wisnivesky-Rocca-Rivarola, Florencia; Jellicoe, Tom C.; Ducati, Caterina; Ehrler, Bruno; Greenham, Neil C. "Multiple-Exciton Generation in Lead Selenide Nanorod Solar Cells with External Quantum Efficiencies Exceeding 120%", Nature Communications, 2015, 6, 8259.

[102] Isborn, Christine M.; Kilina, Svetlana V.; Li, Xiaosong; Prezhdo, Oleg V. "Generation of Multiple Excitons in PbSe and CdSe Quantum Dots by Direct Photoexcitation: First-Principles Calculations on Small PbSe and CdSe Clusters", The Journal of Physical Chemistry C, 2008, 112, 18291-18294.

[103] Hanna, M. C.; Nozik, A. J. "Solar Conversion Efficiency of Photovoltaic and Photoelectrolysis Cells with Carrier Multiplication Absorbers", Journal of Applied Physics, 2006, 100, 074510.

[104] Liu, Mengxia; de Arquer, F. Pelayo García; Li, Yiying; Lan, Xinzheng; Kim, Gi-Hwan; Voznyy, Oleksandr; Jagadamma, Lethy Krishnan; Abbas, Abdullah Saud; Hoogland, Sjoerd; Lu, Zhenghong; Kim, Jin Young; Amassian, Aram; Sargent, Edward H. "Double-Sided Junctions Enable High-Performance Colloidal-Quantum-Dot Photovoltaics", Advanced Materials, 2016, 28, 4142-4148.

[105] Du, Jun; Du, Zhonglin; Hu, Jin-Song; Pan, Zhenxiao; Shen, Qing; Sun, Jiankun; Long, Donghui; Dong, Hui; Sun, Litao; Zhong, Xinhua; Wan, Li-Jun. "Zn–Cu–

In–Se Quantum Dot Solar Cells with a Certified Power Conversion Efficiency of 11.6%", Journal of the American Chemical Society, 2016, 138, 4201-4209.

[106] Pietryga, Jeffrey M.; Schaller, Richard D.; Werder, Donald; Stewart, Michael H.; Klimov, Victor I.; Hollingsworth, Jennifer A. "Pushing the Band Gap Envelope: Mid-Infrared Emitting Colloidal PbSe Quantum Dots", Journal of the American Chemical Society, 2004, 126, 11752-11753.

[107] Romero, Hugo E.; Drndic, Marija. "Coulomb Blockade and Hopping Conduction in PbSe Quantum Dots", Physical Review Letters, 2005, 95, 156801.

[108] Woo, Ju Young; Ko, Jae-Hyeon; Song, Jung Hoon; Kim, Kyungnam; Choi, Hyekyoung; Kim, Yong-Hyun; Lee, Doh C.; Jeong, Sohee. "Ultrastable PbSe Nanocrystal Quantum Dots via in Situ Formation of Atomically Thin Halide Adlayers on PbSe(100)", Journal of the American Chemical Society, 2014, 136, 8883-8886.

[109] Choi, Hyekyoung; Song, Jung Hoon; Jang, Jihoon; Mai, Xuan Dung; Kim, Sungwoo; Jeong, Sohee. "High Performance of PbSe/PbS core/shell Quantum Dot Heterojunction Solar Cells: Short Circuit Current Enhancement Without the Loss of Open Circuit Voltage by Shell Thickness Control", Nanoscale, 2015, 7, 17473-17481.

[110] Padilha, Lazaro A.; Stewart, John T.; Sandberg, Richard L.; Bae, Wan Ki; Koh, Weon-Kyu; Pietryga, Jeffrey M.; Klimov, Victor I. "Carrier Multiplication in Semiconductor Nanocrystals: Influence of Size, Shape, and Composition", Accounts of Chemical Research, 2013, 46, 1261-1269.

[111] Moreels, Iwan; Fritzinger, Bernd; Martins, José C.; Hens, Zeger. "Surface Chemistry of Colloidal PbSe Nanocrystals", Journal of the American Chemical Society, 2008, 130, 15081-15086.

[112] Zhang, Zhong; Liu, Chao; Zhao, Xiujian. "Utilizing Sn-precursor to Promote the Nucleation of PbSe Quantum Dots with In Situ Halide Passivation", The Journal of Physical Chemistry C, 2015, 119, 5626-5632.

[113] Asil, Demet; Walker, Brian J.; Ehrler, Bruno; Vaynzof, Yana; Sepe, Alessandro;

Bayliss, Sam; Sadhanala, Aditya; Chow, Philip C. Y.; Hopkinson, Paul E.; Steiner, Ullrich; Greenham, Neil C.; Friend, Richard H. "Role of PbSe Structural Stabilization in Photovoltaic Cells", Advanced Functional Materials, 2015, 25, 928-935.

[114] Crisp, Ryan W.; Kroupa, Daniel M.; Marshall, Ashley R.; Miller, Elisa M.; Zhang, Jianbing; Beard, Matthew C.; Luther, Joseph M. "Metal Halide Solid-State Surface Treatment for High Efficiency PbS and PbSe QD Solar Cells", Scientific Reports, 2015, 5, 9945.

[115] Kim, Sungwoo; Marshall, Ashley R.; Kroupa, Daniel M.; Miller, Elisa M.; Luther, Joseph M.; Jeong, Sohee; Beard, Matthew C. "Air-Stable and Efficient PbSe Quantum-Dot Solar Cells Based upon ZnSe to PbSe Cation-Exchanged Quantum Dots", ACS Nano, 2015, 9, 8157-8164.

[116] Zhang, Jianbing; Gao, Jianbo; Church, Carena P.; Miller, Elisa M.; Luther, Joseph M.; Klimov, Victor I.; Beard, Matthew C. "PbSe Quantum Dot Solar Cells with More than 6% Efficiency Fabricated in Ambient Atmosphere", Nano Letters, 2014, 14, 6010-6015.

[117] Chang, Jin; Kuga, Yuki; Mora-Sero, Ivan; Toyoda, Taro; Ogomi, Yuhei; Hayase, Shuzi; Bisquert, Juan; Shen, Qing. "High Reduction of Interfacial Charge Recombination in Colloidal Quantum Dot Solar Cells by Metal Oxide Surface Passivation", Nanoscale, 2015, 7, 5446-5456.

[118] Dai, Quanqin; Wang, Yingnan; Li, Xinbi; Zhang, Yu; Pellegrino, Donald J.; Zhao, Muxun; Zou, Bo; Seo, JaeTae; Wang, Yiding; Yu, William W. "Size-Dependent Composition and Molar Extinction Coefficient of PbSe Semiconductor Nanocrystals", ACS Nano, 2009, 3, 1518-1524.

[119] Oh, Soong Ju; Wang, Zhuqing; Berry, Nathaniel E.; Choi, Ji-Hyuk; Zhao, Tianshuo; Gaulding, E. Ashley; Paik, Taejong; Lai, Yuming; Murray, Christopher B.; Kagan, Cherie R. "Engineering Charge Injection and Charge Transport for High Performance PbSe Nanocrystal Thin Film Devices and Circuits", Nano Letters, 2014, 14, 6210-6216.

[120] Sarasqueta, Galileo; Choudhury, Kaushik Roy; So, Franky. "Effect of Solvent

Treatment on Solution-Processed Colloidal PbSe Nanocrystal Infrared Photodetectors", Chemistry of Materials, 2010, 22, 3496-3501.

[121] Kuo, Chih-Yin; Su, Ming-Shin; Ku, Ching-Shun; Wang, Shu-Min; Lee, Hsin-Yi; Wei, Kung-Hwa. "Ligands affect the crystal structure and photovoltaic performance of thin films of PbSe quantum dots", Journal of Materials Chemistry, 2011, 21, 11605-11612.

[122] Luther, Joseph M.; Law, Matt; Song, Qing; Perkins, Craig L.; Beard, Matthew C.; Nozik, Arthur J. "Structural, Optical, and Electrical Properties of Self-Assembled Films of PbSe Nanocrystals Treated with 1,2-Ethanedithiol", ACS Nano, 2008, 2, 271-280.

[123] Brown, Patrick R.; Kim, Donghun; Lunt, Richard R.; Zhao, Ni; Bawendi, Moungi G.; Grossman, Jeffrey C.; Bulović, Vladimir. "Energy Level Modification in Lead Sulfide Quantum Dot Thin Films through Ligand Exchange", ACS Nano, 2014, 8, 5863-5872.

[124] Hines, Douglas A.; Kamat, Prashant V. "Quantum Dot Surface Chemistry: Ligand Effects and Electron Transfer Reactions", The Journal of Physical Chemistry C, 2013, 117, 14418-14426.

[125] Colbert, Adam E.; Wu, Wenbi; Janke, Eric M.; Ma, Fei; Ginger, David S. "Effects of Ligands on Charge Generation and Recombination in Hybrid Polymer/Quantum Dot Solar Cells", The Journal of Physical Chemistry C, 2015, 119, 24733-24739.

[126] Gao, Jianbo; Johnson, Justin C. "Charge Trapping in Bright and Dark States of Coupled PbS Quantum Dot Films", ACS Nano, 2012, 6, 3292-3303.

[127] Shen, Qing; Ogomi, Yuhei; Park, Byung-wook; Inoue, Takafumi; Pandey, Shyam S.; Miyamoto, Akari; Fujita, Shinsuke; Katayama, Kenji; Toyoda, Taro; Hayase, Shuzi. "Multiple Electron Injection Dynamics in Linearly-Linked Two Dye Co-Sensitized Nanocrystalline Metal Oxide Electrodes for Dye-Sensitized Solar Cells", Physical Chemistry Chemical Physics, 2012, 14, 4605-4613.

[128] Ono, Masashi; Nishihara, Taishi; Ihara, Toshiyuki; Kikuchi, Makoto; Tanaka,

Atsushi; Suzuki, Masayuki; Kanemitsu, Yoshihiko. "Impact of Surface Ligands on the Photocurrent Enhancement Due to Multiple Exciton Generation in Close-Packed Nanocrystal Thin Films", Chemical Science, 2014, 5, 2696-2701.

[129] Gao, Jianbo; Zhang, Jianbing; van de Lagemaat, Jao; Johnson, Justin C.; Beard, Matthew C. "Charge Generation in PbS Quantum Dot Solar Cells Characterized by Temperature-Dependent Steady-State Photoluminescence", ACS Nano, 2014, 8, 12814-12825.

[130] Liu, Yao; Gibbs, Markelle; Puthussery, James; Gaik, Steven; Ihly, Rachelle; Hillhouse, Hugh W.; Law, Matt. "Dependence of Carrier Mobility on Nanocrystal Size and Ligand Length in PbSe Nanocrystal Solids", Nano Letters, 2010, 10, 1960-1969.

[131] Milliron, Delia J. "Quantum Dot Solar Cells: The Surface Plays a Core Role", Nature Materials, 2014, 13, 772-773.

[132] Leschkies, Kurtis S.; Kang, Moon Sung; Aydil, Eray S.; Norris, David J. "Influence of Atmospheric Gases on the Electrical Properties of PbSe Quantum-Dot Films", The Journal of Physical Chemistry C, 2010, 114, 9988-9996.

[133] Zhitomirsky, David; Furukawa, Melissa; Tang, Jiang; Stadler, Philipp; Hoogland, Sjoerd; Voznyy, Oleksandr; Liu, Huan; Sargent, Edward H. "N-Type Colloidal-Quantum-Dot Solids for Photovoltaics", Advanced Materials, 2012, 24, 6181-6185.

[134] Zhang, Zhilong; Yang, Jianfeng; Wen, Xiaoming; Yuan, Lin; Shrestha, Santosh; Stride, John A.; Conibeer, Gavin J.; Patterson, Robert J.; Huang, Shujuan. "Effect of Halide Treatments on PbSe Quantum Dot Thin Films: Stability, Hot Carrier Lifetime, and Application to Photovoltaics", The Journal of Physical Chemistry C, 2015, 119, 24149-24155.

[135] Zaban, Arie; Greenshtein, Miri; Bisquert, Juan. "Determination of the Electron Lifetime in Nanocrystalline Dye Solar Cells by Open-Circuit Voltage Decay Measurements", ChemPhysChem, 2003, 4, 859-864.

[136] Kim, Mee Rahn; Ma, Dongling. "Quantum-Dot-Based Solar Cells: Recent

Advances, Strategies, and Challenges", The Journal of Physical Chemistry Letters, 2015, 6, 85-99.

[137] Milliron, Delia J. "Quantum Dot Solar Cells: The Surface Plays a Core Role", Nature Materials, 2014, 13, 772-773.

[138] Crisp, Ryan W.; Kroupa, Daniel M.; Marshall, Ashley R.; Miller, Elisa M.; Zhang, Jianbing; Beard, Matthew C.; Luther, Joseph M. "Metal Halide Solid-State Surface Treatment for High Efficiency PbS and PbSe QD Solar Cells", Sci. Rep., 2015, 5, 9945.

[139] Marshall, Ashley R.; Young, Matthew R.; Nozik, Arthur J.; Beard, Matthew C.; Luther, Joseph M. "Exploration of Metal Chloride Uptake for Improved Performance Characteristics of PbSe Quantum Dot Solar Cells", The Journal of Physical Chemistry Letters, 2015, 6, 2892-2899.

[140] Cao, Yiming; Stavrinadis, Alexandros; Lasanta, Tania; So, David; Konstantatos, Gerasimos. "The role of surface passivation for efficient and photostable PbS quantum dot solar cells", Nature Energy, 2016, 1, 16035.

[141] King, Laurie A.; Parkinson, B. A. "Photosensitization of ZnO Crystals with Iodide-Capped PbSe Quantum Dots", The Journal of Physical Chemistry Letters, 2016, 7, 2844-2848.

[142] Liu, H.; Tang, J.; Kramer, I. J.; Debnath, R.; Koleilat, G. I.; Wang, X. H.; Fisher, A.; Li, R.; Brzozowski, L.; Levina, L.; Sargent, E. H. "Electron Acceptor Materials Engineering in Colloidal Quantum Dot Solar Cells", Advanced Materials, 2011, 23, 3832.

[143] Kim, Gi-Hwan; García de Arquer, F. Pelayo; Yoon, Yung Jin; Lan, Xinzheng; Liu, Mengxia; Voznyy, Oleksandr; Yang, Zhenyu; Fan, Fengjia; Ip, Alexander H.; Kanjanaboos, Pongsakorn; Hoogland, Sjoerd; Kim, Jin Young; Sargent, Edward H. "High-Efficiency Colloidal Quantum Dot Photovoltaics via Robust Self-Assembled Monolayers", Nano Letters, 2015, 15, 7691-7696.

[144] Yuan, Mingjian; Voznyy, Oleksandr; Zhitomirsky, David; Kanjanaboos, Pongsakorn; Sargent, Edward H. "Synergistic Doping of Fullerene Electron

Transport Layer and Colloidal Quantum Dot Solids Enhances Solar Cell Performance", Advanced Materials, 2015, 27, 917-921.

[145] Azmi, Randi; Oh, Seung-Hwan; Jang, Sung-Yeon. "High-Efficiency Colloidal Quantum Dot Photovoltaic Devices Using Chemically Modified Heterojunctions", ACS Energy Letters, 2016, 1, 100-106.

[146] Hu, Long; Li, Deng-Bing; Gao, Liang; Tan, Hua; Chen, Chao; Li, Kanghua; Li, Min; Han, Jun-Bo; Song, Haisheng; Liu, Huan; Tang, Jiang. "Graphene Doping Improved Device Performance of ZnMgO/PbS Colloidal Quantum Dot Photovoltaics", Advanced Functional Materials, 2016, 26, 1899-1907.

[147] Kemp, Kyle W.; Labelle, Andre J.; Thon, Susanna M.; Ip, Alexander H.; Kramer, Illan J.; Hoogland, Sjoerd; Sargent, Edward H. "Interface Recombination in Depleted Heterojunction Photovoltaics Based on Colloidal Quantum Dots", Advanced Energy Materials, 2013, 3, 917-922.

[148] Brown, Patrick R.; Lunt, Richard R.; Zhao, Ni; Osedach, Timothy P.; Wanger, Darcy D.; Chang, Liang-Yi; Bawendi, Moungi G.; Bulović, Vladimir. "Improved Current Extraction from ZnO/PbS Quantum Dot Heterojunction Photovoltaics Using a MoO_3 Interfacial Layer", Nano Letters, 2011, 11, 2955-2961.

[149] Ko, Dong-Kyun; Brown, Patrick R.; Bawendi, Moungi G.; Bulović, Vladimir. "p-i-n Heterojunction Solar Cells with a Colloidal Quantum-Dot Absorber Layer", Advanced Materials, 2014, 26, 4845-4850.

[150] Jin, Zhiwen; Yuan, Mingjian; Li, Hui; Yang, Hui; Zhou, Qing; Liu, Huibiao; Lan, Xinzheng; Liu, Mengxia; Wang, Jizheng; Sargent, Edward H.; Li, Yuliang. "Graphdiyne: An Efficient Hole Transporter for Stable High-Performance Colloidal Quantum Dot Solar Cells", Advanced Functional Materials, 2016, 26, 5284-5289.

[151] Neo, Darren C. J.; Zhang, Nanlin; Tazawa, Yujiro; Jiang, Haibo; Hughes, Gareth M.; Grovenor, Chris R. M.; Assender, Hazel E.; Watt, Andrew A. R. "Poly(3-hexylthiophene-2,5-diyl) as a Hole Transport Layer for Colloidal Quantum Dot Solar Cells", ACS Applied Materials & Interfaces, 2016, 8, 12101-12108.

[152] Zhang, Xiaoliang; Justo, Yolanda; Maes, Jorick; Walravens, Willem; Zhang, Jindan; Liu, Jianhua; Hens, Zeger; Johansson, Erik M. J. "Slow Recombination in Quantum Dot Solid Solar Cell Using p-i-n Architecture with Organic p-Type Hole Transport Material", Journal of Materials Chemistry A, 2015, 3, 20579-20585.

[153] Irfan; Ding, Huanjun; Gao, Yongli; Small, Cephas; Kim, Do Young; Subbiah, Jegadesan; So, Franky. "Energy Level Evolution of Air and Oxygen Exposed Molybdenum Trioxide Films", Applied Physics Letters, 2010, 96, 243307.

[154] Miller, Elisa M.; Kroupa, Daniel M.; Zhang, Jianbing; Schulz, Philip; Marshall, Ashley R.; Kahn, Antoine; Lany, Stephan; Luther, Joseph M.; Beard, Matthew C.; Perkins, Craig L.; van de Lagemaat, Jao. "Revisiting the Valence and Conduction Band Size Dependence of PbS Quantum Dot Thin Films", ACS Nano, 2016, 10, 3302-3311.

[155] Kim, Sungwoo; Im, Sang Hyuk; Kang, Meejae; Heo, Jin Hyuck; Seok, Sang Il; Kim, Sang-Wook; Mora-Sero, Ivan; Bisquert, Juan. "Air-Stable and Efficient Inorganic-Organic Heterojunction Solar Cells Using PbS Colloidal Quantum Dots Co-Capped by 1-Dodecanethiol and Oleic Acid", Physical Chemistry Chemical Physics, 2012, 14, 14999-15002.

[156] Jumabekov, Askhat N.; Siegler, Timothy D.; Cordes, Niklas; Medina, Dana D.; Böhm, Daniel; Garbus, Pelle; Meroni, Simone; Peter, Laurence M.; Bein, Thomas. "Comparison of Solid-State Quantum-Dot-Sensitized Solar Cells with ex Situ and in Situ Grown PbS Quantum Dots", The Journal of Physical Chemistry C, 2014, 118, 25853-25862.

[157] Lee, HyoJoong; Leventis, Henry C.; Moon, Soo-Jin; Chen, Peter; Ito, Seigo; Haque, Saif A.; Torres, Tomas; Nüesch, Frank; Geiger, Thomas; Zakeeruddin, Shaik M.; Grätzel, Michael; Nazeeruddin, Md Khaja. "PbS and CdS Quantum Dot-Sensitized Solid-State Solar Cells: “Old Concepts, New Results”", Advanced Functional Materials, 2009, 19, 2735-2742.

[158] Cardona, Claudia M.; Li, Wei; Kaifer, Angel E.; Stockdale, David; Bazan, Guillermo C. "Electrochemical Considerations for Determining Absolute

Frontier Orbital Energy Levels of Conjugated Polymers for Solar Cell Applications", Advanced Materials, 2011, 23, 2367-2371.

[159] Wu, Guohua; Kaneko, Ryuji; Islam, Ashraful; Zhang, Yaohong; Sugawa, Kosuke; Han, Liyuan; Shen, Qing; Bedja, Idriss; Gupta, Ravindra Kumar; Otsuki, Joe. "Thiocyanate-Free Asymmetric Ruthenium(II) Dye Sensitizers Containing Azole Chromophores with Near-IR Light-Harvesting Capacity", Journal of Power Sources, 2016, 331, 100-111.

[160] Wu, Guohua; Kaneko, Ryuji; Zhang, Yaohong; Shinozaki, Yoshinao; Sugawa, Kosuke; Islam, Ashraful; Han, Liyuan; Bedja, Idriss; Gupta, Ravindra Kumar; Shen, Qing; Otsuki, Joe. "Neutral and Anionic Tetrazole-Based Ligands in Designing Novel Ruthenium Dyes for Dye-Sensitized Solar Cells", Journal of Power Sources, 2016, 307, 416-425.

[161] Wang, Haibin; Kubo, Takaya; Nakazaki, Jotaro; Kinoshita, Takumi; Segawa, Hiroshi. "PbS-Quantum-Dot-Based Heterojunction Solar Cells Utilizing ZnO Nanowires for High External Quantum Efficiency in the Near-Infrared Region", The Journal of Physical Chemistry Letters, 2013, 4, 2455-2460.

[162] Jasieniak, Jacek; Califano, Marco; Watkins, Scott E. "Size-Dependent Valence and Conduction Band-Edge Energies of Semiconductor Nanocrystals", ACS Nano, 2011, 5, 5888-5902.

[163] Brauer, Jan C.; Lee, Yong Hui; Nazeeruddin, Mohammad Khaja; Banerji, Natalie. "Charge Transfer Dynamics from Organometal Halide Perovskite to Polymeric Hole Transport Materials in Hybrid Solar Cells", The Journal of Physical Chemistry Letters, 2015, 6, 3675-3681.

[164] Zhang, Fei; Zhao, Xiaoming; Yi, Chenyi; Bi, Dongqin; Bi, Xiangdong; Wei, Peng; Liu, Xicheng; Wang, Shirong; Li, Xianggao; Zakeeruddin, Shaik Mohammed; Grätzel, Michael. "Dopant-Free Star-Shaped Hole-Transport Materials for Efficient and Stable Perovskite Solar Cells", Dyes Pigments, 2017, 136, 273-277.

[165] Zhang, Yaohong; Ding, Chao; Wu, Guohua; Nakazawa, Naoki; Chang, Jin; Ogomi, Yuhei; Toyoda, Taro; Hayase, Shuzi; Katayama, Kenji; Shen, Qing. "Air

Stable PbSe Colloidal Quantum Dot Heterojunction Solar Cells: Ligand-Dependent Exciton Dissociation, Recombination, Photovoltaic Property, and Stability", The Journal of Physical Chemistry C, 2016, 120, 28509-28518.

[166] Bisquert, Juan; Fabregat-Santiago, Francisco; Mora-Seró, Iván; Garcia-Belmonte, Germà; Giménez, Sixto. "Electron Lifetime in Dye-Sensitized Solar Cells: Theory and Interpretation of Measurements", The Journal of Physical Chemistry C, 2009, 113, 17278-17290.

[167] Wang, Haibin; Gonzalez-Pedro, Victoria; Kubo, Takaya; Fabregat-Santiago, Francisco; Bisquert, Juan; Sanehira, Yoshitaka; Nakazaki, Jotaro; Segawa, Hiroshi. "Enhanced Carrier Transport Distance in Colloidal PbS Quantum-Dot-Based Solar Cells Using ZnO Nanowires", The Journal of Physical Chemistry C, 2015, 119, 27265-27274.

[168] Hodes, Gary. "Perovskite-Based Solar Cells", Science, 2013, 342, 317-318.

[169] Lee, Michael M.; Teuscher, Joël; Miyasaka, Tsutomu; Murakami, Takurou N.; Snaith, Henry J. "Efficient Hybrid Solar Cells Based on Meso-Superstructured Organometal Halide Perovskites", Science, 2012, 338, 643-647.

[170] Liu, Mingzhen; Johnston, Michael B.; Snaith, Henry J. "Efficient Planar Heterojunction Perovskite Solar Cells by Vapour Deposition", Nature, 2013, 501, 395-398.

[171] Park, Nam-Gyu. "Organometal Perovskite Light Absorbers Toward a 20% Efficiency Low-Cost Solid-State Mesoscopic Solar Cell", The Journal of Physical Chemistry Letters, 2013, 4, 2423-2429.

[172] Bi, Dongqin; Tress, Wolfgang; Dar, M. Ibrahim; Gao, Peng; Luo, Jingshan; Renevier, Clémentine; Schenk, Kurt; Abate, Antonio; Giordano, Fabrizio; Correa Baena, Juan-Pablo; Decoppet, Jean-David; Zakeeruddin, Shaik Mohammed; Nazeeruddin, Mohammad Khaja; Grätzel, Michael; Hagfeldt, Anders. "Efficient Luminescent Solar Cells Based on Tailored Mixed-Cation Perovskites", Science Advances, 2016, 2, e1501170.

[173] Paek, Sanghyun; Rub, Malik Abdul; Choi, Hyeju; Kosa, Samia A.; Alamry,

Khalid A.; Cho, Jin Woo; Gao, Peng; Ko, Jaejung; Asiri, Abdullah M.; Nazeeruddin, Mohammad Khaja. "A Dual-Functional Asymmetric Squaraine-Based Low Band Gap Hole Transporting Material for Efficient Perovskite Solar Cells", Nanoscale, 2016, 8, 6335-6340.

[174] Lim, Iseul; Kim, Eun-Kyung; Patil, Supriya A.; Ahn, Do Young; Lee, Wonjoo; Shrestha, Nabeen K.; Lee, Joong Kee; Seok, Won K.; Cho, Cheon-Gyu; Han, Sung-Hwan. "Indolocarbazole Based Small Molecules: an Efficient Hole Transporting Material for Perovskite Solar Cells", RSC Advances, 2015, 5, 55321-55327.

[175] Xu, Bo; Sheibani, Esmaeil; Liu, Peng; Zhang, Jinbao; Tian, Haining; Vlachopoulos, Nick; Boschloo, Gerrit; Kloo, Lars; Hagfeldt, Anders; Sun, Licheng. "Carbazole-Based Hole-Transport Materials for Efficient Solid-State Dye-Sensitized Solar Cells and Perovskite Solar Cells", Advanced Materials, 2014, 26, 6629-6634.

[176]Sung, Sang Do; Kang, Min Soo; Choi, In Taek; Kim, Hong Mo; Kim, Hyoungjin; Hong, MunPyo; Kim, Hwan Kyu; Lee, Wan In. "14.8% Perovskite Solar Cells Employing Carbazole Derivatives as Hole Transporting Materials", Chemical Communications, 2014, 50, 14161-14163.

[177]Kang, Min Soo; Sung, Sang Do; Choi, In Taek; Kim, Hyoungjin; Hong, MunPyo; Kim, Jeongho; Lee, Wan In; Kim, Hwan Kyu. "Novel Carbazole-Based Hole-Transporting Materials with Star-Shaped Chemical Structures for Perovskite-Sensitized Solar Cells", ACS Applied Materials & Interfaces, 2015, 7, 22213-22217.

[178] Wang, Junjie; Wang, Shirong; Li, Xianggao; Zhu, Lifeng; Meng, Qingbo; Xiao, Yin; Li, Dongmei. "Novel Hole Transporting Materials with a Linear π -Conjugated Structure for Highly Efficient Perovskite Solar Cells", Chemical Communications, 2014, 50, 5829-5832.

[179] Jeon, Nam Joong; Lee, Hag Geun; Kim, Young Chan; Seo, Jangwon; Noh, Jun Hong; Lee, Jaemin; Seok, Sang II. "o-Methoxy Substituents in Spiro-OMeTAD for Efficient Inorganic–Organic Hybrid Perovskite Solar Cells", Journal of the

American Chemical Society, 2014, 136, 7837-7840.

[180] Malinauskas, Tadas; Tomkute-Luksiene, Daiva; Sens, Rüdiger; Daskeviciene, Maryte; Send, Robert; Wonneberger, Henrike; Jankauskas, Vygintas; Bruder, Ingmar; Getautis, Vytautas. "Enhancing Thermal Stability and Lifetime of Solid-State Dye-Sensitized Solar Cells via Molecular Engineering of the Hole-Transporting Material Spiro-OMeTAD", ACS Applied Materials & Interfaces, 2015, 7, 11107-11116.

[181] Zheng, Lingling; Chung, Yao-Hsien; Ma, Yingzhuang; Zhang, Lipei; Xiao, Lixin; Chen, Zhijian; Wang, Shufeng; Qu, Bo; Gong, Qihuang. "A Hydrophobic Hole Transporting Oligothiophene for Planar Perovskite Solar Cells with Improved Stability", Chemical Communications, 2014, 50, 11196-11199.

[182] Lv, Songtao; Han, Liying; Xiao, Junyan; Zhu, Lifeng; Shi, Jiangjian; Wei, Huiyun; Xu, Yuzhuan; Dong, Juan; Xu, Xin; Li, Dongmei; Wang, Shirong; Luo, Yanhong; Meng, Qingbo; Li, Xianggao. "Mesoscopic $TiO_2/CH_3NH_3PbI_3$ Perovskite Solar Cells with New Hole-Transporting Materials Containing Butadiene Derivatives", Chemical Communications, 2014, 50, 6931-6934.

[183] Carli, Stefano; Baena, Juan Pablo Correa; Marianetti, Giulia; Marchetti, Nicola; Lessi, Marco; Abate, Antonio; Caramori, Stefano; Grätzel, Michael; Bellina, Fabio; Bignozzi, Carlo Alberto; Hagfeldt, Anders. "A New 1,3,4-Oxadiazole-Based Hole-Transport Material for Efficient $CH_3NH_3PbBr_3$ Perovskite Solar Cells", ChemSusChem, 2016, 9, 657-661.

[184] Zhang, Fei; Yi, Chenyi; Wei, Peng; Bi, Xiangdong; Luo, Jingshan; Jacopin, Gwénolé; Wang, Shirong; Li, Xianggao; Xiao, Yin; Zakeeruddin, Shaik Mohammed; Grätzel, Michael. "A Novel Dopant-Free Triphenylamine Based Molecular “Butterfly” Hole-Transport Material for Highly Efficient and Stable Perovskite Solar Cells", Advanced Energy Materials, 2016, 6, 1600401.

[185] Ma, Yingzhuang; Chung, Yao-Hsien; Zheng, Lingling; Zhang, Danfei; Yu, Xiao; Xiao, Lixin; Chen, Zhijian; Wang, Shufeng; Qu, Bo; Gong, Qihuang; Zou, Dechun. "Improved Hole-Transporting Property via HAT-CN for Perovskite Solar Cells without Lithium Salts", ACS Applied Materials & Interfaces, 2015,

7, 6406-6411.

[186] Steck, Christopher; Franckevicius, Marius; Zakeeruddin, Shaik Mohammed; Mishra, Amaresh; Bauerle, Peter; Gratzel, Michael. "A-D-A-Type S,N-Heteropentacene-Based Hole Transport Materials for Dopant-Free Perovskite Solar Cells", Journal of Materials Chemistry A, 2015, 3, 17738-17746.

[187] Gong, Gengfei; Zhao, Ning; Ni, DeBin; Chen, Jianyou; Shen, Yan; Wang, Mingkui; Tu, Guoli. "Dopant-Free 3,3'-Bithiophene Derivatives as Hole Transport Materials for Perovskite Solar Cells", Journal of Materials Chemistry A, 2016, 4, 3661-3666.

[188] Li, Hairong; Fu, Kunwu; Hagfeldt, Anders; Grätzel, Michael; Mhaisalkar, Subodh G.; Grimsdale, Andrew C. "A Simple 3,4-Ethylenedioxythiophene Based Hole-Transporting Material for Perovskite Solar Cells", Angewandte Chemie International Edition, 2014, 53, 4085-4088.

[189] Paek, S.; Zimmermann, I.; Gao, P.; Gratia, P.; Rakstys, K.; Grancini, G.; Nazeeruddin, Mohammad Khaja; Rub, Malik Abdul; Kosa, Samia A.; Alamry, Khalid A.; Asiri, Abdullah M. "Donor-π-Donor Type Hole Transporting Materials: Marked π-Bridge Effects on Optoelectronic Properties, Solid-State Structure, and Perovskite Solar Cell Efficiency", Chemical Science, 2016, 7, 6068-6075.

[190]Molina-Ontoria, Agustín; Zimmermann, Iwan; Garcia-Benito, Inés; Gratia, Paul; Roldán-Carmona, Cristina; Aghazada, Sadig; Graetzel, Michael; Nazeeruddin, Mohammad Khaja; Martín, Nazario. "Benzotrithiophene-Based Hole-Transporting Materials for 18.2 % Perovskite Solar Cells", Angewandte Chemie International Edition, 2016, 55, 6270-6274.

[191] Ganesan, Paramaguru; Fu, Kunwu; Gao, Peng; Raabe, Ines; Schenk, Kurt; Scopelliti, Rosario; Luo, Jingshan; Wong, Lydia H.; Gratzel, Michael; Nazeeruddin, Mohammad Khaja. "A Simple Spiro-Type Hole Transporting Material for Efficient Perovskite Solar Cells", Energy & Environmental Science, 2015, 8, 1986-1991.

[192] Abate, Antonio; Paek, Sanghyun; Giordano, Fabrizio; Correa-Baena, Juan-

Pablo; Saliba, Michael; Gao, Peng; Matsui, Taisuke; Ko, Jaejung; Zakeeruddin, Shaik M.; Dahmen, Klaus H.; Hagfeldt, Anders; Grätzel, Michael; Nazeeruddin, Mohammad Khaja. "Silolothiophene-Linked Triphenylamines as Stable Hole Transporting Materials for High Efficiency Perovskite Solar Cells", Energy & Environmental Science, 2015, 8, 2946-2953.

[193] Liu, Jian; Wu, Yongzhen; Qin, Chuanjiang; Yang, Xudong; Yasuda, Takeshi; Islam, Ashraful; Zhang, Kun; Peng, Wenqin; Chen, Wei; Han, Liyuan. "A Dopant-Free Hole-Transporting Material for Efficient and Stable Perovskite Solar Cells", Energy & Environmental Science, 2014, 7, 2963-2967.

[194] Krishna, Anurag; Sabba, Dharani; Yin, Jun; Bruno, Annalisa; Antila, Liisa J.; Soci, Cesare; Mhaisalkar, Subodh; Grimsdale, Andrew C. "Facile Synthesis of a Hole Transporting Material with a Silafluorene Core for Efficient Mesoscopic $CH_3NH_3PbI_3$ Perovskite Solar Cells", Journal of Materials Chemistry A, 2016, 4, 8750-8754.

[195] Vak, Doojin; Jo, Jang; Ghim, Jieun; Chun, Chaemin; Lim, Bogyu; Heeger, Alan J.; Kim, Dong-Yu. "Synthesis and Characterization of Spiro-Triphenylamine Configured Polyfluorene Derivatives with Improved Hole Injection", Macromolecules, 2006, 39, 6433-6439.

[196]McFarlane, Shaune L.; Coumont, Leah S.; Piercey, Davin G.; McDonald, Robert; Veinot, Jonathan G. C. "“One-Pot” Synthesis of a Thermally Stable Blue Emitter: Poly[spiro(fluorene-9,9′-(2′-phenoxy-xanthene)]", Macromolecules, 2008, 41, 7780-7782.

[197] Xu, Bo; Bi, Dongqin; Hua, Yong; Liu, Peng; Cheng, Ming; Gratzel, Michael; Kloo, Lars; Hagfeldt, Anders; Sun, Licheng. "A Low-cost Spiro[fluorene-9,9'-xanthene]-based Hole Transport Material for Efficient Solid-state Dye-sensitized Solar Cells and Perovskite Solar Cells", Energy & Environmental Science, 2016, 9, 873-877.

[198] Maciejczyk, Michal; Ivaturi, Aruna; Robertson, Neil. "SFX as a Low-Cost 'Spiro' Hole-Transport Material for Efficient Perovskite Solar Cells", Journal of Materials Chemistry A, 2016, 4, 4855-4863.

[199] Zhang, Yaohong; Wu, Guohua; Mora-Sero, Ivan; Ding, Chao; Liu, Feng; Huang, Qingxun; Ogomi, Yuhei; Hayase, Shuzi; Toyoda, Taro; Wang, Ruixiang; Otsuki, Joe; Shen, Qing. "Improvement of Photovoltaic Performance of Colloidal Quantum Dot Solar Cells Using Organic Small Molecule as Hole-Selective Layer", The Journal of Physical Chemistry Letters, 2017.

[200] Wu, Guohua; Kaneko, Ryuji; Sugawa, Kosuke; Islam, Ashraful; Bedja, Idriss; Gupta, Ravindra Kumar; Han, Liyuan; Otsuki, Joe. "Effect of Different Auxiliary Ligands and Anchoring Ligands on Neutral Thiocyanate-Free Ruthenium(II) Dyes Bearing Tetrazole Chromophores for Dye-Sensitized Solar Cells", Dyes Pigments, 2017, 140, 354-362.

[201] Shi, Yantao; Hou, Kaili; Wang, Yanxiang; Wang, Kai; Ren, HuiCai; Pang, MaoYin; Chen, Fan; Zhang, Sen. "Two Methoxyaniline-Substituted Dibenzofuran Derivatives as Hole-Transport Materials for Perovskite Solar Cells", Journal of Materials Chemistry A, 2016, 4, 5415-5422.

[202] Noh, Jun Hong; Im, Sang Hyuk; Heo, Jin Hyuck; Mandal, Tarak N.; Seok, Sang Il. "Chemical Management for Colorful, Efficient, and Stable Inorganic–Organic Hybrid Nanostructured Solar Cells", Nano letters, 2013, 13, 1764-1769.

[203] Kwon, Young Soo; Lim, Jongchul; Yun, Hui-Jun; Kim, Yun-Hi; Park, Taiho. "A Diketopyrrolopyrrole-Containing Hole Transporting Conjugated Polymer for Use in Efficient Stable Organic-Inorganic Hybrid Solar Cells Based on a Perovskite", Energy & Environmental Science, 2014, 7, 1454-1460.

[204] Nguyen, William H.; Bailie, Colin D.; Unger, Eva L.; McGehee, Michael D. "Enhancing the Hole-Conductivity of Spiro-OMeTAD without Oxygen or Lithium Salts by Using Spiro(TFSI)$_2$ in Perovskite and Dye-Sensitized Solar Cells", Journal of the American Society, 2014, 136, 10996-11001.

[205] Sanchez, Rafael S.; Gonzalez-Pedro, Victoria; Lee, Jin-Wook; Park, Nam-Gyu; Kang, Yong Soo; Mora-Sero, Ivan; Bisquert, Juan. "Slow Dynamic Processes in Lead Halide Perovskite Solar Cells. Characteristic Times and Hysteresis", The Journal of Physical Chemistry Letters, 2014, 5, 2357-2363.

[206] Dualeh, Amalie; Moehl, Thomas; Tétreault, Nicolas; Teuscher, Joël; Gao, Peng;

Nazeeruddin, Mohammad Khaja; Grätzel, Michael. "Impedance Spectroscopic Analysis of Lead Iodide Perovskite-Sensitized Solid-State Solar Cells", ACS Nano, 2014, 8, 362-373.

[207] Leijtens, Tomas; Giovenzana, Tommaso; Habisreutinger, Severin N.; Tinkham, Jonathan S.; Noel, Nakita K.; Kamino, Brett A.; Sadoughi, Golnaz; Sellinger, Alan; Snaith, Henry J. "Hydrophobic Organic Hole Transporters for Improved Moisture Resistance in Metal Halide Perovskite Solar Cells", ACS Applied Materials & Interfaces, 2016, 8, 5981-5989.

Acknowledgements

First and foremost, I am indebted to my advisor, Prof. Qing Shen, for her guidance throughout the course of my doctoral research. I am so very grateful that I learned many useful skills from her. She changed my mind and her support has helped me think and speak more like a professional researcher. I also thank her for helping my everyday life. To Prof. Toyoda, Prof. Abe, and Prof. Okuno, I thank them for all the support and advice. Their insights provided help in shaping the theories presented in this thesis. To Prof. Hayase and Dr. Ogomi, thank you so much for the PYS testing and analysis. To Mr. Kimura, thank you for teaching me to use TEM. To Prof. Otsuki, Dr. Wu, Prof. Mora-Sero, I am very pleasant cooperation with you, and thank you so much for your insights provided through discussions. I would like to especially thank Dr. Wu, who provided the hole transport materials for me.

In addition, I appreciate collaborations and suggestions from members of Shen Lab. I hope to collaborate with all of you in the future. And special thanks to Dr. Chang, Mr. Izuishi, Mr. Kuga, Mr. Ding, Mr. Kaji, Mr. Kobayasi, Mr. Nakazawa, Mr. Ozu, and Dr. Liu for your helping.

And finally, I would like to express my gratitude towards my beloved patents and wife for all of their loving support to make this thesis complete.

List of Publications

Papers

1. **Zhang Yaohong**[#], Wu Guohua[#], Mora-Sero Ivan, Ding Chao, Liu Feng, Huang Qingxun, Ogomi Yuhei, Hayase Shuzi, Toyoda Taro, Wang Ruixiang, Otsuki Joe, and Shen Qing. Improvement of photovoltaic performance of colloidal quantum dot solar cells using organic small molecule as hole-selective layer. *The Journal of Physical Chemistry Letter*, vol. 8, pp. 2163-2169, **2017**. ([#] these authors contributed equally to this work) (content of Chapter 4)

2. Wu Guohua[#], **Yaohong Zhang**[#], Ryuji Kaneko, Yoshiyuki Kojima, Qing Shen, Ashraful Islam, Kosuke Sugawa, Joe Otsuki. A 2,1,3-benzooxadiazole moiety in a D–A–D-type hole-transporting material for boosting the photovoltage in perovskite solar cells. *The Journal of Physical Chemistry C*, vol. 121, pp. 17617-17624, **2017**. ([#] these authors contributed equally to this work)

3. Guohua Wu, **Yaohong Zhang**, Ryuji Kaneko, Yoshiyuki Kojima, Kosuke Sugawa, Ashraful Islam, Towhid H. Chowdhury, Qing Shen, Md. Akhtaruzzaman, Takeshi Noda, Joe Otsuki. Hole-transport materials containing triphenylamine donors with a spiro[fluorene-9,9'-xanthene] core for efficient and stable large area perovskite solar cell. *Solar RRL,* DOI: 10.1002/solr.201700096, **2017**.

4. Chang Jin, Ogomi Yuhei, Ding Chao, **Zhang Yaohong**, Toyoda Taro, Hayase Shuzi, Katayama Kenji, and Shen Qing. Ligand-dependent exciton dynamics and photovoltaic properties of PbS quantum dot heterojunction solar cells. *Physical Chemistry Chemical Physics*, vol. 19, pp. 6358-6367, **2017**.

5. Kapil Gaurav, Ohta Takeshi, Koyanagi Tsuguo, **Zhang Yaohong**, Vigneshwaran Murugan, Ogomi Yuhei, Pandey Shyam S., Yoshino Kenji, Shen Qing, Toyoda Taro, Rahman Md. Mijanur, Minemoto Takashi, Murakami Takurou N., Segawa Hiroshi, and Hayase Shuzi. Investigation of Interfacial Charge transfer in Solution Processed Cs_2SnI_6Thin Films. *The Journal of Physical Chemistry C*, 121, pp. 13092-13100, **2017**.

6. **Zhang Yaohong**, Ding Chao, Wu Guohua, Nakazawa Naoki, Chang Jin, Ogomi

Yuhei, Toyoda Taro, Hayase Shuzi, Katayama Kenji, and Shen Qing. Air stable PbSe colloidal quantum dot heterojunction solar cells: ligand dependent exciton dissociation, recombination, photovoltaic property and stability. *The Journal of Physical Chemistry C*, vol. 120, pp. 28509-28518, **2016**. (content of Chapter 3)

7. **Zhang Yaohong**, Yi Zhiguo, Wu Guohua, and Shen Qing. Novel Y-doped $BiVO_4$ thin film electrodes for enhanced photoelectric and photocatalytic performance. *Journal of Photochemistry and Photobiology A: Chemistry*, vol. 327, pp. 25-32, **2016**.

8. Wu Guohua, Kaneko Ryuji, **Zhang Yaohong**, Shinozaki Yoshino, Sugawa Kosuke, Islam Ashraful, Han Liyuan, Bedja Idriss, Gupta Ravindra Kumar, Shen Qing, and Joe Otsuki. Neutral and anionic tetrazole-based ligands in designing novel ruthenium dyes for dye-sensitized solar cells. *Journal of Power Sources*, vol. 307, pp. 416-425, **2016**.

9. Wu Guohua, Kaneko Ryuji, Islam Ashraful, **Zhang Yaohong**, Sugawa Kosuke, Han Liyuan, Shen Qing, Bedja Idriss, Gupta Ravindra Kumar, Otsuki Joe. Thiocyanate-free asymmetric ruthenium(II) dye sensitizers containing azole chromophores with near-IR light-harvesting capacity. *Journal of Power Sources*, vol. 331, pp. 100-111, **2016**.

Conference Presentations

1. Oral：○**Zhang Yaohong**, Wu Guohua, Ding Chao, Zhang Yang, Liu Feng, Ogomi Yuhei, Toyoda Taro, Hayase Shuzi, Otsuki Joe, and Shen Qing. Suppression of recombination in PbS and PbSe based quantum dot solar cells by surface and interface engineering. *Asia-Pacific International Conference on Hybrid and Organic Photovoltaics (AP-HOPV17))*, Yokohama City, Japan, 02-04 February **2017**.

2. Oral：○**Zhang Yaohong**, Ding Chao, Chang Jin, Toyada Taro, Hayase Shuzi, and Shen Qing. Ligand-dependent performance of PbSe quantum dot planar heterojunction solar cell. *The 26th Annual Meeting of MRS-J*, Yokohama City, 19-22 December **2016**.

3. Poster: ○**Zhang Yaohong**, Ding Chao, Wu Guohua, Ogomi Yuhei, Toyoda Taro, Hayase Shuzi, and Qing Shen. Air-stable PbSe quantum dot solar cell: from device fabrication, storage to measurements. *The Irago Conference 2016*, Chofu, Japan, 01-02 November **2016**.

4. Oral：○**Zhang Yaohong**, Ding Chao, Chang Jin, Toyada Taro, Ogomi Yuhui, Hayase Shuzi, and Shen Qing. Air stable PbSe quantum dots heterojunction solar cells: ligand dependent exciton dissociation, recombination, photovoltaic property and stability. *The 77th JSAP Autumn Meeting*, Niigata City, 13-16 September **2016**.

5. Poster: ○**Zhang Yaohong**, Ding Chao, Chang Jin, Ogomi Yuhui, Hayase Shuzi, Toyada Taro, and Shen Qing. Performance of PbSe quantum dot based heterojunction solar cells: dependence on ligand type. *Annual Meeting on Photochemistry 2016*, Tokyo, 06-08 September **2016**.

6. Poster: ○**Zhang Yaohong**, Ding Chao, Chang Jin, Ogomi Yuhui, Hayase Shuzi, Toyada Taro, and Shen Qing. Performance of PbSe quantum dot based heterojunction solar cells: dependence on ligand type. *The 63rd JSAP Spring Meeting*, Tokyo, 19-22 March **2016**.

7. Poster: ○**Zhang Yaohong**, Yi Zhiguo, Wu Guohua, and Shen Qing. Novel Y-doped BiVO4 thin film electrodes for enhanced photoactivity of Rhodamine B degradation. *28th International Microprocesses and Nanotechnology Conference*, Toyama, Japan, 10-13 November **2015**.

8. Poster: ○**Zhang Yaohong**, Chang Jin, Izuishi Takuya, Ono Keita, Hayase Shuzi, Ogomi Yuhei, Katayama Kenji, Toyoda Taro, and Shen Qing. Photoexcited carrier dynamics and photovoltaic performance of PbSe/CdSe core/shell quantum dots. *The 76th JSAP Autumn Meeting*, Nagoya, 13-16 September **2015**.